SINGLE-NEUTRON EXCITATIONS OF THE $N = 51$ ISOTONES ^{83}Ge AND ^{85}Se

BY JEFFRY SINCLAIR THOMAS

A dissertation submitted to the

Graduate School—New Brunswick

Rutgers, The State University of New Jersey

in partial fulfillment of the requirements

for the degree of

Doctor of Philosophy

Graduate Program in Physics and Astronomy

Written under the direction of

Professor Jolie A. Cizewski

and approved by

New Brunswick, New Jersey

October, 2005

ABSTRACT OF THE DISSERTATION

Single-Neutron Excitations of the $N = 51$ Isotones ^{83}Ge and ^{85}Se

by Jeffry Sinclair Thomas

Dissertation Director: Professor Jolie A. Cizewski

The properties of low-lying states in nuclei near the closed shells are key benchmarks in the description of nuclear structure, and influence how heavier nuclei are produced in the astrophysical rapid neutron capture (r-) process. With the advent of radioactive ion beams, the low-lying single-particle states in neutron-rich nuclei near the closed shells can be studied. An experimental program to measure (d,p) neutron transfer reactions on neutron-rich nuclei, probing the single-neutron states near the $N = 50$ closed shell, has been established at the Holifield Radioactive Ion Beam Facility (HRIBF) at Oak Ridge National Laboratory (ORNL). In the first two measurements of the program, the states of the $N = 51$ nuclei ^{83}Ge and ^{85}Se were populated in inverse kinematics reactions: isobaric $A = 82$ and $A = 84$ radioactive ion beams

bombarded thin deuterated polyethylene $(CD_2)_n$ targets. Protons detected from the transfer reaction were used to determine the excitation energies, spins, parities, and single-particle strengths of the low-lying states of the $N = 51$ nuclei. These are the first measurements of (d,p) transfer on neutron-rich r-process nuclei.

The Q-value of the ^{2}H(^{82}Ge,p)^{83}Ge reaction was determined ($Q = 1.47 \pm 0.07$ MeV), yielding the mass of ^{83}Ge [$\Delta(^{83}\text{Ge}) = -61.25 \pm 0.26$ MeV]. The excitation energy of the first-excited state was determined to be $E_x = 280 \pm 70$ keV. Higher excited states were found to be above ~ 1 MeV in excitation. The measured proton differential cross sections with respect to angle were used to assign spins and parities to the ground ($J^\pi = 5/2^+$) and first-excited ($J^\pi = 1/2^+$) states. The normalizations of the differential cross sections, when compared to distorted waves calculations, gave spectroscopic factors of $S_{\ell j} = 0.48 \pm 0.12$ and $S_{\ell j} = 0.50 \pm 0.13$ for the ground and first-excited states, respectively.

A number of states were populated in the ^{2}H(^{84}Se,p)^{85}Se reaction measurement. Proton differential cross section measurements yielded level assignments and spectroscopic factors of $J^\pi = 5/2^+$ and $S_{\ell j} = 0.33 \pm 0.08$ for the ground state and $J^\pi = 1/2^+$ and $S_{\ell j} = 0.30 \pm 0.08$ for the first-excited state. The state at $E_x = 1.114$ MeV and a doublet of states with $E_x = 1.438$ MeV and $E_x = 1.444$ MeV were populated, but definitive spin-parity assignments could not be made.

Acknowledgements

Five years is a significant chunk of time from which to recount and thank all of the influences that have shaped the development of a budding physicist. But, here goes.

I would like to thank my advisor, Jolie Cizewski, for encouraging me to try a nuclear physics project during the summer that I was considering leaving physics altogether. Four years, two experiments, countless conferences, and one dissertation later, I am grateful that she can be very persuasive.

I'd also like to thank the research scientists of the nuclear astrophysics group at Oak Ridge National Laboratory for teaching me how to be an experimentalist: Dan Bardayan for taking me from the "how-to" of the oscilloscope to the *right* way of finding the noisy channel in SIDAR; Jeff Blackmon for throwing me into the fire early and often, even if that meant scan files that couldn't possibly have any mistakes, and for pulling me out of said fire when trying to decide what to be when I grow up; and Michael Smith for showing me the nuances of a productive night shift (soldering switches for beam-line valves currently in use, making live-time vs. time plots, discussions of the intricacies of the data acquisition), and what it means to be professional. A special thanks goes to all three for reading and commenting on this dissertation, and to Dan for agreeing to be a thesis committee member.

Thanks go to Ray Kozub for discussions on inverse kinematics and the finer points

of DWUCK5, a wonderful program. I am grateful that Kate Jones took the time to make sure that I stayed on track with analysis and publications (despite the language barrier), and that my vast knowledge of Welsh singers turned out to be useful after all. Thanks must also go to Micah Johnson for reminding me why I like South Jersey, and Dale Visser for reminding me why I "like" Java, even if both are a little too comfortable with the Dark Side. Steve Pain is always right, period.

A number of fellow/former students stationed in Oak Ridge deserve thanks for making the stay enjoyable. To my graduate brother-in-arms, Ryan Fitzgerald ("Why, that Ryan, if I were *half* the student..."), we will change the world, but we'll need to burn something. Jake Livesay and Andy Chae are always good for cultural exchanges (*JSA*, Vietnamese food in Oak Ridge), philosophical musings ("that's sostupid"), and generally relaxed conversations about life and nature (mwokay?). Because they are great motivators and I should return the favor, Carlo Domizioli and Brian Moazen are now on the clock ("when are you going to write your thesis?").

The experiments of this dissertation would not have been possible without the additional help of Carl Gross, Uwe Greife, Felix Liang, Zhanwen Ma, and Dan Shapira. For some reason it wasn't possible for one person to take all the shifts during the experiments, or debug all of the initial problems with the detectors. These fine people gladly stepped in to help.

Finally, I want to thank my family for allowing me to run up my phone bill with one-sided conversations about what it is I do. If it's possible, I swear I could *hear* their eyes glazing over. Thank you for your support.

Table of Contents

Abstract ii

Acknowledgements iv

List of Tables ix

List of Figures xi

1. Introduction 1

1.1. Background 2

1.1.1. Single-particle structure 2

1.1.2. The r-process 6

1.2. Direct neutron capture 11

1.3. Experimental aims 12

1.4. Structure of the dissertation 14

2. Direct Reaction Theory 15

2.1. Overview of distorted-wave direct reaction theory 15

2.1.1. Preliminaries 15

2.1.2. Introduction of distorted waves 19

2.2. Connections with experiment 22

2.3. Optical model and DW computer codes 25

2.4. Asymptotic normalization coefficients 28

2.5. Direct radiative capture theory 31

3. Facility and Equipment 34

3.1. Beam production and delivery 34

3.2. Detectors 36

3.2.1. Ionization chamber 37

3.2.2. Silicon strip detectors 43

3.3. Targets 48

4. The Experiments and Data 50

4.1. ^{2}H(^{82}Ge,p)^{83}Ge 50

4.2. ^{2}H(^{84}Se,p)^{85}Se 61

4.3. Proton angular distribution data 66

4.3.1. ^{2}H(^{82}Ge,p)^{83}Ge angular distributions 69

4.3.2. ^{2}H(^{84}Se,p)^{85}Se angular distributions 74

5. Interpretation 80

5.1. Energy level systematics 80

5.2. Masses far from stability 88

6. Summary and Conclusion 94

6.1. Outlook 96

6.1.1. Prospects for further $N = 51$ studies 96

6.1.2. Prospects for further (d,p) studies at HRIBF 99

References 104

Vita 110

List of Tables

3.1. Geometric and operating parameters for the MSL-type YY1 wedge silicon detector [Mic05, Dav00]. 47

4.1. Comparison of published spectroscopic factors, $S_{\ell j}$, and those derived from the present optical model analysis using global parameters. Published data are from: ^{90}Zr(d,p)^{91}Zr [Rat73]; ^{88}Sr(d,p)^{89}Sr [Cle78]; ^{86}Kr(d,p)^{87}Kr [Har70]; ^{82}Se(d,p)^{83}Se [Mon78]. 68

4.2. Optical model potential parameters for the ^{2}H(^{82}Ge,p)^{83}Ge reaction. For the defintion of the parameters see Sect. 2.3. The value at * is adjusted to reproduce the binding energy of the neutron in ^{83}Ge. . . . 71

4.3. Optical model potential parameters for the ^{2}H(^{84}Se,p)^{85}Se reaction. For the defintion of the parameters see Sect. 2.3. The value at * is adjusted to reproduce the binding energy of the neutron in ^{85}Se. . . . 75

4.4. Summary of spectroscopic quantities determined from the measurements of the ^{82}Ge,^{84}Se(d,p) reactions in the present work. The ℓ are the transferred orbital angular momenta, J^{π} are the assigned (tentative) spins and parities, $S_{\ell j}$ are the extracted spectroscopic factors, C^2 are the squared ANCs, and $\Delta(^{A}X)$ is the mass excess of nucleus ^{A}X. Spectroscopic factors and ANCs for both ℓ-transfers are given for the 1.114 MeV excitation in ^{85}Se. The excitation energies of the states of ^{85}Se are taken from [Omt91]. 79

5.1. Comparison of the experimental and calculated [Bro03] properties of the first two states of ^{83}Ge. 86

List of Figures

1.1. Single-particle levels for various potentials. From left to right: (a) Diffuse surface for neutron-rich nuclei, similar to harmonic oscillator with spin-orbit potential; (b) $N_{osc} = 4$ and 5 harmonic oscillator shells; (c) Woods-Saxon potential; (d) Woods-Saxon potential with strong spin-orbit potential. Figure adapted from [Dob96]. 4

1.2. Chart of the nuclides showing some available radioactive ion beams at the HRIBF (Sect. 3.1) and a possible r-process path. 8

1.3. Observed solar r-process abundances (points), and calculations using a standard mass model (dashed line) and one with the shell structure "quenched" (solid line). See text. Figure taken from [Fre99]. 9

1.4. Known properties of the ground and first-excited states of even $Z \leq 40$, $N = 51$ isotones [Bha05, Omt91]. Dashed lines to the states of ^{85}Se indicate the uncertainty in level assignments. 13

2.1. Sample DW-calculated angular distributions for the ^{82}Ge(d,p)^{83}Ge reaction at $E_{beam} = 4$ MeV/nucleon, using the code TWOFNR [Iga]. . . 28

3.1. Beam production and delivery at the HRIBF. Figure taken from [HRI05]. 35

3.2. Diagram of the ionization chamber. The carbon-foil micro-channel plate detector and associated electronics were not used in this dissertation. Isobutane as a fill gas was replaced with tetrafluoromethane (see text). Figure taken from [Bar00]. 39

3.3. Electron drift velocities as functions of density-reduced electric field strength using CF_4 (circles and solid lines [Hun88, Chr79]) and i-C_4H_{10} (triangles and dashed lines [Chr66, Pal75, Bia99]) fill gases. Solid symbols are data points, open symbols are calculations. 42

3.4. Single SIDAR strip calibration spectrum showing the two α lines at 5.805 MeV and 5.763 MeV with a peak fit for each. 45

3.5. MSL-type YY1 wedge. Figure from Micron Semiconductor, Ltd. [Mic05]. 46

4.1. Energy loss ΔE vs. total energy E spectrum from the ionization chamber for the $A = 82$ beam. 52

4.2. TAC spectrum for the ^{2}H(^{82}Ge,p)^{83}Ge reaction generated by a start signal from the silicon detectors and a stop signal from the ionization chamber. The silicon detectors were required to be above a low-energy noise threshold. 54

4.3. SIDAR strip number vs. proton energy in coincidence with (a) Se and (b) Ge from the $A = 82$ beam in the ionization chamber. 55

4.4. ^{2}H(^{82}Se,p)^{83}Se reaction Q-value spectrum summed over all angles. The solid line is the fit of the doublet of states at $E_x = 540$ keV and $E_x = 582$ keV. The ground-state Q-value of the reaction is $Q = 3.593$ MeV [Mon78]. 56

4.5. ^{82}Se(d,p)^{83}Se reaction Q-value spectrum as measured in normal kinematics at one angle. Figure taken from [Mon78]. Peaks labeled 3,4,7,12,and 22 correspond to states observed in the present measurement. The ^{12}C reaction contaminant would not be seen in the present measurement. 57

4.6. ^{2}H(^{82}Ge,p)^{83}Ge reaction Q-value spectrum summed over all angles. The dashed line is the two-peak fit of the ground and first-excited states (see text). 58

4.7. MSL Design S1 annular detector. Figure from Micron Semiconductor, Ltd. [Mic05]. 62

4.8. Energy loss ΔE vs. total energy E spectrum from the ionization chamber for the $A = 84$ beam. 62

4.9. Detector strip number vs. proton energy in coincidence with Se from the $A = 84$ beam in the ionization chamber for the (a) SIDAR and (b) CD silicon detectors. 63

4.10. Strip angles for one wedge of SIDAR as calculated by a computer program (open circles) and determined from a few counts in a strip (filled triangles). The error bars give the calculated angular ranges for a strip. 64

4.11. ^{2}H(^{84}Se,p)^{85}Se reaction Q-value spectrum summed over all angles. The ground-state Q-value of the reaction is $Q = 2.323$ MeV [Aud03]. . . . 65

4.12. Proton angular distributions fit with global optical model parameters [Loh74] and [Var91]. Filled symbols (solid lines) are for $\ell = 2$ transfer to $5/2^+$ states; open symbols (dashed lines) are for $\ell = 0$ transfer to $1/2^+$ states. Data are for (a) ^{90}Zr(d,p)^{91}Zr [Rat73], (b) ^{88}Sr(d,p)^{89}Sr [Cle78], (c) ^{86}Kr(d,p)^{87}Kr [Har70], (d) ^{82}Se(d,p)^{83}Se [Mon78]. 67

4.13. Proton angular distributions as functions of c.m. angle for ^{83}Ge. (a) Ground-state data are fit by an $\ell = 2$ DW calculation; (b) $E_x = 280$ keV data are fit by an $\ell = 0$ DW calculation. 70

4.14. DW-calculated angular distributions with varying radial cutoffs in the overlap functions for ^{83}Ge. (a) Ground-state; (b) $E_x = 280$ keV state. 72

4.15. Dependencies of the extracted spectroscopic factors, S, and asymptotic normalization coefficients, C^2, on the single-particle ANCs, b, for ^{83}Ge. The single-particle ANCs are themselves functions of the bound-state potential geometry. (a) Ground-state; (b) $E_x = 280$ keV state. 73

4.16. Proton angular distributions as functions of c.m. angle for ^{85}Se. (a) Ground-state data are fit by an $\ell = 2$ DW calculation; (b) $E_x = 462$ keV data are fit by an $\ell = 0$ DW calculation. 74

4.17. DW-calculated angular distributions with varying radial cutoffs in the overlap functions for ^{85}Se. (a) Ground-state; (b) $E_x = 462$ keV state. 76

4.18. Dependencies of the extracted spectroscopic factors, S, and asymptotic normalization coefficients, C^2, on the single-particle ANCs, b, for ^{85}Se. The single-particle ANCs are themselves functions of the bound-state potential geometry. (a) Ground-state; (b) $E_x = 462$ keV state. 77

4.19. Proton angular distributions as functions of c.m. angle for ^{85}Se higher-lying excitations. (a) $E_x = 1.115$ MeV data are fit with $\ell = 2$ and $\ell = 4$ DW calculations; (b) doublet of $E_x = 1.438 + 1.444$ MeV data with $\ell = 2$ DW calculations as guides (see text). 78

5.1. Spectroscopic properties of the first two states of the even $Z \leq 40$, $N = 51$ isotones. The lengths of the thick lines represent measured spectroscopic factors. Data for ^{83}Ge and ^{85}Se are from the present work. Data for the other $N = 51$ isotones: ^{91}Zr [Rat73], ^{89}Sr [Cle78], ^{87}Kr [Har70]. 81

5.2. Relative energies of the first $5/2^+$ and $7/2^+$ states of odd-A Sb ($Z = 51$) isotopes, assumed to be the $\pi d_{5/2}$ and $\pi g_{7/2}$ single-particle states, respectively. Data taken from [Bha05]. 83

5.3. Neutron single-particle energies above the Fermi level in ^{78}Ni calculated from the Skyrme parameterization [Bro03]. 85

5.4. Excitation energies of the first 2^+ states in the even $Z \leq 40$, $N = 50$ isotones. Data taken from [Bha05, Pad05]. 87

5.5. The mass excess, Δ, of ^{83}Ge as measured (horizontal line with dashed-line error bars), and predicted from the Atomic Mass Evaluation (AME) 2003 [Aud03], the Finite Range Droplet Model (FRDM) [Möl95], the Hartree-Fock-Bogoliubov-8 (HFB-8) model [Sam04], and the Duflo-Zuker model [Duf95]. 89

5.6. Differences between experimentally measured masses [Aud03] and predictions from the Duflo-Zuker mass model [Duf95, AMD05], offset by Z MeV, for isotopic chains with $Z = 28 - 40$. The circled point is the value for ^{83}Ge. 92

5.7. Differences between experimentally measured masses [Aud03] and predictions from the Duflo-Zuker mass model [Duf95, AMD05], offset by Z MeV, for isotopic chains of $Z = 48 - 64$. 93

6.1. Calculated dependency of the ratio $\sigma^{DW} / \left(b^B_{A\ell j}\right)^2$ as a function of the single-particle ANC, $b^B_{A\ell j}$ (points). (a) peripheral reaction; horizontal line is a "measured" ratio $(d\sigma/d\Omega)/(C^B_{A\ell j})^2$. (b) non-peripheral reaction; the measured ratio (horizontal lines) constrains the single-particle ANC (vertical lines) leading to a more accurate spectroscopic factor. . 98

6.2. Calculated angular distributions for the ^{132}Sn(d,p)^{133}Sn reaction with $\ell = 3$ transfer at $E_{beam} = 4$ MeV/nucleon, referred to c.m. (dashed) and laboratory (solid) coordinates. 100

6.3. The Oak Ridge Rutgers University Barrel Array showing the two rings of charged-particle telescopes. The gap between rings allows for a target to be mounted. 101

Chapter 1

Introduction

Nuclear structure physics is concerned with the shapes, sizes, internal states of motion, the transitions between those states, and the decays of atomic nuclei. It is the study of the not-so-familiar strong force that binds nuclei, and the phenomenology associated with that force. The properties of the large number of stable nuclei that exist in nature are the foundation for the nuclear models that describe that phenomenology. However, there exist many more nuclei away from stability, and it is not certain that the models developed for stable nuclei are still applicable in those cases.

An era of investigation is emerging now where the models of nuclear structure—as applied to nuclei close to stability—are being tested with, revised because of, and expanded to include the physics of more exotic nuclei. These investigations are possible because of advances in producing these very rare isotopes in sufficient numbers to allow for their study. The availability of radioactive ion beams has allowed physicists to probe nuclei ever closer to the extremes of nuclear existence. But to use these new beams effectively, novel approaches for measurement have to be introduced, and old techniques developed for light-mass beams on heavy targets adapted to accomodate the unique challenges of measuring with heavy radioactive beams on light-mass targets.

Studies of the structure of nuclei far from stability are also important for understanding the observed abundances of elements in the cosmos. For example, the nuclei studied in this dissertation have bearing on the astrophysical process of rapid neutron capture (the r-process), responsible for the origin of about half of the elements heavier than iron. The work presented here is part of the present effort that emphasizes the overlap of nuclear structure and nuclear astrophysics, and the nuclear reactions that enable these studies.

1.1 Background

1.1.1 Single-particle structure

The binding energies of the last nucleons of the stable isotopes and the natural abundances of the elements indicate a certain stability for particular "magic" numbers—2, 8, 20, 28, 50, 82, 126—of protons and neutrons (e.g. [May48, Bar39]). The observed ground-state spins, magnetic moments, and quadrupole moments also show regularites around the same magic numbers [Fee49]. These experimental facts suggest that the structure of atomic nuclei can be described by a shell model, analogous to the case of atomic electrons.

With the atomic shell model, the central Coulomb potential of the positively charged nucleus binds the electrons in orbits characterized by their angular momentum, which are constants of motion. The mutual interactions between electrons are treated as perturbations on the dominant Coulomb attraction. It is unintuitive to imagine how a very strong nuclear force between nucleons can be responsible for a

similar central potential in which protons and neutrons move nearly independently of each other. However, the uncertainty and Pauli principles, together, cause the "saturation" of the nuclear forces and the large mean free paths of nucleons in a nucleus [Rin80, Pre75]. The total binding energy between two interacting nucleons is an interplay between the strong nuclear attraction (with a repulsive "hard core" at very short distances) and the relative kinetic energy of the pair. By the uncertainty principle, the kinetic energy has to increase with ever smaller internucleon distances:

$$E_{kin} \approx \frac{(\Delta p)^2}{2(M/2)} \geq \frac{\hbar^2}{M\,(\Delta x)^2}, \tag{1.1}$$

where $M/2$ is the reduced mass of the system. The combination of the potential and kinetic energies leads to a total binding energy that is positive for very short distances with a shallow minimum at ≈ 2.4 fm, and quickly disappears because of the short range of the nuclear potential [Rin80]. As a result, only a few nucleons can be within the interaction range of a single nucleon [Rin80]. Because of the Pauli principle, if two nucleons are to collide (interact) with each other, the collision must trasnfer enough energy to move the nucleons to available quantum states that are not blocked because of their occupation by other nucleons, that is, to states above the Fermi energy [Kra87]. As this generally involves a large energy transfer, the collisions rarely happen, and the nucleons behave as if they were non-interacting. It is in this sense that the nuclear shell model can describe the nucleus as a collection of nucleons moving nearly independently of each other in an average central potential established by the very motion of those nucleons.

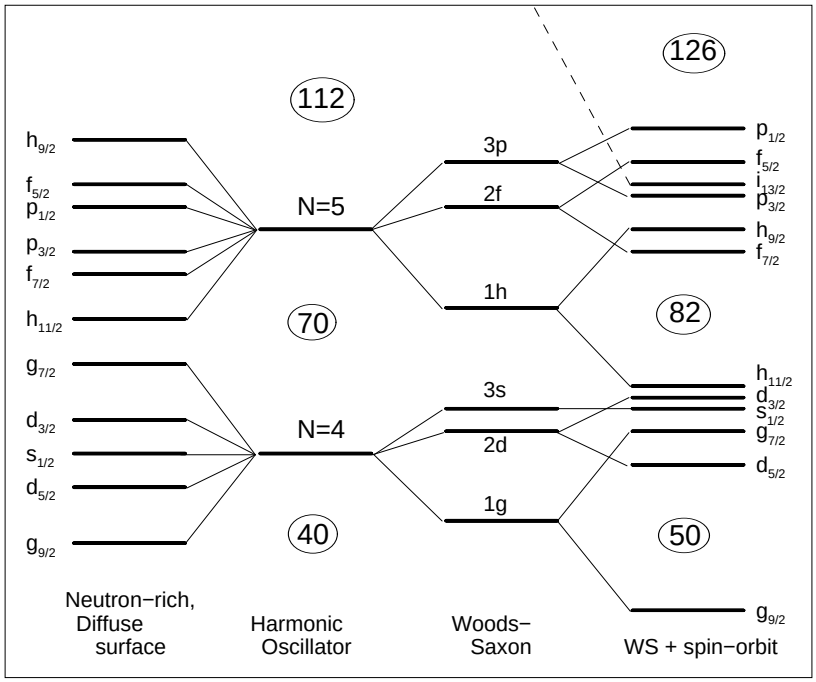

Figure 1.1: Single-particle levels for various potentials. From left to right: (a) Diffuse surface for neutron-rich nuclei, similar to harmonic oscillator with spin-orbit potential; (b) $N_{osc} = 4$ and 5 harmonic oscillator shells; (c) Woods-Saxon potential; (d) Woods-Saxon potential with strong spin-orbit potential. Figure adapted from [Dob96].

As a first approximation, the average potential is treated as a harmonic oscillator potential. The degenerate shell levels for nucleon numbers between $Z, N = 40 - 112$ in this scheme are shown in Fig. 1.1(b). An improvement to the model is made by using a more realistic average potential, such as a Woods-Saxon shape which is similar to the observed shape of mass density distributions in nuclei. Figure 1.1(c) displays how this potential splits some of the degeneracy, but is unable to reproduce the observed magic numbers. It was the insight of Mayer [May49] and Haxel, Jensen, and Suess [Hax49] to include a strong spin-orbit interaction that favors the higher-spin partner ($j = \ell + 1/2$) that led to the theoretical reproduction of all of the observed magic numbers in the stable isotopes (Fig. 1.1(d)).

A key concept of a shell model is the definite spatial orbital, characterized by its

angular momentum properties, that a single particle occupies [Kra87]. In the nuclear shell model, some of the properties of a nucleus on the whole can be determined by a relative few of these single-particle orbitals. Just as with the description of electrons in atoms, closed shells can be considered, for the most part, as inert cores. The valence nucleons determine the spins and parities of the low-lying states in nuclei. For example, the ground-state spin and parity of the $N = 51$ isotones is expected to be $J^\pi = 5/2^+$; the even number of valence protons pairing off to form $J^\pi = 0^+$, the underlying core of closed shells of protons and neutrons also with $J^\pi = 0^+$, and a single neutron occupying a $d_{5/2}$ orbital outside the $N = 50$ closed shell.

The nuclear shell model was designed for, and explains very well, the experimental observations of nuclei near the valley of stability. However, the available data are limited mostly to those nuclei, and there is little or no experimental data for the thousands of nuclei away from stability, particularly those that are very neutron rich. It is not clear that the descriptions of nuclear structure, such as the shell model, can adequately describe the physics of these exotic nuclei. As discussed in Sect. 5.1, a particular part of the proton-neutron interaction has been shown to cause the migration of single-particle orbitals, with the possibility of creating new shell closures in exotic nuclei. Also, Hartree-Fock-Bogoliubov mean-field calculations for weakly-bound, neutron-rich nuclei with diffuse surfaces show that these systems should exhibit more uniformly spaced single-particle spectra similar to that from a harmonic oscillator potential with a spin-orbit interaction [Dob96]. This is illustrated in Fig. 1.1(a).

The single-particle states of exotic nuclei, particularly near traditional closed

shells, serve as benchmarks for nuclear structure studies. The investigations of the low-lying states of the $N = 51$ isotones ^{83}Ge and ^{85}Se—both studied in this dissertation—are first steps in determining if or what types of changes nuclear structure might undergo in exotic nuclei far from stability.

1.1.2 The *r*-process

The r-process is believed to be the origin of half of the elements heavier than iron in the universe. In some astrophysical sites, such as postulated in the remnants of core-collapse supernovae, the neutron density ($\approx 10^{23}$ cm^{-3}) and the temperature ($\approx 10^9$ K) are both high [Cla83]. With the presence of seed nuclei, an equilibrium between neutron captures and photodisintegrations is quickly established in an isotopic chain. Both the neutron capture and photodisintegration rates are much faster than the β decay rates, allowing for an equilibrated build up of abundances governed by the detailed balance between the (n,γ) and (γ,n) reaction rates [Qia03]. Abundance ratios for neighboring isotopes can be calculated based on the conditions for statistical equilibrium and a nuclear Saha-type equation for the photodisintegration rate [Cla83, Qia03]:

$$\begin{aligned}\frac{Y(Z,A+1)}{Y(Z,A)} &= \frac{n_n\langle v\sigma_{n,\gamma}(Z,A)\rangle}{\lambda_{\gamma,n}(Z,A+1)} \\ &= n_n\left(\frac{2\pi\hbar^2}{m_u kT}\right)^{3/2}\left(\frac{A+1}{A}\right)^{3/2}\frac{G(Z,A+1)}{2G(Z,A)}\exp\left[\frac{S_n(Z,A+1)}{kT}\right].\end{aligned} \tag{1.2}$$

In this equation, $Y(Z,A)$ is the abundance of the isotope with atomic number Z and mass number A; $n_n\langle v\sigma_{n,\gamma}(Z,A)\rangle$ is the thermally-averaged neutron capture rate;

$\lambda_{\gamma,n}(Z, A+1)$ is the photodisintegration rate; $S_n(Z, A)$ is the neutron separation energy; $G(Z, A)$ is the nuclear partition function; n_n is the neutron concentration; m_u is the nucleon mass; T is the temperature; and k is Boltzmann's constant.

The abundances build up in typically one or two isotopes in a chain, and r-process nucleosynthesis must wait for these isotopes to β decay to proceed to the next isotopic chain. For this reason, the most abundant isotopes in a chain are usually called "waiting points" of the r-process. After moving up to the next chain, statistical equilibrium is quickly established again, producing the next waiting point nuclei that β decay to the next chain, and so on [Cla83]. The r-process path is identified by tracing out the most abundant elements. The most abundant isotope, (Z, A), in an isotopic chain can be crudely estimated by setting $Y(Z, A+1) \lesssim Y(Z, A)$ and neglecting the small differences in atomic mass numbers and nuclear partition functions, leading to [Qia03]:

$$S_n(Z, A+1) \lesssim kT \ln \left[\frac{2}{n_n} \left(\frac{m_u kT}{2\pi\hbar^2} \right)^{3/2} \right]. \tag{1.3}$$

The condition for the isotopic ratio of Eq. 1.2 to be $\lesssim 1$ amounts to identifying the turning point where, for a given temperature and neutron concentration, the pre-factors to the exponential and the exponential itself just balance. The overall trend of neutron separation energies, even with the odd-even staggering due to the pairing effect, is to decrease with increasing neutron number. Therefore, after the turning point, the exponential is no longer large enough to counteract the smallness of the pre-factors, and the abundance ratio of succeeding isotopes drops below 1. Typically,

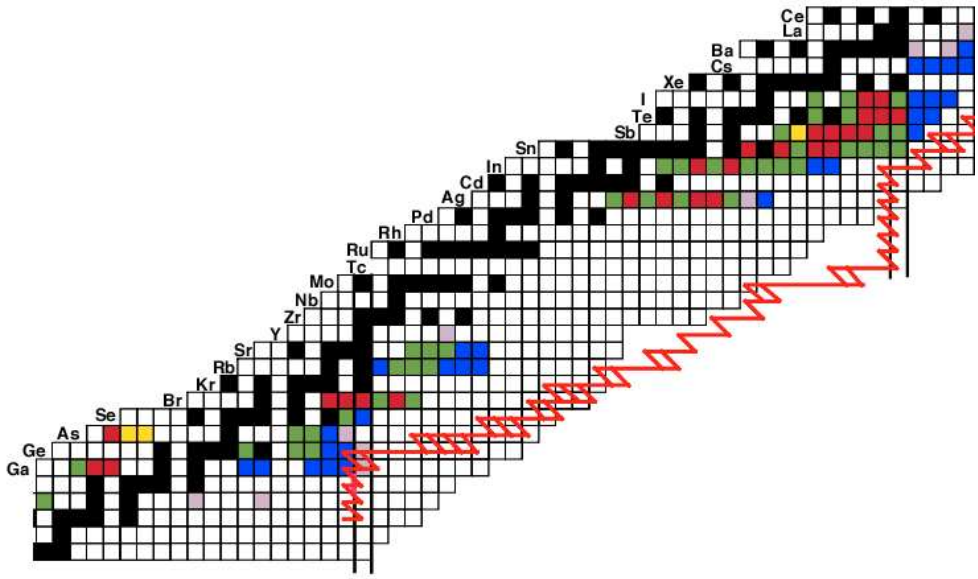

Figure 1.2: Chart of the nuclides showing some available radioactive ion beams at the HRIBF (Sect. 3.1) and a possible r-process path.

neutron separation energies fall off rapidly just after a closed neutron shell, and lifetimes against β decay for closed shell nuclei are longer, leading to the tendency of waiting point nuclei to have magic numbers of neutrons. The r-process path, therefore, traces the different elements that have the same number of neutrons until there is a point where the neutron separation energies are such that the path "breaks through" to the next string of waiting point nuclei (see Fig. 1.2).

The whole r-process takes on the order of a few seconds to progress from the lighter nuclei to the heavier nuclei that decay mainly by fissioning [Qia03]. Nuclei with very large neutron excesses can be generated in this way. As the material cools, or the process runs out of neutrons to feed the captures, the statistical equilibrium faces a "freeze out". All of the unstable, built-up isotopes decay back to stability generating concentrations in stable isotopes that reflect the conditions at the freeze out [Cla83].

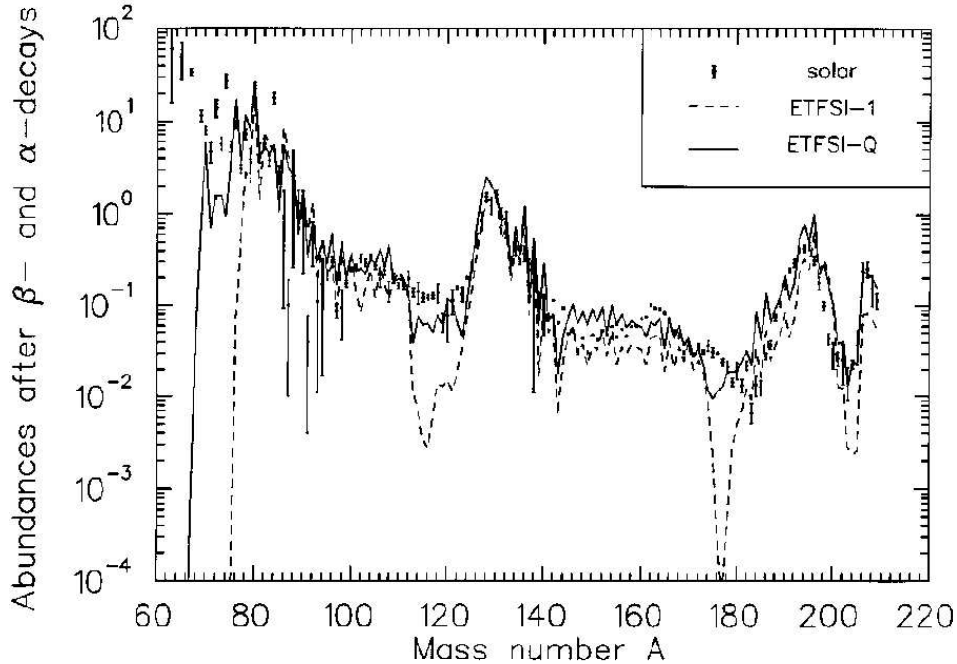

Figure 1.3: Observed solar r-process abundances (points), and calculations using a standard mass model (dashed line) and one with the shell structure "quenched" (solid line). See text. Figure taken from [Fre99].

The solar abundances of the elements have been measured, and after subtracting out the contributions from other nucleosynthesis processes (e.g. the slow neutron capture process), the solar r-process abundances can be extracted (see Fig. 1.3). The large peaks at $A \sim 80$, $A \sim 130$, and $A \sim 195$ correspond to the decay of the neutron-rich waiting point nuclei at $N = 50$, $N = 82$, and $N = 126$, respectively.

Astrophysicists try to reproduce plots such as Fig. 1.3 with full network calculations that incorporate the predicted properties of the large number of unstable nuclei that are expected to exist out to the neutron drip line, the limit where nuclei become particle-unbound to neutrons. The vast majority of these nuclei have never been observed, however. The measurement of at least a few key nuclei could greatly impact

the calculations. For example, it was shown that neutron capture rates on particular exotic nuclei near the closed shells, while not necessarily important during the processing phase, determine the extent of modifications to the calculated r-process abundances during the freeze-out phase [Sur01]. These modifications alter the solar abundances that are observed in noticeable ways [Sur01]. Any measurements that provide at least indirect information to the neutron capture rates (e.g. excitation energies of states, level assignments, spectroscopic factors; see Sect. 1.2) are useful.

The calculations of r-process abundances have also led to suggestions of new physics that might be observed when the most exotic nuclei are finally measured. The network calculations rely on models to predict the masses of the unmeasured nuclei. Traditionally, these models have been based on measured properties of stable nuclei (see Sect. 5.2). An abundance calculation, using a standard nuclear structure model (such as displayed in Fig. 1.1(d)) as input for the predicted masses, is shown in Fig. 1.3 and displays a large deficiency in the abundance predictions just below the $A \sim 130$ and $A \sim 195$ peaks. It was found that by changing the mass model to include a "quenching" of the shell structure, the calculations are better able to reproduce the solar abundances [Che95,Fre99]. The nuclear structure assumptions in these quenched calculations include a more uniform spacing of the single-particle levels that eliminates the large shell gaps observed in nuclei close to stability [Che95]. Measurements of the single-particle structure of exotic nuclei are, therefore, important to determine if the shell structure that has been successful for over 50 years in characterizing nuclei near stability is changed in neutron-rich systems.

1.2 Direct neutron capture

The synthesis of elements in the r-process may be modified by neutron capture reactions following the fall out from the (n,γ)-(γ,n) nuclear statistical equilibrium [Sur01]. During the equilibrium phase of the process, the distribution of nuclei is typically concentrated in the isotopes near the closed shells as a result of the sharp drop-offs in neutron binding energies just past the closed shell (see Sect. 1.1.2). As the material cools, neutron captures and β decays of these near-closed-shell nuclei alter the abundance pattern [Sur01].

In most nuclei near stability, neutron capture proceeds through a number of closely spaced states just above the neutron threshold energy of the compound nucleus. Such a process is described reasonably well by statistical modeling incorporating the high density of states available for capture, and the subsequent decay of the compound nucleus [Hau52, Rau97]. The capture can also take place in a direct process to a discrete bound state accompanied by the simultaneous emission of a gamma ray. The direct component of neutron capture is usually a small contribution compared to resonant capture. However, neutron capture reactions on many neutron-rich, closed-shell nuclei are expected to be dominated by the direct process because the small Q-values for neutron capture mean the level densities near the neutron threshold energy are low. The direct radiative capture rates on these nuclei depend sensitively on the properties of low-lying states—such as excitation energies, spins, parities, electromagnetic transition probabilities, and single-particle spectroscopic factors—and typically cannot be accurately estimated in the absence of experimental data [Rau98]. Most of

the structural input necessary for a direct radiative neutron capture calculation can be determined experimentally from a measurement of the (d,p) reaction to low-lying states involving the same initial and final nuclei as the (n,γ) reaction. The properties of these states give clues as to which states are important, and how the direct capture should proceed.

1.3 Experimental aims

The two nuclei at the focus of this work, ^{83}Ge and ^{85}Se, both have 51 neutrons, are short-lived radioactive species (the half-lifes against β decay: ^{83}Ge, $t_{1/2} = 1.85$ s; ^{85}Se, $t_{1/2} = 31.7$ s), and have more neutrons than the last stable isotopes for each element (i.e., they are neutron-rich). The pre-existing data on each nucleus are sparse. The mass of ^{85}Se has been measured [Aud03], along with energies of electromagnetic transitions between states following the population of these states by the β decay of ^{85}As [Omt91]. At the time of this measurement, the only known property of ^{83}Ge was its half-life [Win88]. Since then, a β decay study of ^{83}Ga has tentatively identified two electromagnetic transitions associated with ^{83}Ge [Per03]. Figure 1.4 compares some of the known properties of the first two states in the even $Z \leq 40$, $N = 51$ isotones.

The low-lying excitations of ^{83}Ge and ^{85}Se were populated by transferring a neutron onto the radioactive, closed-shell nuclei ^{82}Ge and ^{84}Se in two measurements of the (d,p) reaction. The (d,p) neutron transfer reaction has been used extensively in nuclear structure studies in the past because of its relative simplicity and selectivity

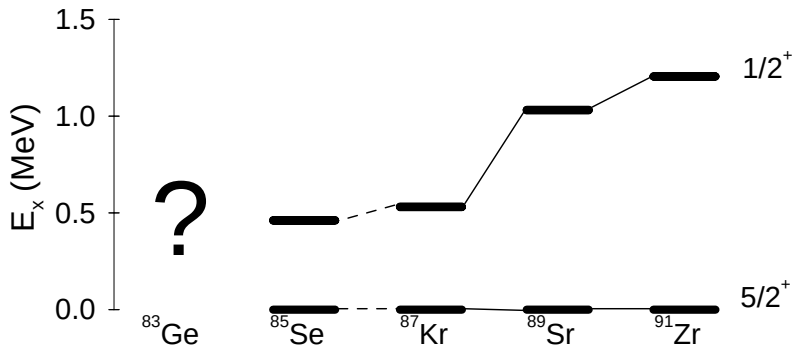

Figure 1.4: Known properties of the ground and first-excited states of even $Z \leq 40$, $N = 51$ isotones [Bha05, Omt91]. Dashed lines to the states of ^{85}Se indicate the uncertainty in level assignments.

in populating single-neutron excitations in nuclei [Sat83]. Chapter 2 describes how direct reactions of this type are used, and specifically in Sect. 2.2, the spectroscopic utility of the (d,p) reaction is discussed.

In a literature search, the first measurement of the (d,p) reaction in inverse kinematics was a proof-of-principle design with a stable beam, measuring the ^{2}H(^{136}Xe,p)^{137}Xe reaction [Kra91b]. The authors showed that a (d,p) measurement could be performed with adequate resolution, despite the situation of inverse kinematics. Some of the special considerations of performing an inverse kinematics measurement are described in detail in Sects. 3.2, 4.1, and 4.2. A measurement of the ^{2}H(^{56}Ni,p)^{57}Ni reaction was performed by another group [Reh98], showing that useful measurements can also be made with low intensity, radioactive beams.

The (d,p) measurements on ^{82}Ge and ^{84}Se are unique in the sense that these are the first measurements of their kind with radioactive, neutron-rich species that have particular relevance to the r-process and the structure of exotic nuclei near closed shells. The aim of this work is to provide spectroscopic information for the low-lying

levels of ^{83}Ge and ^{85}Se that will help to determine how the shell structure behaves in exotic nuclei with increasing neutron-richness near ^{78}Ni (see Fig. 1.4), and what modifications might be necessary for neutron capture calculations related to r-process nucleosynthesis.

1.4 Structure of the dissertation

The structure of the remainder of the dissertation is as follows:

Chapter 2 introduces the reaction theory formalism that is needed for the spectroscopic analysis of the data, and the similar formalism for direct radiative neutron capture calculations.

Chapter 3 gives an overview of the radioactive ion beam production and delivery, and descriptions of the targets, detectors, and experimental techniques used in the measurements.

The data and results of the ^{2}H(^{82}Ge,p)^{83}Ge and ^{2}H(^{84}Se,p)^{85}Se reaction measurements are presented in Chapter 4.

The implications of the two measurements are discussed in Chapter 5, particularly with regard to spectroscopic strengths and masses of exotic nuclei, both important in astrophysical contexts.

In the final chapter, the results and outcomes of the work of the dissertation are summarized, and some future directions for this research are outlined.

Chapter 2

Direct Reaction Theory

The ^{82}Ge and ^{84}Se(d,p) reactions were measured to determine the spectroscopic properties and level assignments of low-lying states in the $N = 51$ isotones via the analysis of the energies and angular distributions of the reaction protons. This chapter contains a very rudimentary formalism for the theory of direct nuclear reactions as analyzed in the distorted-waves approach[1], a discussion relating experimental observables to the theory, and a brief description of models and computer codes that implement that theory. These tools are used directly in the analysis of the data presented in Chap. 4. The chapter concludes with an overview of the theory of direct radiative capture calculations.

2.1 Overview of distorted-wave direct reaction theory

2.1.1 Preliminaries

The goal of direct reaction theory is to describe the transition from one partition of nuclei, $\alpha = a + A$, to another partition, $\beta = b + B$. In standard nuclear reaction

[1]The discussion and notation of Sect. 2.1 are taken directly from [Sat83]. Unless otherwise noted, all material presented here is from that reference.

notation, this transition is written as $A(a,b)B$.

The internal states of a given nucleus or partition are given by the wavefunctions $\psi_i(x_i)$, where the internal coordinates are denoted x_i. If the ψ_i refers to a partition, the wavefunction is the product of the internal states of the nuclei in that partition, e.g.:

$$\psi_\alpha(x_\alpha) \equiv \psi_a(x_a)\psi_A(x_A). \tag{2.1}$$

The eigenfunctions, ψ_i, are solutions to the Schrödinger equations governed by the internal Hamiltonians, H_i, with eigenenergies, ε_i:

$$H_\alpha\psi_\alpha \equiv (H_a + H_A)\psi_\alpha = \varepsilon_\alpha\psi_\alpha, \tag{2.2}$$

$$H_a\psi_a = \varepsilon_a\psi_a, \quad H_A\psi_A = \varepsilon_A\psi_A. \tag{2.3}$$

The Hamiltonian of the system, referred to a specific channel α, is the sum of the internal Hamiltonians of the nuclei of the partition (a and A), the kinetic energy of the relative motion of these nuclei, and their interaction with each other. In operator form,

$$H = H_\alpha + K_\alpha + V_\alpha. \tag{2.4}$$

The kinetic energy of relative motion, E_α (i.e., the eigenvalue of the operator K_α), is the difference between the *total* energy of the system, E, and the internal energies of the individual nuclei, ε_α:

$$E_\alpha = E - \varepsilon_\alpha. \tag{2.5}$$

The total wavefunction for the system is written as Ψ_i, and can be expanded in terms of a complete set of eigenfunctions of the internal states of a partition:

$$\Psi_\alpha = \sum_\beta \xi_\beta(\mathbf{r}_\beta)\psi_\beta(\mathbf{x}_\beta). \tag{2.6}$$

The $\xi_\beta(\mathbf{r}_\beta)$ are the projections of Ψ_α onto the β channels, and describe the relative motion in these channels. The $\xi_\beta(\mathbf{r}_\beta)$, therefore, describe the transition $\alpha \to \beta$, and should have the asymptotic form

$$\xi_\beta(\vec{r}_\beta) \xrightarrow{r_\beta \to \infty} e^{i\mathbf{k}_\alpha \cdot \mathbf{r}_\alpha}\delta_{\alpha\beta} + f_{\beta\alpha}(\hat{\mathbf{k}}_\beta, \hat{\mathbf{k}}_\alpha)\frac{1}{r_\beta}e^{ik_\beta r_\beta}. \tag{2.7}$$

This has the form of an incoming plane wave in the α channel inducing an outgoing spherical wave in the β channel with a scattering amplitude, $f_{\beta\alpha}$. (The $\mathbf{k}_i$ here refer to wave vectors related to relative momenta in channel i. The $\hat{\mathbf{k}}_i$ represent unit vectors in the direction of the relative momenta.) The transition amplitude, $T_{\beta\alpha}$, is related to the scattering amplitude by

$$T_{\beta\alpha} \equiv -\frac{2\pi\hbar^2}{\mu_\beta} f_{\beta\alpha} \tag{2.8}$$

where $\mu_{\beta\alpha}$ is the reduced mass of the β partition. The differential cross section for the reaction $A(a,b)B$ is proportional to the square of the modulus of the transition amplitude:

$$\frac{d\sigma_{\beta\alpha}}{d\Omega} = \frac{\mu_\alpha \mu_\beta}{(2\pi\hbar^2)^2}\left(\frac{k_\beta}{k_\alpha}\right)\left|T_{\beta\alpha}(\mathbf{k}_\beta, \mathbf{k}_\alpha)\right|^2. \tag{2.9}$$

The full, formal expression for the transition amplitude can be derived in this incident plane-wave case from the Schrödinger equation governing the reaction,

$$(E - H_\beta - K_\beta)\Psi_\alpha^{(+)} = V_\beta \Psi_\alpha^{(+)}. \tag{2.10}$$

Projecting onto the β channel by multiplying from the left by $\psi_\beta^*(x_\beta)$, and integrating over the x_β with the use of Eqs. 2.2, 2.5, and 2.6, yields:

$$(E_\beta - K_\beta)\xi_\beta(\mathbf{r}_\beta) = \left(\psi_\beta \middle| V_\beta \middle| \Psi_\alpha^{(+)}\right) \equiv \int \psi_\beta^*(x_\beta) V_\beta(\mathbf{r}_\beta, x_\beta) \Psi_\alpha^{(+)}\, dx_\beta. \tag{2.11}$$

The formal solution to Eq. 2.11 is found using standard Green's function techniques ([Byr70], [Sak94]), and is:

$$\xi_\beta(\mathbf{r}_\beta) = e^{i\mathbf{k}_\alpha \cdot \mathbf{r}_\alpha} \delta_{\alpha\beta} - \left(\frac{\mu_\beta}{2\pi\hbar^2}\right) \int \frac{e^{ik_\beta |\mathbf{r}_\beta - \mathbf{r}'_\beta|}}{|\mathbf{r}_\beta - \mathbf{r}'_\beta|} \left(\psi_\beta \middle| V_\beta \middle| \Psi_\alpha^{(+)}\right)\, d\mathbf{r}'_\beta. \tag{2.12}$$

In the limit $r_\beta \gg r'_\beta$, the term $|\mathbf{r}_\beta - \mathbf{r}'_\beta| \approx r_\beta - \hat{\mathbf{k}}_\beta \cdot \mathbf{r}'_\beta$, leading to the asymptotic form of $\xi_\beta(\mathbf{r}_\beta)$. Comparison with Eq. 2.7 reveals the transition amplitude to be

$$\begin{aligned} T_{\beta\alpha}(\mathbf{k}_\beta, \mathbf{k}_\alpha) &= \iint e^{-i\mathbf{k}_\beta \cdot \mathbf{r}'_\beta}\, \psi_\beta^*(x_\beta) V_\beta(\mathbf{r}'_\beta, x_\beta) \Psi_\alpha^{(+)}(\mathbf{k}_\alpha)\, dx_\beta\, d\mathbf{r}'_\beta \\ &\equiv \left\langle e^{-i\mathbf{k}_\beta \cdot \mathbf{r}'_\beta}\, \psi_\beta \middle| V_\beta \middle| \Psi_\alpha^{(+)}(\mathbf{k}_\alpha) \right\rangle. \end{aligned} \tag{2.13}$$

2.1.2 Introduction of distorted waves

So far, the formal solution of Eq. 2.13 is not amenable to the study of real reactions; the full wavefunction Ψ_α still appears in the transition amplitude, along with a complicated interaction potential, V_β. The distorted-waves (DW) method is introduced under the premise that elastic scattering is the most important interaction between two nuclei. The interactions that cause transitions $\alpha \to \beta$ when $\alpha \neq \beta$ are perturbations on the dominant elastic scattering in each channel. Again, the terminology of [Sat83] is used where elastic scattering includes events in which absorption occurs—some of the incident flux is removed in the nuclear interior as a result of the complicated many-body interaction there.

The DW method involves introducing an auxiliary potential, $U_\beta(r_\beta)$, into Eq. 2.11:

$$(E_\beta - K_\beta - U_\beta)\xi_\beta(\mathbf{r}_\beta) = \left(\psi_\beta \middle| W_\beta \middle| \Psi_\alpha^{(+)}\right) \tag{2.14}$$

$$W_\beta = V_\beta(\mathbf{r}_\beta, x_\beta) - U_\beta(r_\beta),$$

where W_β is the residual interaction. In principle, the auxiliary potential is arbitrary, but is chosen so as to account for the elastic scattering in the β channel. Because the elastic scattering usually includes absorption effects, U_β is generally complex.

The solutions to the homogeneous equation,

$$(E_\beta - K_\beta - U_\beta)\chi_\beta^{(+)}(\mathbf{k}_\beta, \mathbf{r}_\beta) = 0, \tag{2.15}$$

are the distorted waves, and can be used to describe the solution of Eq. 2.14. The

superscript on the $\chi_\beta^{(+)}$ indicates the asymptotic form of the waves, equivalent to Eq. 2.7. The solutions of the time-reverse of Eq. 2.15,

$$(E_\beta - K_\beta - U_\beta^*)\chi_\beta^{(-)}(\mathbf{k}_\beta, \mathbf{r}_\beta) = 0, \tag{2.16}$$

are also needed, but they can be found from the original solutions through the relationship

$$\chi_\beta^{(-)}(\mathbf{k}, \mathbf{r}) = \chi_\beta^{(+)*}(-\mathbf{k}, \mathbf{r}). \tag{2.17}$$

Equation 2.14 is solved with Green's function techniques just like Eq. 2.11, leading to the DW transition amplitude

$$\begin{aligned} T_{\beta\alpha}(\mathbf{k}_\beta, \mathbf{k}_\alpha) &= T_{\beta\alpha}(\mathbf{k}_\beta, \mathbf{k}_\alpha)^{(0)}\delta_{\alpha\beta} + \iint \chi_\beta^{(-)*}(\mathbf{k}_\beta, \mathbf{r}_\beta)\, \psi_\beta^*(x_\beta)\big[V_\beta(\mathbf{r}_\beta, x_\beta) \\ &\qquad - U_\beta(r_\beta)\big]\, \Psi_\alpha^{(+)}(\mathbf{k}_\alpha)\, dx_\beta\, d\mathbf{r}_\beta \\ &\equiv T_{\beta\alpha}(\mathbf{k}_\beta, \mathbf{k}_\alpha)^{(0)}\delta_{\alpha\beta} + \big\langle \chi_\beta^{(-)*}(\mathbf{k}_\beta)\, \psi_\beta \big| W_\beta \big| \Psi_\alpha^{(+)}(\mathbf{k}_\alpha)\big\rangle, \end{aligned} \tag{2.18}$$

where $T_{\beta\alpha}(\mathbf{k}_\beta, \mathbf{k}_\alpha)^{(0)}$ is the elastic transition amplitude from U_β alone.

Until now, the presentation of the theory has been made exclusively in the *post*-form representation, where the reaction is described in terms of the potentials of the exit channel, β. But with time-reversal invariance, the transition amplitudes for the reactions $A(a,b)B$ and $B(b,a)A$ are equivalent (up to a phase). All of the previous equations could have been derived in the *prior*-form representation with potentials describing the entrance channel, α. The point to note, and what is important for the next part of the discussion, is that the equivalent to Eq. 2.15 in the *prior* form

generates distorted waves for the entrance channel, $\chi_\alpha^{(+)}(\mathbf{k}_\alpha)$.

The first significant approximation introduced into the DW method is from the recognition that the most important part of the total wavefunction Ψ_α is the elastic part. Because the elastic part is not completely known, it is approximated by the distorted wave in the entrance channel:

$$\Psi_\alpha^{(+)} \simeq \xi_\alpha^{(+)}(\mathbf{r}_\alpha)\psi_\alpha(x_\alpha) \approx \chi_\alpha^{(+)}(\mathbf{r}_\alpha)\psi_\alpha(x_\alpha). \tag{2.19}$$

This approximation leads to the DW non-elastic transition amplitude for the reaction $A(a,b)B$,

$$\begin{aligned} T_{\beta\alpha}(\mathbf{k}_\beta, \mathbf{k}_\alpha) &= \left\langle \chi_\beta^{(-)}(\mathbf{k}_\beta)\, \psi_\beta \middle| W \middle| \chi_\alpha^{(+)}(\mathbf{k}_\alpha)\, \psi_\alpha \right\rangle \\ &= \iint \chi_\beta^{(-)*}(\mathbf{k}_\beta, \mathbf{r}_\beta) \left(\psi_\beta \middle| W \middle| \psi_\alpha\right) \chi_\alpha^{(+)}(\mathbf{k}_\alpha, \mathbf{r}_\alpha)\, d\mathbf{r}_\alpha d\mathbf{r}_\beta. \end{aligned} \tag{2.20}$$

The second form of Eq. 2.20 shows, explicitly, the nuclear reaction contribution (the distorted waves) and the nuclear structure contribution (the matrix element of the residual interaction) to the transition $\alpha \to \beta$.

A crucial component to the distorted waves approach, therefore, is the choice of the auxiliary potentials that account for the elastic scattering—the bulk of the interaction—in both the initial and final states. The auxiliary potentials are related to scattering states just as effective interactions are related to bound states. The auxiliary potentials are usually chosen as optical model (OM) potentials. The intention of the OM is to replace the complicated many-body interaction of colliding nuclei

with simple potentials that mimic the true processes involved in elastic scattering. In practice, the OM potentials are chosen so that they describe the measured elastic scattering in both the entrance and exit channels.

The whole of the DW method in direct reaction theory is the evaluation of Eq. 2.20 in order to describe the differential cross section of Eq. 2.9. The next section examines the connections between distorted wave theory, the nuclear matrix element $\big(\psi_\beta\big|W\big|\psi_\alpha\big)$, and information that can be gleaned from experimental measurements of angular distributions.

2.2 Connections with experiment

For the rest of the discussion of the DW method, the specific transitions of single-nucleon transfer reactions will be considered. The $\alpha \rightarrow \beta$ transition is now written,

$$A + a\,(= b + x) \rightarrow b + B\,(= A + x) \tag{2.21}$$

where x is the transferred nucleon.

The transition $\alpha \rightarrow \beta$ is seen as the result of the (small) residual interaction remaining after treating the most important elastic scattering channels with distorted waves. As mentioned in the previous section, the nuclear structure physics is contained in the matrix element $\big(\psi_\beta\big|W\big|\psi_\alpha\big)$. In the *post*-form representation of W, the residual interaction is

$$W_\beta = V_{bB} - U_\beta = V_{xb}(\mathbf{r}_{xb}, \zeta_x, \zeta_b) + \Big(V_{bA}(\mathbf{r}_{bA}, \zeta_b, \zeta_A) - U_\beta(\mathbf{r}_\beta, \zeta_B, \zeta_b)\Big) \tag{2.22}$$

where the ζ_i are the internal coordinates of nucleus i (ζ_x are just the spin and possibly isospin of x), V_{xb} is the potential binding nucleus $a(= x + b)$, and $(V_{bA} - U_\beta)$ is the remaining effective interaction. The terms in W can cause excitations in the corresponding nuclei that they refer to, but these excitations are usually neglected. Then W commutes with ψ_a and ψ_A, and the matrix element is a product of overlap functions, (ψ_i, ψ_j) and W:

$$\begin{aligned}\left(\psi_b\psi_B\middle|W\middle|\psi_a\psi_A\right) &= \int \psi_b^*\psi_a\,\psi_B^*\psi_A\,W_\beta\,d\zeta \\ &= (\psi_b,\psi_a)\,(\psi_B,\psi_A)\,W,\end{aligned} \tag{2.23}$$

where the integration is over all internal coordinates, ζ_i.

The overlap functions, $\phi_i^j \equiv (\psi_i, \psi_j)$, have a special significance. They are the projections of the state i onto the state j, e.g.:

$$\psi_B(\mathbf{r}_{xA}, \zeta_x, \zeta) \propto \sum_{A,\ell j} \psi_A(\zeta)\phi^B_{A\ell j}(\mathbf{r}_{xA}, \zeta_x)\,\langle I_A j M_A m | I_B M_B\rangle$$

$$(\psi_B, \psi_A) \propto \sum_{\ell j} \phi^{B*}_{A\ell j}(\mathbf{r}_{xA}, \zeta_x)\,\langle I_A j M_A m | I_B M_B\rangle,$$

where the sum in the first equation is over all states labeled by A and the angular momenta ℓ and j, and the second sum is just over the angular momenta. The Clebsch-Gordon coefficients are for the coupling of the spin of A with j, resulting in the spin of B. A spectroscopic factor is defined as the square of the norm of an overlap function,

$$S_{\ell j}(A, x|B) \equiv \iint \left|\phi^B_{A\ell j}\right|^2 d\mathbf{r}_{xA} d\zeta_x, \tag{2.24}$$

and gives the probability that when the system B is in the state ψ_B, it will be found to be composed of the nucleus x with orbital angular momentum ℓ and total j relative to the nucleus A in state ψ_A. There is a corresponding spectroscopic factor for a composed of b and x. After a decomposition of the overlap function into a radial part, $R^B_{A\ell j}(r_{xA})$, and an angular part, the integration in Eq. 2.24 can be carried out over the spin and isospin of x (ζ_x), and over the angular coordinates, leaving

$$S_{\ell j}(A, x|B) = \int \left|R^B_{A\ell j}(r_{xA})\right|^2 r^2_{xA}\, dr_{xA}. \tag{2.25}$$

Because the DW transition amplitude is proportional to the product of the overlap functions, ϕ^a_b and ϕ^A_B (see Eqs. 2.20, 2.23, and 2.24), it is easy to see that the angular distribution calculated in the DW method is proportional to the product of the spectroscopic factors, $S_{\ell j}(A, x|B)$ and $S_{\ell j}(b, x|a)$ (see Eq. 2.9):

$$\frac{d\sigma}{d\Omega} \propto \sum S_{\ell_B j_B}(A, x|B) \cdot S_{\ell_a j_a}(b, x|a) \cdot \sigma^{DW}_{\ell_B j_B \ell_a j_a}. \tag{2.26}$$

The sum in Eq. 2.26 is taken after a multipole expansion of the transition amplitude of Eq. 2.9. That expansion and the kinematic factors of Eq. 2.9 are grouped into σ^{DW}. It is seen from Eq. 2.26 that any measurement of a transfer reaction gives information about the initial and final states together, but not absolute information about an individual state.

Before turning to the evaluation of angular distributions with DW theory, it is worthwhile to point out the connections with measured distributions. The shape

of the DW distribution is a sensitive indicator of the transferred orbital angular momentum, ℓ. When considering a (d,p) reaction, the deuteron wavefunction (neglecting the small D-state component) is usually treated explicitly in the calculation, and the spectroscopic factor $S(p,n|d) = 1$. The calculated distribution is fit to the measured differential cross section and the normalization of the DW calculation to the measured data gives the spectroscopic factor $S_{\ell j}(A,n|B)$.

A critical assumption is made in the calculation before comparing to data. The radial part, R_A^B, of the overlap function ϕ_A^B (Eqs. 2.24 and 2.25), is assumed to be of the form of a single-particle bound-state wavefunction:

$$R_{A\ell j}^B(r_{xA}) \approx [S_{\ell j}]^{1/2}\, \varphi_{\ell j}(r_{xA}) \tag{2.27}$$
$$\int \left|\varphi_{\ell j}(r_{xA})\right|^2 r_{xA}^2\, dr_{xA} = 1.$$

Because of this assumption, any extracted spectroscopic factor is meaningless unless the bound-state wavefunction is also given. The wavefunction is usually generated from the geometry of a Woods-Saxon potential well (see Sect. 2.3), and, therefore, is a model-dependent quantity. The validity of this approximation is the subject of Sect. 2.4.

2.3 Optical model and DW computer codes

Thankfully for the experimentalist, generous theorists have developed computer codes that calculate the DW differential cross sections, Eq. 2.9 (e.g. [Iga, Kun]). When

calculating for transfer reactions, the codes take as input the geometrical forms of OM potentials for both channels, the spin of each nucleus, the angular momentum transfers, and the final bound-state potential parameters. The OM potentials are usually given with Woods-Saxon forms [Per76]:

$$\begin{aligned} U(r) = V_c - V f(x_0) + \left(\frac{\hbar}{m_\pi c}\right)^2 V_{so} \left(\ell \cdot \sigma\right) \frac{1}{r} \frac{d}{dr} f(x_{so}) \\ - i\left[W f(x_W) - 4 W_D \frac{d}{dx_D} f(x_D)\right] \end{aligned} \tag{2.28}$$

where

$$\begin{aligned} V_c &= ZZ'e^2/r, \quad r \geq R_c \\ &= \left(ZZ'e^2/2R_c\right)\left(3 - r^2/R_c^2\right), \quad r < R_c \\ R_c &= r_c A^{1/3}; \\ f(x_i) &= \left(1 + e^{x_i}\right)^{-1} \text{ where } x_i = \left(r - r_i A^{1/3}\right)/a_i. \end{aligned}$$

The individual terms in the order of their appearance in the full potential, $U(r)$, describe the OM parameterization into Coulomb, real volume, spin-orbit, and imaginary volume and surface potentials. The parameters, V, V_{so}, W, and W_D, are set to the strengths of the real volume, spin-orbit, imaginary volume, and imaginary surface forms, respectively, of the Woods-Saxon potential shapes. The potential radius, r_i, and diffuseness, a_i, parameters are also set by the user.

Typically, the elastic scattering of the particles in both the entrance and exit channels is measured to determine the optical model potential parameters. However, because the OM potential is supposed to act essentially as an average interaction, the parameters are expected to change slowly over a small region of similar atomic

mass A, atomic number Z, and energy E [Sat83]. Several studies have determined phenomenological relationships between the potential parameters and A, Z, and E based on fits to a number of elastic-scattering data sets (e.g. [Loh74, Bec69, Per63]). These global parameters are designed to be used over a range of nuclei and energies, and are ideal for nuclei for which elastic scattering has not been measured.

The bound-state potential also has a Woods-Saxon form with the strength adjusted to reproduce the observed binding energy of the transferred particle. The radius parameter, r, and the diffuseness parameter, a, are set arbitrarily within certain ranges ($1.15 < r < 1.3$ fm; $a \simeq 0.65$ fm) unless more information is known about the size and shape of the bound-state nucleus. It is from these assignments that spectroscopic factors are largely model dependent and acquire large uncertainties [Sat83] (see Sects. 4.3.1 and 4.3.2).

Proton angular distributions from sample calculations produced by the code TWOFNR [Iga] are presented in Fig. 2.1. The calculations are for the ^{82}Ge(d,p)^{83}Ge reaction, at a beam energy $E_{beam} = 4$ MeV/nucleon, for $\ell = 2$ and $\ell = 0$ orbital angular momentum transfers to a hypothetical state. The two curves show the distinctiveness of the shapes to the transferred ℓ, particularly the angle at which the first maximum in the angular distribution occurs. A general feature of transfer reaction distributions at energies just above the Coulomb barrier is that lower values of the transferred ℓ yield distributions that peak at more forward angles [Sat83].

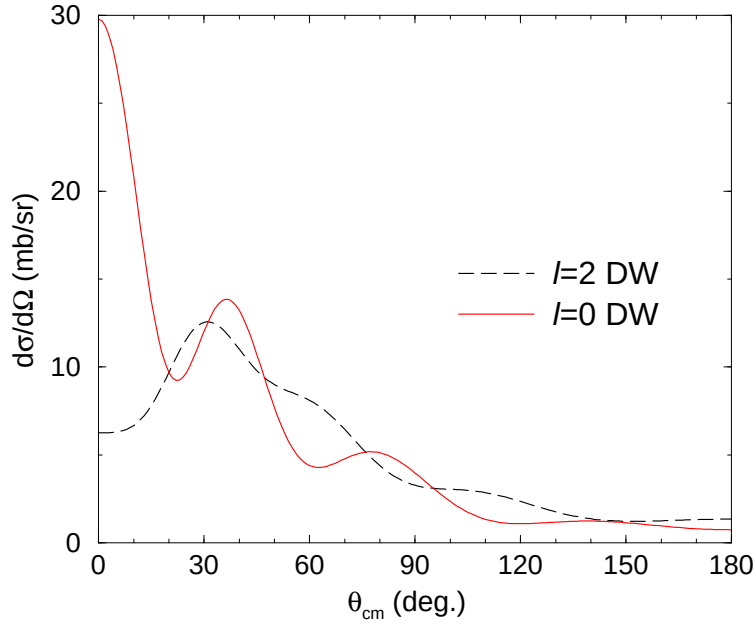

Figure 2.1: Sample DW-calculated angular distributions for the ^{82}Ge(d,p)^{83}Ge reaction at $E_{beam} = 4$ MeV/nucleon, using the code TWOFNR [Iga].

2.4 Asymptotic normalization coefficients

Several authors have pointed out that calculated transition amplitudes are rather insensitive to the parts of the overlap functions in the nuclear interior, $r < R_N$, particularly for reactions at energies below the Coulomb barrier [Rap68,Rap72,For74, Kör71, Sat83]. It has also been shown that this insensitivity to the nuclear interior can be extended to reactions above the Coulomb barrier, provided the reaction is still peripheral, or occurs at, or outside, the nuclear surface [Muk01]. But the spectroscopic factor, defined as the square of the norm of the overlap function (Eq. 2.25), acquires most of its magnitude from the nuclear interior. It is, therefore, not clear that the prescription of normalizing a DW calculation to an experimental distribution gives the spectroscopic factor. However, measured angular distributions can still be used to extract a nearly model-independent quantity related to the overlap function [Rap68,

Muk01]. The discussion in the remainder of this section largely follows the notation of [Muk01].

The radial part of the overlap function of nuclei A and B, $R^B_{A\ell j}(r_{xA})$ defined in Eq. 2.25, must fall off exponentially if it is to describe the overlap properly [Sat83,Muk01]:

$$R^B_{A\ell j}(r) \xrightarrow{r>R_N} C^B_{A\ell j}\, ik\, h^{(1)}_\ell(ikr) \tag{2.29}$$

where $h^{(1)}_\ell$ is the exponentially-decaying spherical Hankel function of the first kind; $k = \sqrt{2\mu_{xB}\varepsilon_{BA}}/\hbar$ is the wavenumber associated with the binding energy ε_{BA} of nucleon x within B; and $C^B_{A\ell j}$ is defined as the asymptotic normalization coefficient (ANC) [Muk01]. (Equation 2.29 is valid when the transferred x is an uncharged particle such as a neutron.) The ANC is the amplitude of the tail of the bound-state overlap function, and physically is related to the probability of finding nucleon x in B somewhere in the nuclear exterior region [Muk01].

The approximation of Eq. 2.27 can also be examined in the nuclear exterior region. Asymptotically, the single-particle wavefunction of Eq. 2.27 behaves as

$$\varphi^{B(sp)}_{A\ell j}(r) \xrightarrow{r>R_N} b^B_{A\ell j}\, ik\, h^{(1)}_\ell(ikr) \tag{2.30}$$

where $b^B_{A\ell j}$ is the single-particle ANC, and is determined from the geometry of the bound-state potential (the parameters r and a for the Woods-Saxon shape) [Muk01]. The relationship between the radial overlap function and the single-particle wavefunction of Eq. 2.27 is exact at large distances (both decay exponentially); therefore, the

relationship between the ANC, the single-particle ANC, and the spectroscopic factor is [Muk01]:

$$\left(C^{B}_{A\ell j}\right)^2 = S^{(sp)}_{\ell j} \cdot \left(b^{B}_{A\ell j}\right)^2 \tag{2.31}$$

The $S_{\ell j}$ as parameterized in Eq. 2.26 is actually the $S^{(sp)}_{\ell j}$ of this last equation. The angular distributions from the DW method for a peripheral (d,p) reaction are then [Muk01]:

$$\frac{d\sigma}{d\Omega} \propto \sum \left(C^{B}_{A\ell_B j_B}\right)^2 \cdot \left(C^{d}_{p\ell_d j_d}\right)^2 \cdot \frac{\sigma^{DW}_{\ell_B j_B \ell_d j_d}}{\left(b^{B}_{A\ell j}\right)^2 \cdot \left(b^{d}_{p\ell j}\right)^2}. \tag{2.32}$$

In a peripheral reaction, $\sigma^{DW}_{\ell_B j_B \ell_d j_d} \propto \left(b^{B}_{A\ell j}\right)^2 \cdot \left(b^{d}_{p\ell j}\right)^2$, meaning the nuclear model dependencies carried in the b^2 are factored out of the distributions [Muk01]. The extracted ANCs are quantities that can be used reliably across measurements without considering any underlying model assumptions, in contrast to spectroscopic factors extracted in a similar way [Muk01].

As mentioned in Sect. 2.2, an angular distribution measurement can provide information about the *product* of states; the product of spectroscopic factors (Eq. 2.26), or ANCs (Eq. 2.32), is what is determined by normalizing a DW distribution to data. However, in a (d,p) reaction, the ANC associated with the vertex $d \rightarrow n + p$ is equivalent to the single-particle ANC (the spectroscopic factor $S = 1$, neglecting the small D-state contribution), so the two cancel each other in Eq. 2.32 [Muk05].

2.5 Direct radiative capture theory

Direct radiative capture cross sections can be calculated under a formalism similar to the calculation of direct transfer reactions. In this formalism, the direct capture of a projectile (neutron), a, by a target nucleus, A, to yield nucleus B in state i is given by [Kra96]:

$$\begin{aligned}\sigma_i^{DC} &= \int d\Omega \, \frac{d\sigma_i^{DC}}{d\Omega_\gamma} \\ &= \int d\Omega \, 2 \left(\frac{e^2}{\hbar c}\right) \left(\frac{\mu c^2}{\hbar c}\right) \left(\frac{k_\gamma}{k_a}\right)^3 \frac{1}{2I_A+1} \frac{1}{2S_a+1} \sum_{M_A M_a M_B, \sigma} \left|T_{M_A M_a M_B, \sigma}\right|^2\end{aligned} \tag{2.33}$$

where S_a and I_A (M_a, M_A, and M_B) are the spins (projections) of the corresponding nuclei, μ is the reduced mass in the entrance channel, σ is the polarization of the electromagnetic radiation (± 1), k_γ is the wave number of the emitted radiation, k_a is the wave number associated with the entrance channel relative momentum, and T is the multipole expansion of the electromagnetic transition amplitude. The transition amplitudes are proportional to overlaps with the appropriate electromagnetic multipole operators, $\mathcal{O}^{E\mathcal{L}/M\mathcal{L}}$ [Kra96]:

$$I^{E\mathcal{L}/M\mathcal{L}}_{\ell_a j_a; \ell_B j_B I_B} = \int dr \; \chi_{\ell_a j_a}(r) \, \mathcal{O}^{E\mathcal{L}/M\mathcal{L}} \, U_{\ell_B j_B I_B}(r). \tag{2.34}$$

In this equation, $U_{\ell_B j_B I_B}$ is the bound-state wavefunction and $\chi_{\ell_a j_a}$ is the wavefunction describing the entrance channel. The total direct capture cross section is a sum over

all states in nucleus B, weighted by the spectroscopic factors of those states [Kra96],

$$\sigma^{\text{th}} = \sum S^i_{\ell j}\, \sigma^{DC}_i. \tag{2.35}$$

The wavefunctions can be calculated with Woods-Saxon based optical model potentials, as is done for the wavefunctions in direct transfer reactions (see Sect. 2.3). The bound-state potential strength is chosen to reproduce the binding energy of the neutron in the final nucleus. Alternatively, the potentials can be determined from a folding procedure that involves fewer free parameters [Bee96]:

$$\begin{aligned} V(R) &= \lambda V_F(R) \\ &= \lambda \iint \rho_a(\vec{r_1})\rho_A(\vec{r_2}) v_{eff}(E, \rho_a, \rho_A, s)\, d\vec{r_1} d\vec{r_2}, \end{aligned} \tag{2.36}$$

with λ a strength parameter, $\rho_{a,A}$ the mass densities of the nuclei, v_{eff} an effective nucleon-nucleon interaction such as the M3Y interaction [Kob84], and $s = |\vec{R}+\vec{r_2}-\vec{r_1}|$ with R the distance between the centers of mass of the two nuclei. The parameter λ can be adjusted to reproduce the binding energy in the case of a bound-state potential, or to reproduce elastic scattering data in the neutron entrance channel. Care must be taken that the spectroscopic factor in Eq. 2.35 is appropriately defined, as discussed in Sects. 2.4, 4.3.1, and 4.3.2. If the capture is peripheral, it is probably more appropriate to use the ANC, C^2, instead of the spectroscopic factor, and then factor out a single-particle ANC, b^2, from the individual cross sections in Eq. 2.35,

i.e.:

$$\sigma^{\text{th}} = \sum (C^i_{\ell j})^2 \cdot \frac{\sigma^{DC}_i}{(b^i_{\ell j})^2}. \tag{2.37}$$

The strongest direct transitions usually involve s-wave ($\ell = 0$) capture of the neutron, accompanied by an $E1$ (electric dipole) electromagnetic transition. Higher relative angular momentum captures are hindered by the centrifugal barrier at low neutron energies, and other electromagnetic multipolarities are typically weaker due to the properties of the multipole operators [Kra87]. The $J^\pi = 0^+$ spin of the ^{82}Ge and ^{84}Se ground states and the expected positive-parity low-lying states of ^{83}Ge and ^{85}Se prevent s-wave capture with $E1$ decay from populating these states by the conservation of angular momentum. Non-parity-changing $M1$ (magnetic dipole) γ-ray transitions can accompany s-wave capture, but are typically on the order of $50 - 100$ times weaker than $E1$ transitions [Kra87]. Therefore, p-wave capture with $E1$ γ-ray emission is expected to be the most important contribution to the direct neutron capture to both ground and first-excited states in ^{83}Ge and ^{85}Se.

Chapter 3

Facility and Equipment

The investigation of spectroscopic properties of neutron-rich nuclei in this work follows the traditional technique of measuring (d,p) reactions. However, the methods of that technique have been modified as a result of measuring nuclei very far from stability. This chapter will describe the facility used to provide radioactive ion beams, as well as the apparatus used to measure (d,p) reactions with unstable beams.

3.1 Beam production and delivery

Neutron-rich radioactive ion beams are produced at the Holifield Radioactive Ion Beam Facility (HRIBF) at Oak Ridge National Laboratory with the isotope separation on-line (ISOL) method [Str04]. A primary proton beam from the Oak Ridge Isochronous Cyclotron bombards a thick, fibrous UC target on a high voltage platform (nominally held at -160 kV), inducing fission of the uranium. The fission fragments so produced diffuse through the target material and effuse through a transport line to an electron-beam-plasma ion source (EBPIS), and are ionized [Car97]. The positively charged ions "fall out" of the plasma and are accelerated by an extractor held at a negative potential with respect to the platform (typically -40 kV) [Str05, Mue05].

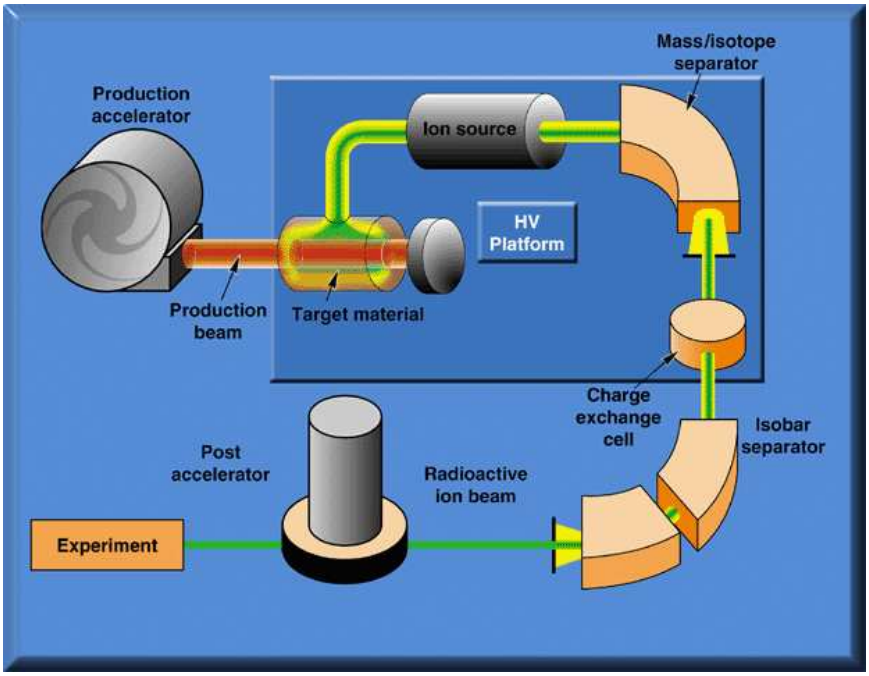

Figure 3.1: Beam production and delivery at the HRIBF. Figure taken from [HRI05].

The ions are magnetically mass analyzed and continue to a cesium-vapor charge exchange cell to make singly-charged negative ions for injection into the 25-MV tandem electrostatic accelerator. Figure 3.1 is a schematic of these components.

At the positively-charged terminal, the ion beam passes through a carbon stripper foil, removing a number of electrons and leaving positive ions. The beam is then sent around a 180° bending magnet and accelerated down the high energy side of the tandem. If necessary, the beam can be "double stripped" by another foil about a third of the way down from the terminal on the high-energy side. Removing more electrons increases the energy to which the beam is accelerated. The $A = 82$ and $A = 84$ isobaric beams used in this dissertation were single-stripped and accelerated to 4 and 4.5 MeV/nucleon, respectively.

It has been shown that for some group 4A elements of the periodic table (e.g. Sn,

Ge) transport of the isotope of interest as a sulfide molecule through the ion source enhances the relative isobaric purity of the beam [Str03]. Hydrogen sulfide (H_2S) is introduced into the transfer line on the injector platform, just before the EBPIS. The sulfide molecules so created are ionized and mass analyzed in the same way as a normal beam. The sulfide molecules are then broken up in the charge exchange cell and made into singly-charged negative ions for injection into the tandem [Str05]. The advantage of this technique is that neighboring chemical groups of elements do not as readily form sulfide molecules; thus they are filtered by the magnetic mass analysis. The technique was applied to the $A = 82$ isobaric beam used in this dissertation; one isotope of interest was ^{82}Ge, a group 4A element, with the neighboring stable ^{82}Se as the major contaminant (see Sect. 4.1).

3.2 Detectors

Charged-particle spectroscopy figures prominently in the measurement of (d,p) reactions. The somewhat novel consideration in this work is the need to do the experiment in inverse kinematics. The (d,p) reaction is to occur on short-lived unstable nuclei that cannot be made into targets. The only recourse is to make the radioactive species the beam and fashion a target out of the lighter deuterated material. The kinematics dictates where to place detectors and what type to use.

In normal kinematics the center-of-mass (c.m.) frame is essentially that of the stationary, heavy target. In inverse kinematics, in order to reproduce the same energy conditions in the reaction as a normal measurement, the heavy beam must be

accelerated to $\sim$ 10 % the speed of light. The c.m. frame is, therefore, also moving at $\sim$ 10 % the speed of light with respect to the laboratory frame where the measurement is performed. The major effect of this inversion is to forwardly focus all of the heavy reaction products in the laboratory frame. The beam and beam-like recoils after passing through the target follow essentially the direction as the beam upstream from the target. If the recoils are to be detected, they must be distinguished from the rest of the heavy ions by some other means than the spatial separation after passing through the target. The protons of interest are detected at backward laboratory angles (forward c.m. angles in normal kinematics), but over a larger angular range than if the measurement were in normal kinematics. There are hardly any reaction products other than the protons that are emitted at backward laboratory angles, but the protons suffer from a large kinematic shift in their energies due to the rapid change in proton energy as a function of laboratory angle. The detection of the protons must, therefore, involve good energy and angle resolution, and a large angular coverage, with less emphasis on separating protons from other types of charged particles in this measurement.

The rest of this section details the charged particle detection systems used in the measurements of this dissertation.

3.2.1 Ionization chamber

The radioactive beams that are delivered to the target (see Sect. 3.1) are usually highly contaminated. The fissioning of uranium in the ISOL production technique

yields numerous fission fragments, all at once. The very small mass differences between wanted and unwanted medium-mass isotopes preclude electromagnetic separation in their delivery, and chemical separation is not perfect, either. These contaminants will induce reactions with the target material with similar reaction kinematics as the isotope of interest. It is necessary, then, to be able to distinguish the transfer reactions caused by specific nuclei.

As incident charged particles pass through material, energy is lost in collisions with atomic electrons at a rate according to Bethe's well known formula [Kno00]

$$-\frac{dE}{dx} = \frac{4\pi e^4 z^2}{m_0 v^2} NZ \left[\ln \frac{2\gamma^2 m_0 v^2}{I} - \beta^2 \right] \tag{3.1}$$

where ze and v are the incident radiation's charge and relative speed; N and Z are the number density and atomic number of the stopping material; m_0 is the electron mass; γ and β are the Lorentz quantities formed from the relative speed; and I is the average ionization potential of the stopping material, usually treated as an experimentally determined parameter. For nonrelativistic particles ($\beta \ll 1$), the stopping power can be written [Kno00]:

$$-\frac{dE}{dx} = A \, \frac{mz^2}{E} \, \ln \frac{BE}{m}. \tag{3.2}$$

Here, m is the mass of the charged-particle, and A and B are constants that depend on the absorber material. The logarithmic term is masked by the leading dependencies on mz^2 and $1/E$. This relationship is exploited in the detection and identification of

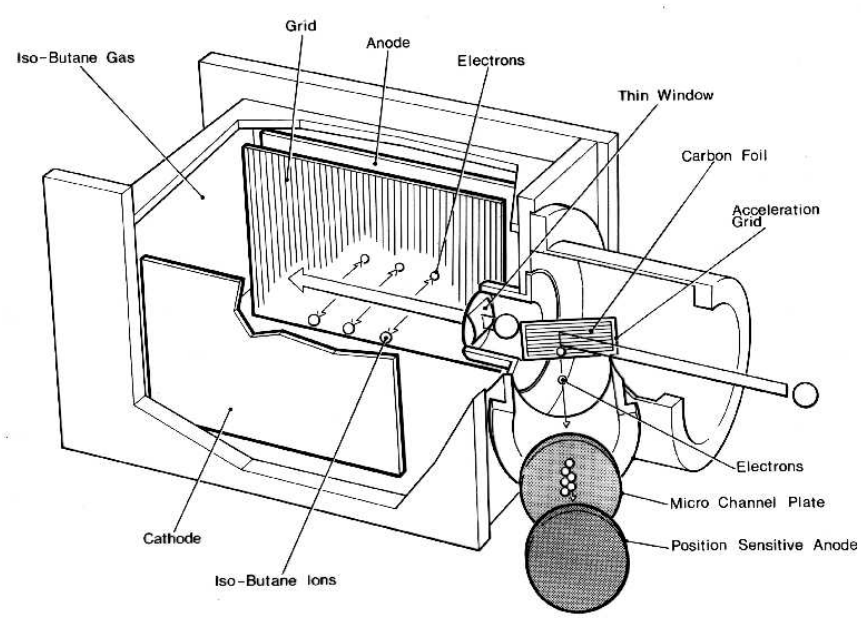

Figure 3.2: Diagram of the ionization chamber. The carbon-foil micro-channel plate detector and associated electronics were not used in this dissertation. Isobutane as a fill gas was replaced with tetrafluoromethane (see text). Figure taken from [Bar00].

the beam contaminants.

A segmented, gas-filled ionization chamber, formerly from the Daresbury Recoil Separator [Jam88], was used in the present measurements to identify the beam species after passing through the target. In the ionization chamber, the energy lost by the incident particle is observed via the ionization of the fill gas in the wake of the particle track. The geometry is such that the particle tracks are parallel to the electrodes collecting the ionization charges (Fig. 3.2). With the application of an external potential gradient across the electrodes, the ionized electrons are swept towards the segmented anodes, and the remaining ions of the fill gas are swept to the cathode.

The sensitivity of the detector to different atomic species is a result of the strong dependence with atomic number of the stopping power (Eq. 3.2). The fill-gas pressure

is chosen so that the incident charged particles stop within the volume of the detector but not before traversing the length of at least the first anode. In this way, the total energy of the particles can be measured simultaneously with the rate of energy loss. Different amounts of energy are deposited in the first section of the detector, directly related to the different energy loss rates; thus, a larger signal is generated in the first anode for charged particles with the same initial energy but higher atomic number. The different atomic species can be clearly identified in a plot of the energy deposited in the first anode, ΔE, versus the total energy deposited in the ionization chamber, E (c.f. Fig. 4.1 and Fig. 4.8).

The signal from the detector can have two different time components, reflecting the different drift times for ions and electrons. The magnitude of the individual components of the signal are each dependent on the position of the initial interaction. The *combined* amplitude of the electron- and ion-induced signal is proportional to the energy deposited near the electrodes [Kno00]. However, as is described below, it is sometimes advantageous to consider just the faster, electron-induced signal. To maintain the proportionality between the pulse amplitude and deposited energy, a Frisch grid is used [Kno00]. The grid is situated $\sim$1 cm in front of the anodes and is held at ground potential with respect to the anodes and cathode. The grid prevents a change in voltage on the anodes until the electrons cross into the gap between the grid and anodes. The rise time of the anode signal is, therefore, a function of only the electron drift velocity between the grid and anode, independent of track position. Independent signals can be read off from both the cathode and anodes, the effect of

the motion of the ions being shielded from the anode by the grid [Kno00]. Because every electron still counts equally in the formation of a signal, the pulse amplitude is once again directly related to the number of electron-ion pairs formed from the deposition of energy.

In the two measurements of this dissertation, the ionization chamber was also used to monitor the amount of beam current. The kinematics are such that nearly 100% (> 99 %) of the beam and beam-like recoils are collected by the detector, so a direct integration of beam particles was possible. The expected rates for radioactive ion beams are low compared to stable beams, but still higher than what are usually encountered in charged-particle detectors. The ionization chamber had to handle a high beam rate—on the order of 10^5 particles per second—with minimal losses to the pile-up of pulses.

A severe count rate limitation is imposed by the inherent charge collection time of the ionization chamber. If the electrons generated by the interaction of the radiation within the detector are slow to generate the output pulse, there is a greater probability that another radiation event will occur before the first is fully processed. The result is the pile-up of the two pulses, and the information of both signals is essentially lost. Pile-up is present in every counting application, but the effect is obviously minimized by reducing the signal rate, or decreasing the response time of the detector and the processing time of the subsequent electronics. The pulse-shaping amplifier, coupled to the detector's preamplifier and used to generate a pulse that is easy to digitize, is usually set to integrate the collected charge with a time constant that is long compared

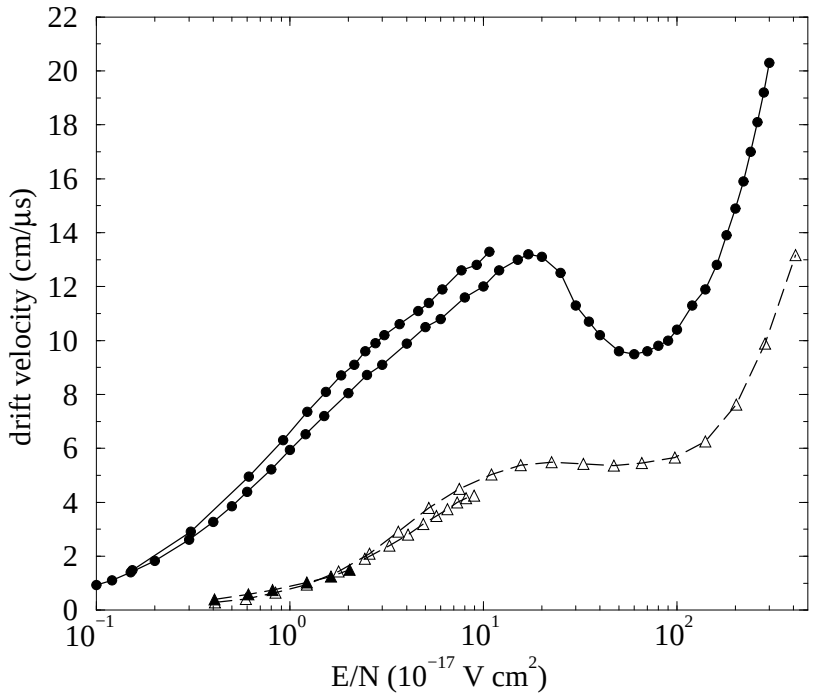

Figure 3.3: Electron drift velocities as functions of density-reduced electric field strength using CF_4 (circles and solid lines [Hun88, Chr79]) and i-C_4H_{10} (triangles and dashed lines [Chr66, Pal75, Bia99]) fill gases. Solid symbols are data points, open symbols are calculations.

to the rise time of the preamplifier signal [Kno00]. If the preamplifier's signal rise time can be shortened, the shaping time can be shortened, and the probability for pile-up is reduced. However, diminishing the integration time constant has a negative effect on the pulse height (energy) resolution that can be achieved [Kno00].

Normally, the ionization chamber is filled with isobutane (i-C_4H_{10}). We have instead experimented with the fill gas tetrafluromethane (CF_4) for its "fast gas" properties [Hun88, Chr79]. The electron drift velocities in both CF_4 and i-C_4H_{10} are shown in Fig. 3.3. At every density-reduced electric field strength—the electric field normalized by the gas number density—the drift velocity in CF_4 is higher. In our tests with tetrafluoromethane, we observed a best preamplifier rise time of 100 ns,

compared to 200 ns with isobutane under similar conditions. The stopping powers of the two gases are also comparable. Based on these results, CF_4 was chosen as the fill gas for both experiments, and taking advantage of the faster signal rise time, the shaping time of the amplifier was shortened to 250 ns. The ionization chamber was filled with $\sim$ 70 Torr of CF_4, and operating voltages put the density-reduced electric field strengths at 3-8$\times 10^{-17}$ V$\cdot$cm^2.

3.2.2 Silicon strip detectors

The proton reaction products from the (d,p) reactions need to be measured with good energy and angular resolution in an array of detectors covering a large solid angle at backward angles in the laboratory. In the present measurements, a large area array of silicon semiconductor detectors was used [Bar01]. The technology of these detectors exploits the properties of semiconductor junction diodes.

At an interface between the two types of doped silicon crystals, the majority charge carriers—electrons for n-type and holes for p-type—see a large concentration gradient. Because of the gradient, the charge carriers will diffuse across this junction and fill vacancies in the opposite-type layer until an equilibrium is established. The diffusion leaves behind immobile crystal impurities that have net charges associated with them—positive charges with the removal of an electron and negative charges with the removal of a hole. The net space-charge distribution establishes an electric field across the junction, directed from the n-type to the p-type, that maintains the equilibrium by preventing further migration of the charge carriers [Kno00].

The properties of these semiconductor junction diodes are exploited to fashion charged-particle detectors. The region of the space-charge electric field is depleted of charge carriers that can participate in the conduction of a current, thus it is highly resistive. Free electrons and holes created near the junction are easily swept to opposite sides of this depletion region by the strong electric field. Ionizing radiation that passes through the depleted volume creates electron-hole pairs that behave analogously to the electron-ion pairs formed in the gas-filled ionization chamber of Section 3.2.1. The drifting electron-hole pairs are collected on electrodes bounding the active volume, generating the detector signal. With the application of a reverse bias across the junction, the space-charge distribution is enhanced, the electric field is made stonger, and the depletion region grows. Normally, the reverse bias is applied so that the depletion region extends throughout the whole volume of the silicon [Kno00].

The achievable energy resolution of silicon semiconductor detectors is typically much better than that of the gas-filled ionization chamber. The reason is mainly a matter of counting statistics. The average energy needed to create an electron-hole pair in silicon is 3.62 eV, whereas the average energy needed to create an electron-ion pair in the ionization chamber is $\sim$ 30 eV [Kno00]. Thus, for the same energy deposited in the detectors, more charge carriers are available to generate a signal in the silicon detector, reducing the statistical fluctuation of that signal. Figure 3.4 is an energy calibration spectrum for one of the silicon strips used in this dissertation. The α particles emitted by a ^{244}Cm alpha source have energies of 5.805 MeV (branching ratio of 76%) and 5.763 MeV (branching ratio of 24%). The full width

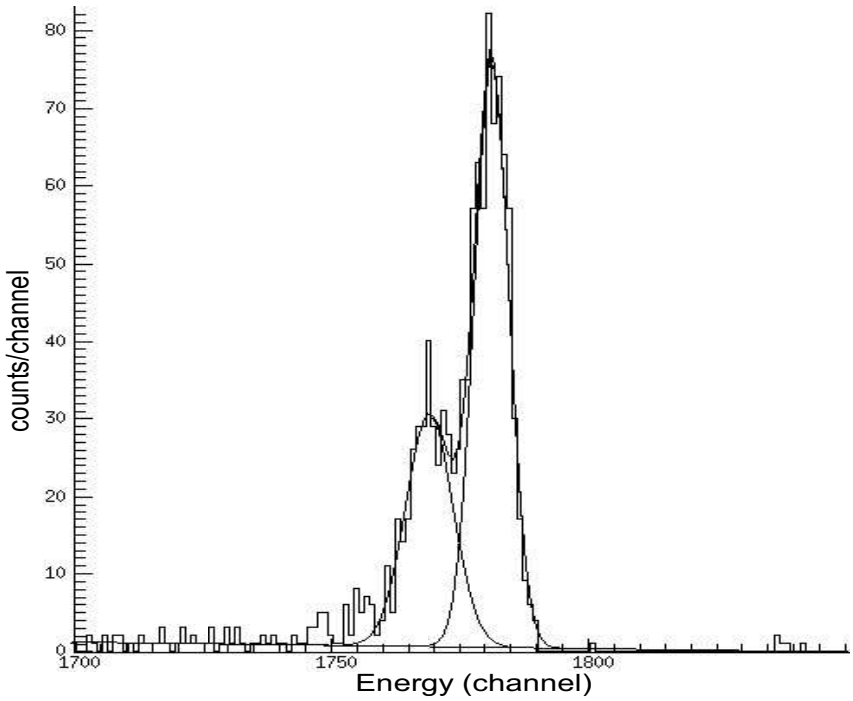

Figure 3.4: Single SIDAR strip calibration spectrum showing the two α lines at 5.805 MeV and 5.763 MeV with a peak fit for each.

at half-maximum (FWHM) of the peaks shows a 0.5% energy resolution (29 keV at 5.805 MeV).

In the two experiments of this dissertation, a large area silicon detector array (SIDAR) was used to detect protons from the reactions [Bar01]. The array consists of 6 MSL-type YY1 wedges with 16 annular strips per wedge, manufactured by Micron Semiconductor, Ltd. [Mic05] (Fig. 3.5). The wedges are arranged in a "lampshade" geometry—a six-sided cone where each detector is equally spaced azimuthally and tilted forward 43° from the perpendicular to the beam axis. Table 3.1 summarizes geometrical and operatational characteristics for an individual wedge. Wedges of 300 μm and 500 μm thicknesses were used. The array is centered on the beam axis and is moved relative to the target position to cover the desired angular range.

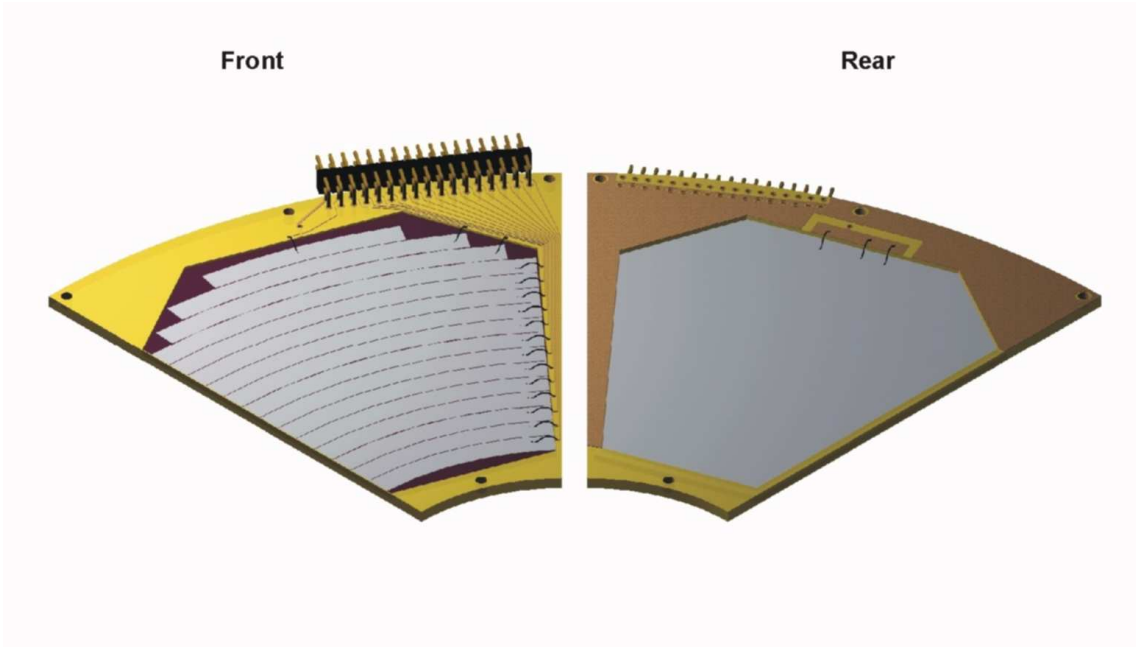

Figure 3.5: MSL-type YY1 wedge. Figure from Micron Semiconductor, Ltd. [Mic05].

In order to measure proton angular distributions, or differential cross sections with respect to solid angle, it is necessary to know the geometric efficiency of each strip of the array. The procedure for measuring the solid angle is straightforward. An α source with a known decay rate, R, is placed at the target position, illuminating the silicon array. The number of α particles hitting each strip, N, is recorded simultaneously with the elapsed time, Δt. The ratio of the recorded α rate in a strip to the calibrated rate into 4π steradians is the fraction of the total solid angle subtended by the strip, or:

$$\Delta\Omega = 4\pi \cdot \frac{N}{\Delta t \cdot R} \tag{3.3}$$

The calibrated ^{244}Cm source that was used was somewhat recessed in its holder. When placed at the target postion, and with the close geometry of SIDAR, the 3 or 4 outermost strips of SIDAR on each wedge were not illuminated. A computer program

Table 3.1: Geometric and operating parameters for the MSL-type YY1 wedge silicon detector [Mic05, Dav00].

Number of strips:	16	
Strip pitch:	5.0 mm	
Strip width:	4.9 mm	
Inner radius (active area):	50.0 mm	
Outer radius (active area):	129.9 mm	
Inner radius (PCB):	40.0 mm	
Outer radius (PCB):	145.0 mm	
PCB ϕ range:	45°	
Strip ϕ range (in flat mode):	strip	ϕ range (deg.)
	1	39.82
	2	40.00
	3	40.17
	4	40.30
	5	40.42
	6	40.52
	7	40.61
	8	40.69
	9	40.76
	10	40.82
	11	40.88
	12	40.93
	13	40.98
	14	35.89
	15	28.75
	16	18.91
Depletion voltage (300 μm):	$\sim$ 30 V	

was used to calculate the subtended solid angle of all the strips. The calculations were within 2-5% of the values determined for the α-illuminated strips, so the calculated values were used for the geometric efficiencies of the outermost strips.

3.3 Targets

The targets used for the (d,p) reaction studies were thin foils of deuterated polyethylene $(CD_2)_n$. The procedure for making the $(CD_2)_n$ thin-foil targets largely follows the prescription of [Bar73]. Powdered deuterated polyethylene [1] is dissolved in a solvent of p-xylene. The thicknesses of the foils are controlled by the concentration of polyethylene in solution and the volume of that concentration deposited onto a known surface area. For example, if 1 mL of solution completely covers an area of 10 cm^2, then a solution with a concentration of 2000 mg/mL of CD_2 must be prepared to make a target of 200 $\mu g/cm^2$ thickness. The prepared solution is heated and maintained at the boiling point temperature ($\sim$ 145° C) for 5 minutes in a covered beaker. After the powder is completely dissolved and the solution has cooled to about 125° C, a small volume is pipetted onto a glass slide of known surface area that was heated on the same element during the cooling of the solution. The known volume deposited should be enough to completely cover the slide. The p-xylene evaporates from the slide leaving a thin, polymerized layer of CD_2. Another beaker is inverted over the slide to slow the evaporation of the p-xylene. The dried foil is immersed quickly in warm water then scored along an edge. The slide is held above the water

[1] powder from Cambridge Isotope Laboratories, Inc., Andover, MA

with the scored edge just on the surface. As the slide is slowly immersed again, the surface tension of the water helps to separate the foil from the slide until the whole foil floats. A target frame is brought under the floating foil, lifted out of the water with the foil in place, and allowed to dry.

We have found that the dissolved solution must boil for the full 5 minutes, otherwise complete polymerization of the powder does not occur and the resulting foil is brittle. Care must also be taken in the cooling and evaporation of the solution on the slide. Too fast of an evaporation can prevent the solution from completely covering the slide and can cause non-uniformities in the eventual foil thickness by the irregular drying over the whole surface of the slide.

The thicknesses of the foils are verified individually by measuring the energy loss in a silicon detector, ΔE, of 5.805 MeV incident α particles from a ^{244}Cm source after passing through the targets. For thin films, the energy loss is the product of the specific energy loss, or stopping power, of the incident charged particle in the target and the target thickness:

$$\Delta E = -\frac{dE}{dx} \cdot \Delta x. \tag{3.4}$$

The stopping power of α particles in polyethylene is well known [Ber00], leading to a simple determination of the target thickness, Δx.

Chapter 4

The Experiments and Data

The measurement of the ^{2}H(^{82}Ge,p)^{83}Ge reaction was performed in January-February, 2003, and the measurement of the ^{2}H(^{84}Se,p)^{85}Se reaction was completed in February, 2004. This chapter describes the reaction measurements, including data collection and calibrations, and the results.

4.1 ^{2}H(^{82}Ge,p)^{83}Ge

A 4 MeV/nucleon isobaric $A = 82$ beam bombarded a 430 μg/cm^2 CD_2 target for 5 days. The target thickness was verified after the experiment using the methods of Sect. 3.3. The measurement was performed in inverse kinematics with a heavy beam incident on a much lighter target. The heavy beam direction defines $\theta_{lab} = 0°$. This definition is, therefore, 180° different than the definition of $\theta_{lab} = 0°$ in normal kinematics, where the incident deuteron beam defines the $\theta_{lab} = 0°$ direction. In a nuclear scattering experiment with cross sections on the order of millibarns, the majority of the incident beam passes through the target unreacted or with slight deflections from collisions with atomic electrons. For the rare event of a nuclear collision, the kinematics dictates the emission angles and energies of the reaction

products. Kinematics for the $A = 82$ beam impinging on the target deuterons limits the angle of emission of beam and beam-like recoils from these reactions to $\theta_{lab} < 1.5°$. For reactions on the target carbon atoms, the recoils are limited to $\theta_{lab} < 8°$. However, the elastic scattering of heavy recoils to laboratory angles of $\theta_{lab} > 4°$ corresponds to c.m. scattering angles for the carbons (in normal kinematics) of $\theta_{cm} > 30°$. The carbon elastic scattering cross section, while not completely Rutherfordian, falls off quickly at larger scattering angles, considerably reducing the number of beam-like recoils that scatter out to the kinematic limiting angle. The ionization chamber, placed at $\theta_{lab} = 0°$ and with an acceptance of $\pm 5°$ (see Sect. 3.2), therefore, sees very nearly 100% of the beam and beam-like recoils from all reactions with the target atoms.

As discussed in Sect. 3.2.1, the ionization chamber is used to stop, count, and identify by atomic number the beam-like particles entering the active volume of the detector. Figure 4.1 shows the energy deposited by the $A = 82$ beam species in the first anode of the ionization chamber, ΔE, as a function of the total energy deposited in the detector, E. The $\Delta Z = 1$ separation clearly shows the main components of the beam. The species present were stable ^{82}Se (85%), ^{82}As (<1%), and the radioactive ^{82}Ge (15%, $t_{1/2} = 4.6$ s [Bha05]) necessary for the measurement. The total beam intensity was up to 10^5 particles per second (pps) with an average of 7×10^4 pps (10^4 pps ^{82}Ge) over the duration of the measurement.

Protons from the (d,p) transfer reaction are emitted at all angles in the laboratory. However, according to nuclear reaction theory, a manifestation of a direct transfer of

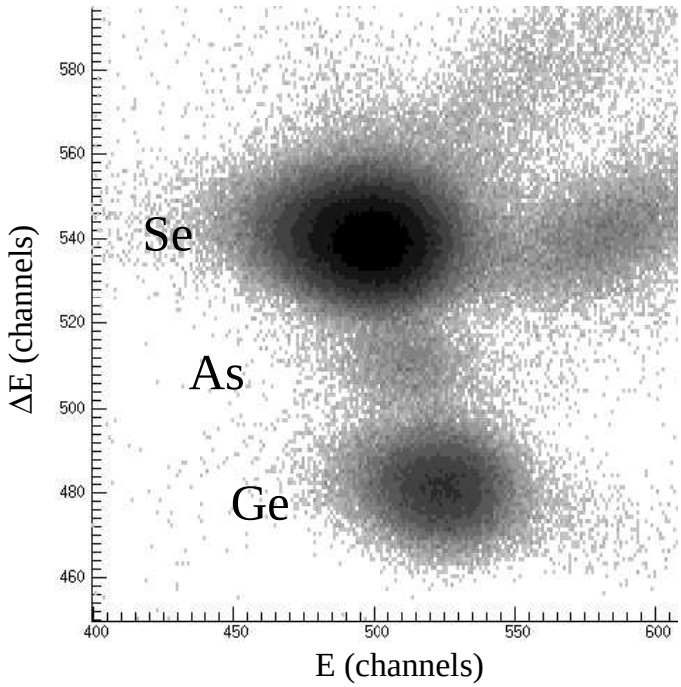

Figure 4.1: Energy loss ΔE vs. total energy E spectrum from the ionization chamber for the $A = 82$ beam.

the neutron from the deuteron to the heavy ion is a forward-peaked proton angular distribution in the center of mass frame [Sat83]. This is a consequence of the transfer being very nearly a reaction at the surface of the two nuclei (a grazing collision), with no compound nucleus formation, and very few internal degrees of freedom excited. For a direct reaction, the location in angle of the first forward peak in the proton angular distribution is also sensitive to the transferred orbital angular momentum, ℓ, to the final state [Sat83]. The forward angles described here are with respect to the *normal* kinematics, center-of-mass (c.m.) coordinate system. In the *inverse* kinematics measurement, where the c.m. is moving forward in the laboratory, these angles correspond to backward laboratory angles. The silicon detector array SIDAR (Sect. 3.2.2) was configured in the "lampshade" geometry, and placed at backward

laboratory angles subtending $\theta_{lab} = 105° - 150°$ ($\theta_{cm} \simeq 36° - 11°$) to detect transfer reaction protons.

The data were collected in event mode by the data acquisition system. The data acquistition event trigger was the logical combination of a registered charged-particle hit in SIDAR or a pre-scaled trigger from the ionization chamber. The pre-scaled ionization chamber events were recorded to get a continuous measure of the integrated beam current and beam composition. The ionization chamber pre-scaler outputs a pulse for every 2^9 registered incident charged-particles. This was necessary because while the detector can process high count-rates (up to 10^5 pps), the data acquisition system cannot. The event stream consisted of the digitized output from the analog-to-digital converters (ADCs) that transformed the linear signals from the detectors, as well as the digitized output from a time-to-amplitude converter (TAC).

The TAC outputs a pulse with an amplitude proportional to the time difference between the two input signals—one start signal and one stop signal. For time-correlated events, the TAC spectrum will show a peak corresponding to the correlated time difference. The TAC inputs in this case were a start signal from a registered silicon detector hit and a stop signal from a delayed, non-pre-scaled ionization chamber event. The delay in the stop signal was added to bring the TAC pulse amplitude up above the detection threshold. Figure 4.2 shows the TAC spectrum for the ^{2}H(^{82}Ge,p)^{83}Ge reaction measurement, with a peak indicating coincident events between the silicon detectors and ionization chamber. A low-energy threshold was applied to the proton data to generate Fig. 4.2. The width of the peak, $\Delta t \sim 80$ ns, reflects mainly

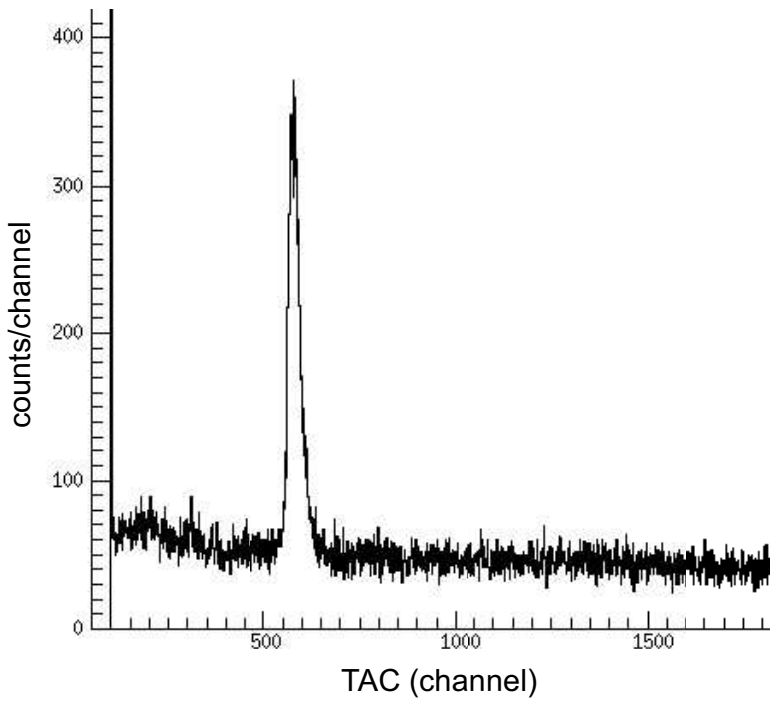

Figure 4.2: TAC spectrum for the ^{2}H(^{82}Ge,p)^{83}Ge reaction generated by a start signal from the silicon detectors and a stop signal from the ionization chamber. The silicon detectors were required to be above a low-energy noise threshold.

the spread in drift times of the electrons in the ionization chamber from the track generation point to the Frisch grid (Sect. 3.2.1).

Proton-recoil coincidences were established in the acquisition sorting software by requiring: (1) an ionization chamber event with anode signals that fell within the boundaries of a two-dimensional gate surrounding a particular beam-like species in the ΔE vs. E spectrum (Fig. 4.1); (2) a recorded hit in SIDAR; (3) and a TAC pulse that registers within the bounds of the TAC peak of Fig. 4.2. In this way, coincident spectra such as Fig. 4.3 were generated. Figure 4.3 shows the strip number versus the particle energy of events recorded by the silicon detectors in coincidence with Se [Fig. 4.3(a)] and Ge [Fig. 4.3(b)]. The kinematic bands seen in the figure correspond to states populated in the $A = 83$ systems (laboratory angle decreases with increasing

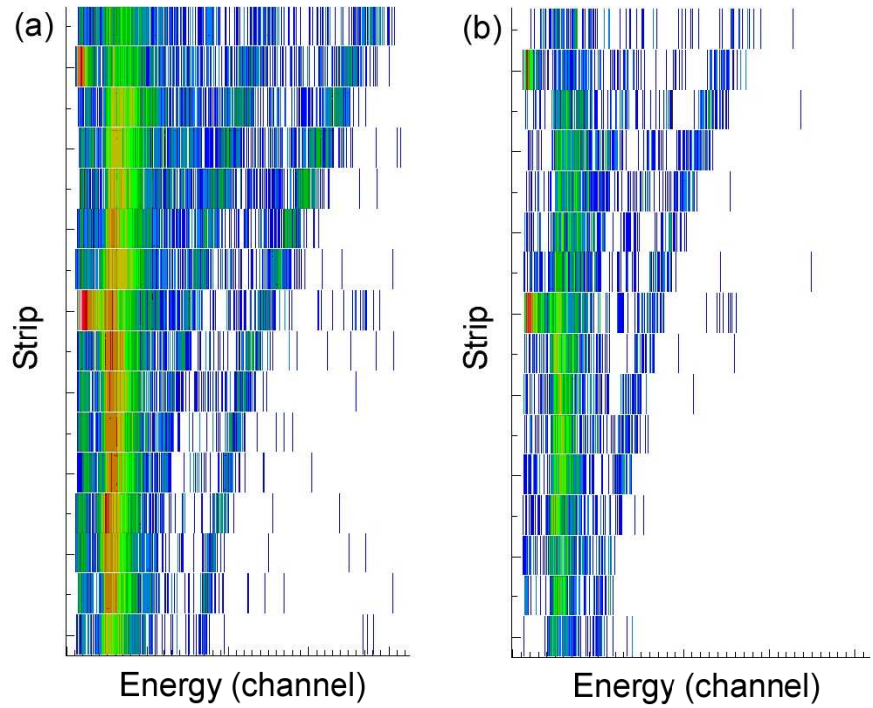

Figure 4.3: SIDAR strip number vs. proton energy in coincidence with (a) Se and (b) Ge from the $A = 82$ beam in the ionization chamber.

strip number).

Calibration of the measurement was a two-step process. The energy of the coincident protons and the laboratory reaction angle subtended by each strip of SIDAR are sufficient to extract the reaction Q-value and excitation energies of ^{83}Ge from the other known kinematic quantities (e.g. beam energy and masses of ^{82}Ge, d, and p). The energy per channel for each strip was determined from α particles emitted from a ^{244}Cm source (Sect. 3.2.2). The average angles of each strip were determined with the help of a previously published measurement. Montestruque, *et al.*, measured the ^{82}Se(d,p)^{83}Se reaction in normal kinematics and observed excitations up to 3.83 MeV [Mon78]. The most energetic band of coincident protons in Fig. 4.3(a) corresponds to an isolated doublet of states nearly equal in strength at $E_x = 540$ keV

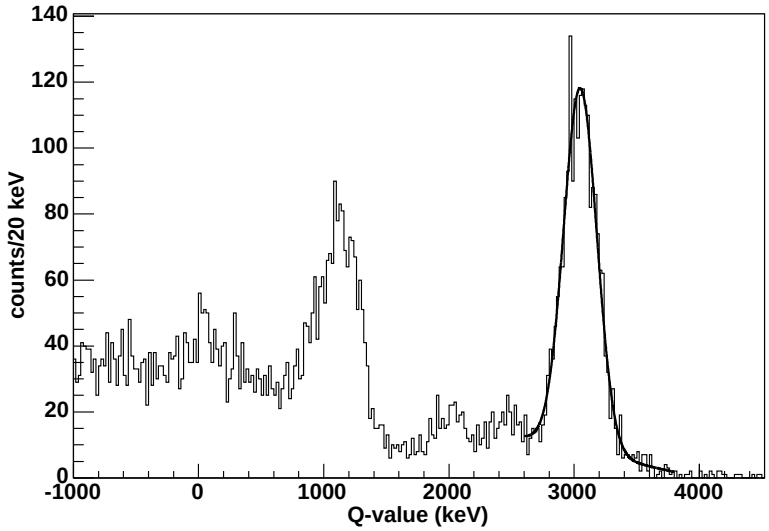

Figure 4.4: ^{2}H(^{82}Se,p)^{83}Se reaction Q-value spectrum summed over all angles. The solid line is the fit of the doublet of states at $E_x = 540$ keV and $E_x = 582$ keV. The ground-state Q-value of the reaction is $Q = 3.593$ MeV [Mon78].

and $E_x = 582$ keV (see Fig. 4.5) [Mon78]. It was unrealistic to expect that these two states could be resolved in the present measurement, so they were treated as a single state with an excitation energy of $E_x = 560$ keV. On a strip-by-strip basis, the proton energies for the doublet were used to determine the average angle at which they were measured, such that the reconstructed Q-value for this proton energy and angle corresponded to an excitation energy of $E_x = 560$ keV in ^{83}Se. Figure 4.4 is the sum over all strips of the reconstructed ^{2}H(^{82}Se,p)^{83}Se reaction Q-value spectrum, as measured concurrently with the ^{2}H(^{82}Ge,p)^{83}Ge reaction. The solid line is a fit of a gaussian peak with a linear background to the doublet giving a width of $\Delta E_{cm} \approx 300$ keV—an upper limit to the c.m. energy resolution that was achieved in the experiment. The larger widths of the higher-lying ^{83}Se excitations in Fig. 4.4

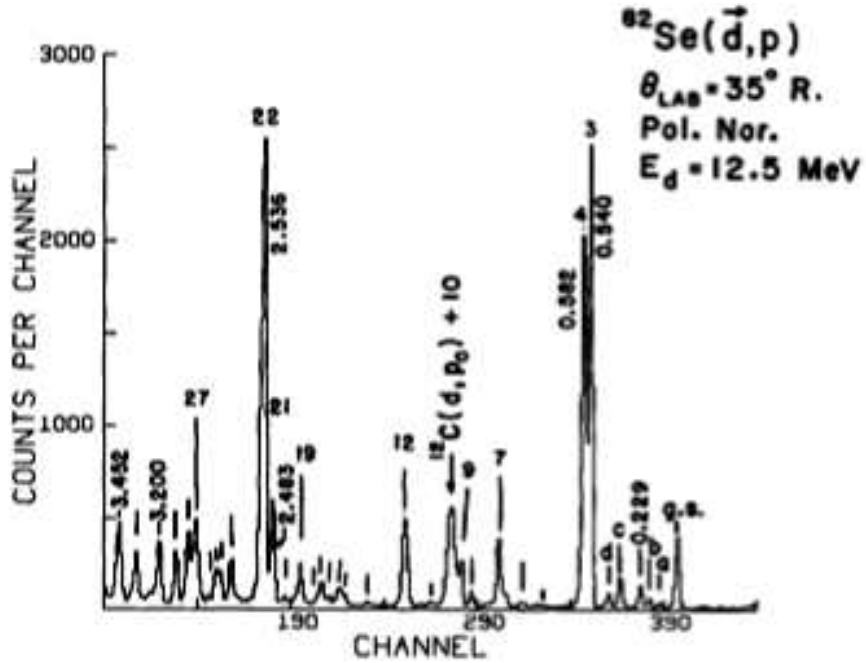

Figure 4.5: ^{82}Se(d,p)^{83}Se reaction Q-value spectrum as measured in normal kinematics at one angle. Figure taken from [Mon78]. Peaks labeled 3,4,7,12,and 22 correspond to states observed in the present measurement. The ^{12}C reaction contaminant would not be seen in the present measurement.

are not indications of deteriorating c.m. energy resolution; these groups each contain a number of closely spaced states that are not resolved. This energy resolution is consistent with expectations considering target thickness and angular resolution effects.

For comparison, Fig. 4.5 displays the Q-value spectrum measured in normal kinematics by Montestruque, *et al.*, at one angle with a magnetic spectrograph [Mon78]. The peaks labeled 3 and 4 comprise the doublet centered at $E_x = 560$ keV that was observed in the present measurement. Peak number 22 and nearby states correspond to the next strongest group as measured in the present experiment. Contaminant peaks are labeled by letters or the contaminating reaction. The peak labeled by the reaction ^{12}C(d,p$_0$) would not be seen in the present measurement.

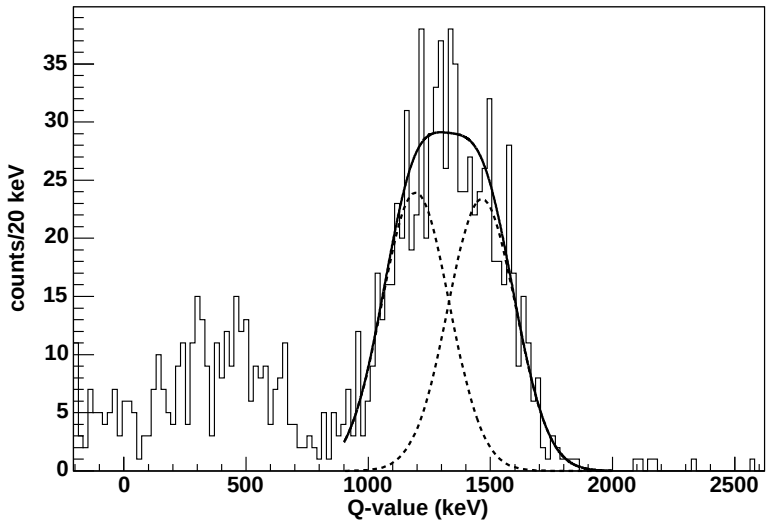

Figure 4.6: ^{2}H(^{82}Ge,p)^{83}Ge reaction Q-value spectrum summed over all angles. The dashed line is the two-peak fit of the ground and first-excited states (see text).

With the proton energies and angles calibrated, the Ge-coincident protons were projected onto a similar Q-value spectrum. Figure 4.6 is the ^{2}H(^{82}Ge,p)^{83}Ge reaction Q-value spectrum summed over all strips of SIDAR. The data in the figure show two groups, centered at $Q = 1.3$ MeV and $Q = 0.5$ MeV. The width of the first, strongest group is 1.5 times the empirical energy resolution of 300 keV, as determined from the internal Se calibration. The energy-level systematics of the even Z, $N = 51$ isotones, presented in Fig. 1.4, suggest the first-excited states of these nuclei are below ~ 1 MeV in energy. Based on the large width of the strong group, the large separation between the two resolved groups, and the locations of the first-excited states in similar $N = 51$ isotones (Fig. 1.4), the strong group is assumed to be the unresolved ground and first-excited states of ^{83}Ge. Figure 4.6 includes a fit to the strongest group assuming two peaks with widths equal to the 300-keV width of the lowest unresolved doublet in ^{83}Se.

The centroids of the fitted peaks yield a reaction Q-value of $Q = 1.47 \pm 0.02$ MeV and an excitation energy of $E_x = 280 \pm 20$ keV for the first-excited state. The quoted uncertainties are statistical. The systematic uncertainty of the Q-value determination is estimated from the biases introduced by the uncertainties of the quantities used to calibrate the measurement from kinematics. These include the uncertainties of the beam energy, the masses of ^{82}Se and ^{83}Se, the target thickness, and the excitation energy of the Se doublet line. A conservative estimate for this systematic uncertainty is 70 keV.

The Q-value of a reaction is defined as the difference of the mass energy in the initial reaction channel from the mass energy in the final channel [Kra87]. For a binary reaction:

$$Q = (m_{beam} + m_{target}) - (m_{eject} + m_{recoil}). \tag{4.1}$$

When three of the four masses are known along with the Q-value, Eq. 4.1 can be used to deduce the remaining mass. An atomic mass is usually quoted as a mass excess, a measure of the binding of the nucleus relative to the mass of an aggregate of its A nucleons [Kra87]:

$$\Delta(Z, A) = (m(Z, A) - A) \cdot c \tag{4.2}$$

Here, $m(Z, A)$ is in atomic mass units (amu) and $c \simeq 931.494$ MeV/amu is a conversion factor. By definition, the mass excess of ^{12}C, $\Delta(^{12}\text{C}) \equiv 0$ MeV. Since the total

number of nucleons is conserved in a (d,p) reaction, the Q-value can be written as

$$\begin{aligned} Q &= (\Delta(Z,A) + \Delta(d)) - (\Delta(p) + \Delta(Z,A+1)) \\ Q &= BE(Z,A+1) - (BE(d) + BE(Z,A)) \end{aligned} \tag{4.3}$$

where $BE(Z,A)$ is the binding energy of nucleus (Z,A). The neutron separation energy, $S_n(Z,A)$, defined as the energy needed to remove one neutron from nucleus (Z,A), is given as the difference in binding energies between this nucleus and the nucleus with the neutron removed:

$$S_n(Z,A+1) = BE(Z,A+1) - BE(Z,A). \tag{4.4}$$

From the second form of Eq. 4.3, it can be seen that by correcting the Q-value of a (d,p) reaction for the binding energy of the deuteron, the neutron separation energy of nucleus $(Z,A+1)$ is obtained.

The measured Q-value for the ^{2}H(^{82}Ge,p)^{83}Ge reaction corresponds to a mass excess of $\Delta(^{83}\text{Ge}) = -61.25 \pm 0.26$ MeV. The large uncertainty is almost entirely due to the uncertainty of the mass of ^{82}Ge (244 keV [Aud03]), an effect not seen with the Q-value determination because of a strong, negative covariance within the calculation of the Q-value involving this mass. The Q-value also leads to a neutron separation energy, $S_n(^{83}\text{Ge}) = 3.69 \pm 0.07$ MeV. The uncertainty is entirely from the Q-value as the deuteron binding energy is known to a much higher precision [Aud03]. The measured ^{83}Ge mass is compared to predictions from mass models in Sect. 5.2.

4.2 ^{2}H(^{84}Se,p)^{85}Se

The second measurement of this dissertation was performed in a way very similar to the first. The reaction kinematics are very similar, so the detectors were positioned to cover nearly the same laboratory ranges. Because of the large similarity in how the data were collected for the two experiments, this section describes how the measurement of the ^{2}H(^{84}Se,p)^{85}Se reaction differs from that of the ^{2}H(^{82}Ge,p)^{83}Ge measurement, as well as some immediate results.

An isobaric, $A = 84$ beam at $E_{beam} = 4.5$ MeV/nucleon bombarded a 200 μg/cm^2 CD_2 target for nearly 10 days. The choices of a higher beam energy and a thinner target were partly due to the resolution-limiting effects described in Sect. 4.1. The energy loss of the beam through the target "smears" the kinematics of the reaction, and is one of the main sources of systematic uncertainty in a Q-value determination. With a higher beam energy and a thinner target, the beam loses less energy as a fraction of its initial energy when passing through the target (2% for this measurement, compared to 5% for the ^{2}H(^{82}Ge,p)^{83}Ge measurement). The trade-off is that with a thinner target the (d,p) reaction counting rate is lower.

The SIDAR lampshade was positioned to subtend the same angles as for the previous measurement (see Sect. 4.1). Another silicon detector was placed upstream of the lampshade to cover the angular range of $\theta_{lab} = 160^\circ - 170^\circ$ ($\theta_{cm} \simeq 10^\circ - 5^\circ$). This detector, Micron Semiconductor's Design S1 [Mic05], is a flat, annular strip detector shaped like a compact disc (CD) with inner radius of 24 mm and outer radius of 48 mm. The sixteen annular strips are sectioned into quadrants (Fig. 4.7).

Figure 4.7: MSL Design S1 annular detector. Figure from Micron Semiconductor, Ltd. [Mic05].

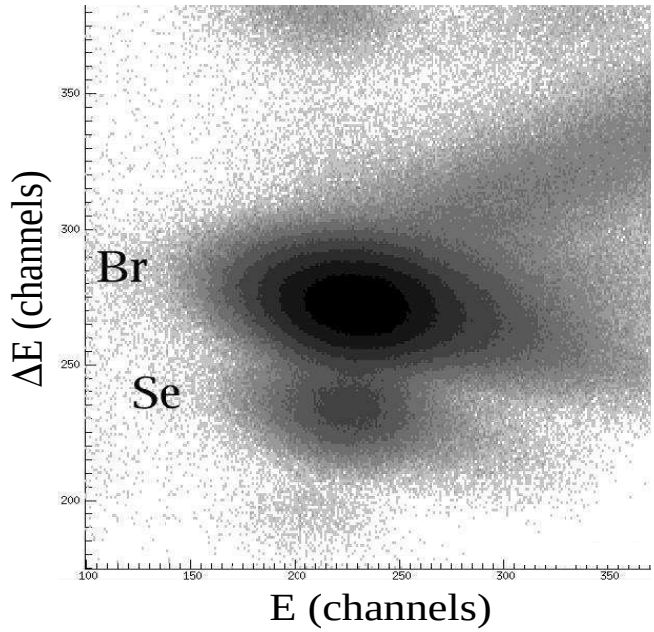

Figure 4.8: Energy loss ΔE vs. total energy E spectrum from the ionization chamber for the $A = 84$ beam.

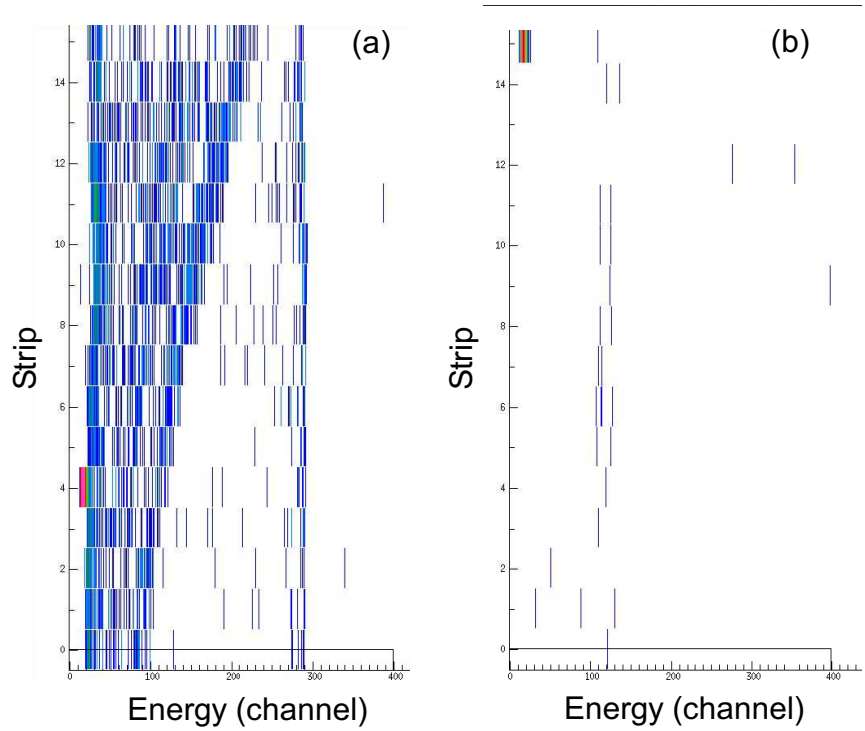

Figure 4.9: Detector strip number vs. proton energy in coincidence with Se from the $A = 84$ beam in the ionization chamber for the (a) SIDAR and (b) CD silicon detectors.

Figure 4.8 is the ionization chamber spectrum of energy loss, ΔE, versus energy deposited, E, for this measurement. The $\Delta Z = 1$ separation was necessary as the main beam contaminant was ^{84}Br (93%), separated from ^{84}Se by one proton. The radioactive ^{84}Se ($t_{1/2} = 3.1$ min [Bha05]) comprised only 7% of the total beam. The average beam rate over the entire experiment was 9×10^4 total pps. Spectra of strip number versus Se-coincident proton energy are shown in Fig. 4.9, for both (a) SIDAR and (b) the CD detector. The spectra were derived in the same way that coincident spectra were derived for the case of the $A = 82$ beam, with the necessary requirements of both the correct recoil species and a good TAC coincidence.

The calibration of the energy measured in the silicon detectors proceeded in the same way as with the Ge measurement. However, a key difference between this Se

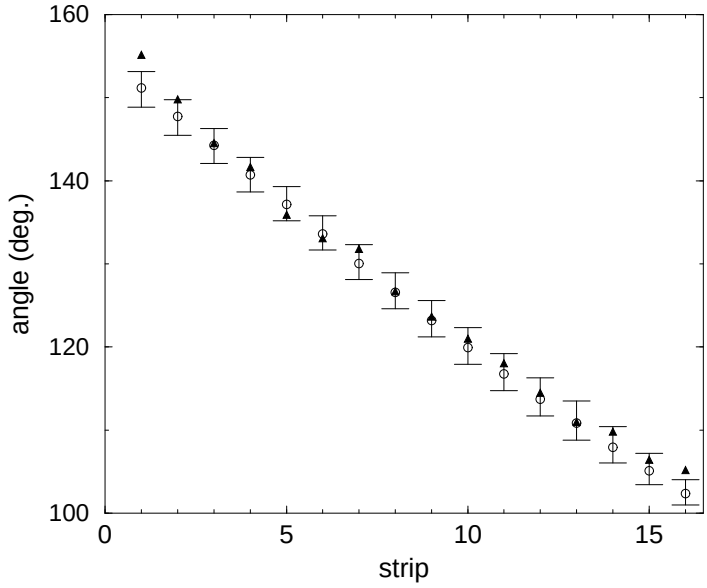

Figure 4.10: Strip angles for one wedge of SIDAR as calculated by a computer program (open circles) and determined from a few counts in a strip (filled triangles). The error bars give the calculated angular ranges for a strip.

measurement and the Ge measurement is that the excitation energies of the low-lying levels of ^{85}Se are known from a previous study of γ-ray transitions following the β decay of ^{85}As [Omt91], and the masses of all reacting particles are known (Q = 2.323 MeV [Aud03]). On a strip-by-strip basis it was possible to determine the counts that belong to a known state, although with very poor statistics (usually one or two counts). For data sorting purposes, the angle of the strip was determined such that these few counts were reconstructed with the proper Q-value. The same computer program that calculates geometric efficiences for the SIDAR (Sect. 3.2.2) calculates the average angle and the angular range subtended by each strip. As a check, the program output was compared to the angles as determined from the few counts registered in a strip. Figure 4.10 shows the comparison for one wedge of SIDAR. Because of the good agreement, the calculated angles were used in all

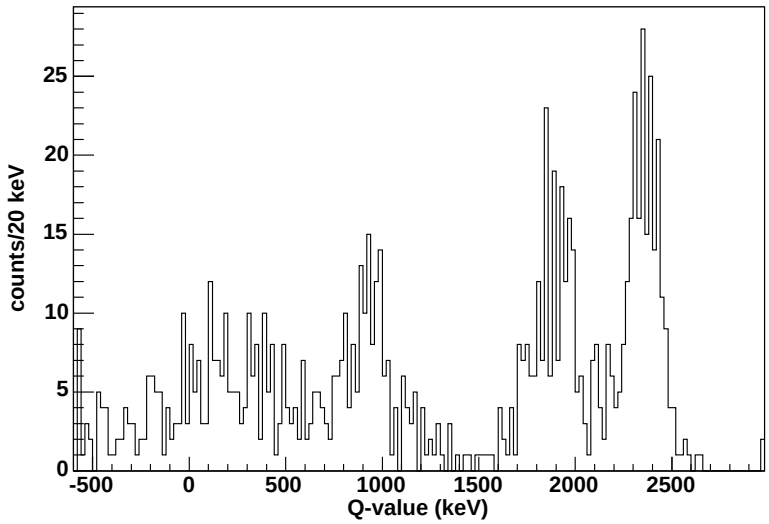

Figure 4.11: ^{2}H(^{84}Se,p)^{85}Se reaction Q-value spectrum summed over all angles. The ground-state Q-value of the reaction is $Q = 2.323$ MeV [Aud03].

subsequent analysis of proton angular distributions (Sect. 4.3.2).

A detailed analysis of the (d,p) reaction on the unstable ^{84}Br beam was not feasible. The ^{84}Br in the beam seemed to be a mixture of ^{84}Br in its ground state ($J^{\pi} = 2^{-}$, $t_{1/2} = 31.80$ min [Bha05]) and in its first-excited, isomeric state ($J^{\pi} = 6^{-}$, $t_{1/2} = 6.0$ min, $E_x = 320$ keV [Bha05]). As a test, the cyclotron bombardment of the UC target (Sect. 3.1) was stopped, but the beam was still delivered through the tandem to the ionization chamber. The intensity of the Br group as observed over time in the ionization chamber suggested two decay components in the beam with half-lives similar to those expected for both the ground and first-excited state of ^{84}Br. Because of the non-zero spin of both of these states, it is also not clear to which state in ^{85}Br the transfer occurs.

After both energy and angle calibrations, the proton data were projected onto a Q-value spectrum (Fig. 4.11). The ground and first-excited ($E_x = 462$ keV) states

are clearly separated, and the c.m. energy resolution is $\Delta E_{cm} \approx 220$ keV. There is also evidence of the second-excited state at $E_x = 1115$ keV ($Q = 1.21$ MeV), and a doublet of states centered at $E_x = 1441$ keV ($Q = 0.88$ MeV); the next strongest group in Fig. 4.11 after the first-excited state is likely two unresolved states with $E_x = 1438$ keV and $E_x = 1444$ keV [Omt91].

4.3 Proton angular distribution data

Absolute differential cross sections as a function of angle for the observed states were determined from the data through the relationship:

$$\frac{d\sigma(\theta_i)}{d\Omega} = \frac{N(\theta_i)}{I \cdot \Delta\Omega(\theta_i) \cdot n} \cdot \frac{\Delta\Omega_i^{lab}}{\Delta\Omega_i^{cm}} \tag{4.5}$$

where θ_i is the average angle of the ith angular bin; $N(\theta_i)$ is the number of recoil-coincident protons observed in the ith angular bin; I is the integrated beam current measured in the two-dimensional gate on the recoils in the ionization chamber (see Figs. 4.1, 4.8); $\Delta\Omega(\theta_i)$ is the solid angle subtended by the silicon detectors in the ith angular bin; n is the areal number density of target deuterons; and $\frac{\Delta\Omega_i^{lab}}{\Delta\Omega_i^{cm}}$ is the Jacobian of the transformation from laboratory to c.m. coordinates for the ith angular bin.

Because elastic scattering was not measured in the two reaction studies of this dissertation, global OM parameter sets had to be used. Lohr and Haeberli have determined a parameterization of the OM potentials for deuterons of $E_d = 8 - 13$ MeV (equivalent to $E_{beam} = 4 - 6.5$ MeV/nucleon in inverse kinematics) interacting with

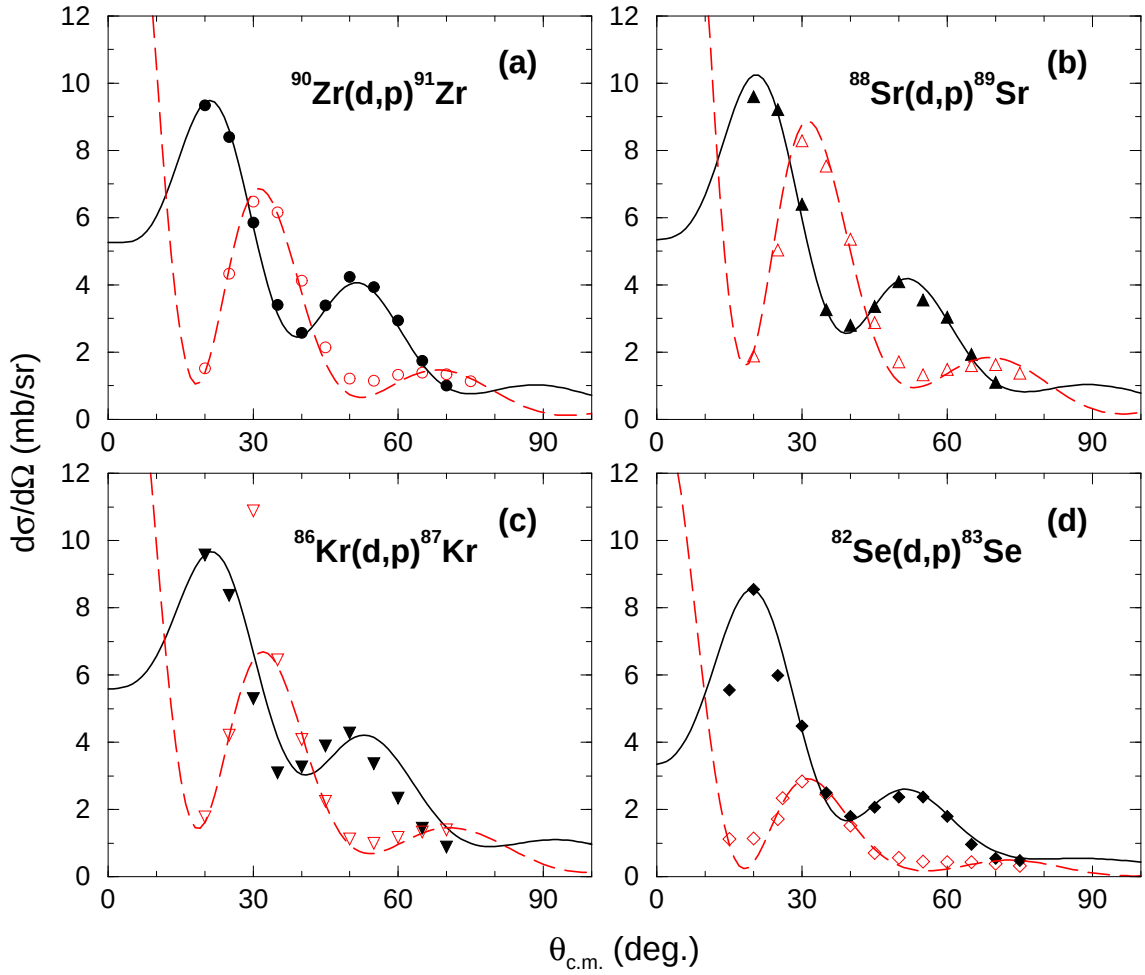

Figure 4.12: Proton angular distributions fit with global optical model parameters [Loh74] and [Var91]. Filled symbols (solid lines) are for $\ell = 2$ transfer to $5/2^+$ states; open symbols (dashed lines) are for $\ell = 0$ transfer to $1/2^+$ states. Data are for (a) ^{90}Zr(d,p)^{91}Zr [Rat73], (b) ^{88}Sr(d,p)^{89}Sr [Cle78], (c) ^{86}Kr(d,p)^{87}Kr [Har70], (d) ^{82}Se(d,p)^{83}Se [Mon78].

Table 4.1: Comparison of published spectroscopic factors, $S_{\ell j}$, and those derived from the present optical model analysis using global parameters. Published data are from: ^{90}Zr(d,p)^{91}Zr [Rat73]; ^{88}Sr(d,p)^{89}Sr [Cle78]; ^{86}Kr(d,p)^{87}Kr [Har70]; ^{82}Se(d,p)^{83}Se [Mon78].

^{A}Z	E_x (keV)	ℓ	J^π	$S_{\ell j}$ (published)	$S_{\ell j}$ (global OM)
^{91}Zr	0	2	$5/2^+$	1.09	1.02
	1201	0	$1/2^+$	0.88	0.82
^{89}Sr	0	2	$5/2^+$	1.03	0.89
	1031	0	$1/2^+$	1.06	0.93
^{87}Kr	0	2	$5/2^+$	0.56	0.76
	529	0	$1/2^+$	0.46	0.60
^{83}Se	540	0	$1/2^+$	0.28	0.27
	582	2	$5/2^+$	0.46	0.47

$A > 40$ nuclei [Loh74]. Varner, *et al.*, have established a parameterization for protons with $E_p > 10$ MeV interacting with $A > 40$ nuclei [Var91]. As a test of the applicability of these OM choices, data for (d,p) transfer onto nuclei near ^{82}Ge and ^{84}Se were re-analyzed with these potential parameterizations. Figure 4.12 shows a comparison of data from (d,p) reactions leading to even Z, $N = 51$ isotones [Figs. 4.12(a), 4.12(b), and 4.12(c)] and to ^{83}Se [Fig. 4.12(d)]. The curves in the figures are distorted waves calculations using the global OM parameters of [Loh74] and [Var91], and normalized to the data. The derived spectroscopic factors—the normalizations of the curves to the data in the figure, assuming the same bound-state geometries—are compared to the published values in Table 4.1. The shapes of the distributions in Fig. 4.12 qualitatively match the data, and the agreement of the re-analyzed spectroscopic factors to the published values is better than 14% for all cases with the exception of the ^{87}Kr data. However, the authors of another measurement of the ^{86}Kr(d,p)^{87}Kr reaction at a lower beam energy (data not shown) have extracted spectroscopic factors of

$S_{\ell j} = 0.66$ for the $\ell = 2$ ground state of ^{87}Kr and $S_{\ell j} = 0.67$ for the $\ell = 0$ first-excited state, both in considerably better agreement with the re-analyzed values [Sas65]. The differential cross section data from the Sass, *et al.*, work are reported as relative values (as opposed to absolute) [Sas65], so they were not included in the re-analysis. Because of the good agreement in most cases between the existing data and the distorted waves analysis with the chosen global OM potentials, these parameterizations were used in the subsequent analyses of the ^{2}H(^{82}Ge,p)^{83}Ge and ^{2}H(^{84}Se,p)^{85}Se reactions.

4.3.1 ^{2}H(^{82}Ge,p)^{83}Ge angular distributions

Ground and first-excited state proton angular distributions have been extracted from the ^{2}H(^{82}Ge,p)^{83}Ge reaction data (Sect. 4.1). The data were binned over larger angular ranges ($\Delta\theta_{lab} \simeq 12°$) than that subtended by a single strip to decrease the statistical uncertainty on a point of the distribution. However, because of the Jacobian of the transformation to the c.m. coordinates, this angular range corresponds to $\Delta\theta_{cm} \simeq 6°$. The distribution data were extracted from the binned Q-value spectra that together sum to the spectrum of Fig. 4.6. The proton counts of both states observed in each bin were determined from the areas of peak fits. The binned Q-value data from the ^{2}H(^{82}Se,p)^{83}Se reaction were used to fix the widths of the ^{83}Ge peaks for bin-by-bin fits, and the centroids of the peaks were fixed at the values already determined from the summed data.

The c.m. distributions extracted from the proton counts of the fits are shown in Fig. 4.13. The errors bars on the data are statistical. The solid curves are fitted

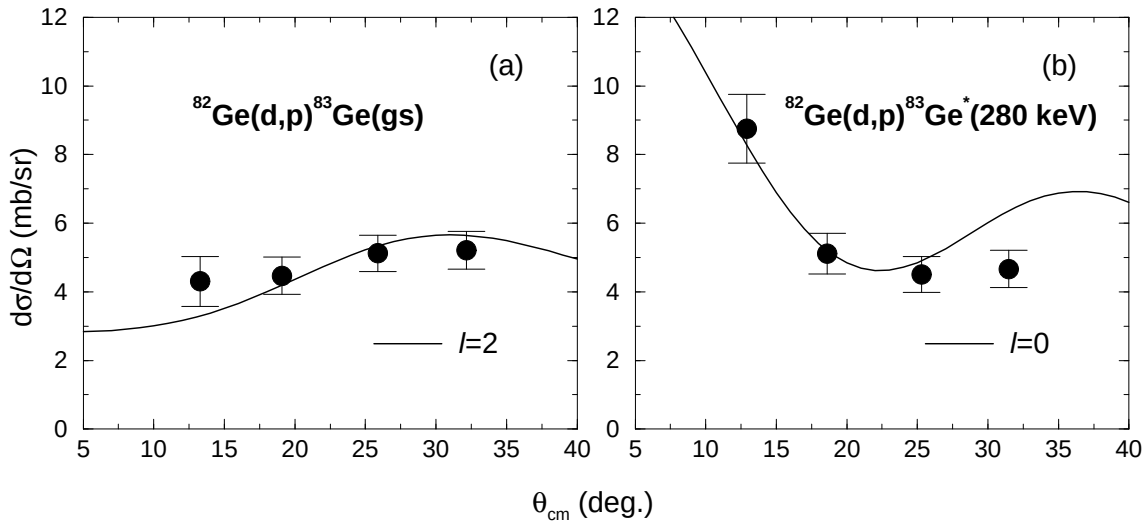

Figure 4.13: Proton angular distributions as functions of c.m. angle for ^{83}Ge. (a) Ground-state data are fit by an $\ell = 2$ DW calculation; (b) $E_x = 280$ keV data are fit by an $\ell = 0$ DW calculation.

distorted waves calculations for the reaction from the TWOFNR code [Iga] for $\ell = 2$ transfer to the ground state and $\ell = 0$ transfer to the first-excited state in ^{83}Ge. The geometry of the OM potentials as input into the TWOFNR code follow the conventions of [Per76] (see Sect. 2.3). The values of the potential parameters, derived from the global parameterizations of [Loh74, Var91], and including the assumed geometrical parameters of the neutron Woods-Saxon bound-state potential, are given in Table 4.2.

The empirical angular distributions are consistent with $\ell = 2$ transfer to the ground state and $\ell = 0$ transfer to the first-excited state. The $\ell = 2$ transfer to the ground state of ^{83}Ge supports a level assignment of $J^\pi = 3/2^+$ or $J^\pi = 5/2^+$, but the energy-level systematics of $N = 51$ isotones (Fig. 1.4) suggest a $J^\pi = 5/2^+$ assignment, which has been adopted. The $\ell = 0$ first-excited state can only be assigned $J^\pi = 1/2^+$. The DW calculations of Fig. 4.13 were made assuming the population

Table 4.2: Optical model potential parameters for the ^{2}H(^{82}Ge,p)^{83}Ge reaction. For the defintion of the parameters see Sect. 2.3. The value at * is adjusted to reproduce the binding energy of the neutron in ^{83}Ge.

	V (MeV)	r_0 (fm)	a_0 (fm)	W (MeV)	W_D (MeV)	r_W (fm)	a_W (fm)	V_{so} (MeV)	r_{so} (fm)	a_{so} (fm)	r_c (fm)
d	107.33	1.05	0.86	0.0	11.55	1.43	0.745	7.0	0.75	0.5	1.3
p (g.s.)	56.14	1.195	0.69	0.84	9.59	1.226	0.72	5.9	1.062	0.65	1.27
n	*	1.25	0.65	0.0	0.0	-	-	6.0	1.25	0.65	1.25

of the $2d_{5/2}$ neutron orbital for the ground state, and the $3s_{1/2}$ orbital for the first-excited state. Spectroscopic factors, as defined by Eq. 2.26, have been determined based on these assignments, with the values $S_{\ell j} = 0.48 \pm 0.12$ for the ground state and $S_{\ell j} = 0.50 \pm 0.13$ for the first-excited state. The 25% uncertainties on each factor are the combination in quadrature of the statistical best-fit uncertainty (6%), the estimated uncertainty in the determination of the target thickness (15%), and the systematic uncertainty (19%) due to the ambiguity of the geometrical parameters in the bound-state potential of the DW calculation. This last uncertainty was estimated by varying the bound-state potential radius parameter, r, between 1.2 to 1.3 fm and examining the effect on the extracted spectroscopic factors.

Without more information, the bound-state geometrical parameters in the DW calculation are essentially arbitrary. But as discussed in Sect. 2.4, if the measured reaction is peripheral, the ANC of the ^{83}Ge wavefunction can be extracted in a model-independent way. The computer code DWUCK4 [Kun] was used to apply a lower cutoff to the integration of the radial form-factors (overlap functions) used in the full DW calculation. Distorted waves calculations were performed for both ^{83}Ge states, varying the radial cutoff parameter, as displayed in Fig. 4.14. The magnitude of the

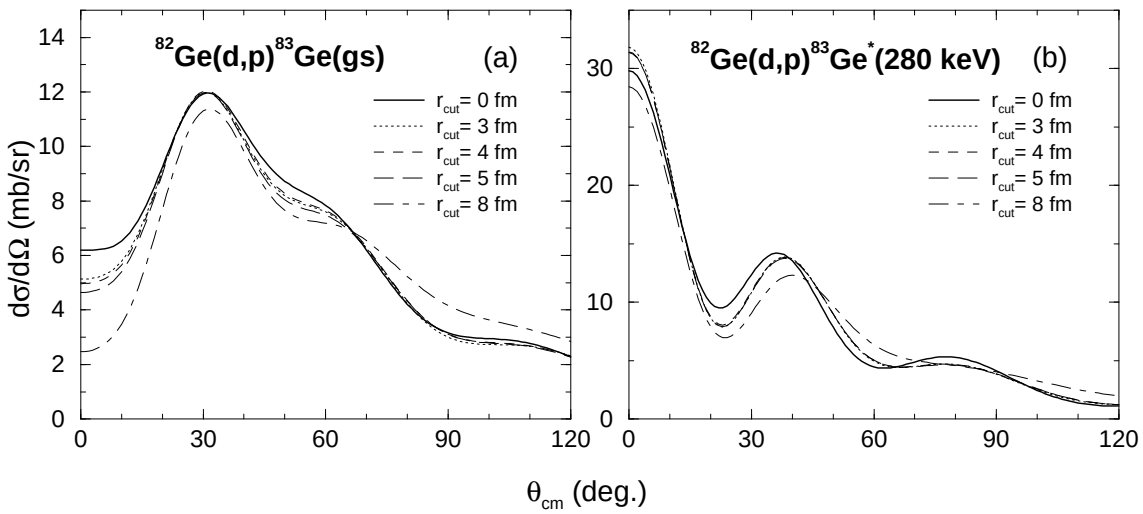

Figure 4.14: DW-calculated angular distributions with varying radial cutoffs in the overlap functions for ^{83}Ge. (a) Ground-state; (b) $E_x = 280$ keV state.

most prominent peak in each angular distribution varied by at most 10%, out to a cutoff radius of 8 fm. The relatively small change in peak magnitude demonstrates the relative insensitivity of the differential cross section to the nuclear interior parts of the overlap functions, a measure of a peripheral reaction.

Full DW calculations were made for both ^{83}Ge states, varying only the geometrical parameters for the bound-state potential. The DWUCK4 code was used to calculate the single-particle radial wavefunction for the neutron in the bound state (φ in Eq. 2.27). This wavefunction, for each variation of geometrical parameters, is matched at large radii to a corresponding spherical Hankel function (Eq. 2.30) to get the single-particle ANC, $b^B_{A\ell j}$. The corresponding spectroscopic factors, $S_{\ell j}$ were also determined for each parameter variation. Equation 2.31 was then used to extract C^2, the square of the ^{83}Ge ANC. The ANCs and spectroscopic factors for each of these analyses are plotted as functions of the single-particle ANCs b in Fig. 4.15. The scales of the vertical axes in each plot span the same percentage above and below a

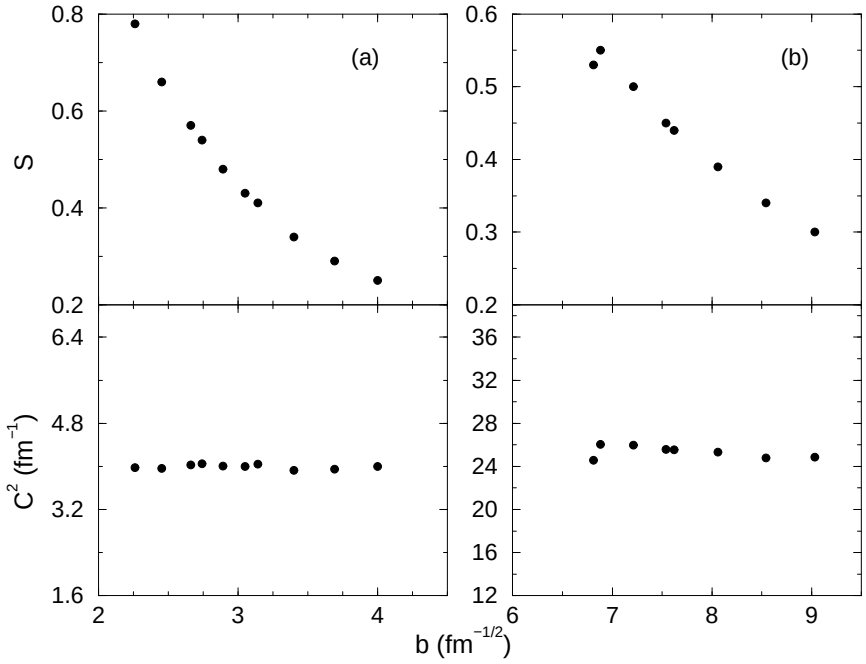

Figure 4.15: Dependencies of the extracted spectroscopic factors, S, and asymptotic normalization coefficients, C^2, on the single-particle ANCs, b, for ^{83}Ge. The single-particle ANCs are themselves functions of the bound-state potential geometry. (a) Ground-state; (b) $E_x = 280$ keV state.

central value to show the large dependency of the spectroscopic factor on the bound-state geometrical parameters, and the relative insensitivity of the ANC to these same parameters—another sign of a peripheral measurement.

The ANCs for each state were determined by averaging the extracted values related to each single-particle ANC. The uncertainties associated with each ANC are a quadrature combination of the sample deviation from the average, the best-fit uncertainty of the DW fit to the data, and the systematic uncertainty of the target normalization. The extra 19% contribution to the uncertainty of the quoted spectroscopic factor no longer applies as the ambiguity of potential parameters does not change the extracted ANC appreciably. The squared ANC for the ground-state transfer to ^{83}Ge is $C^2 = 3.99 \pm 0.67$ fm^{-1}. For the transfer to the first-excited state, the

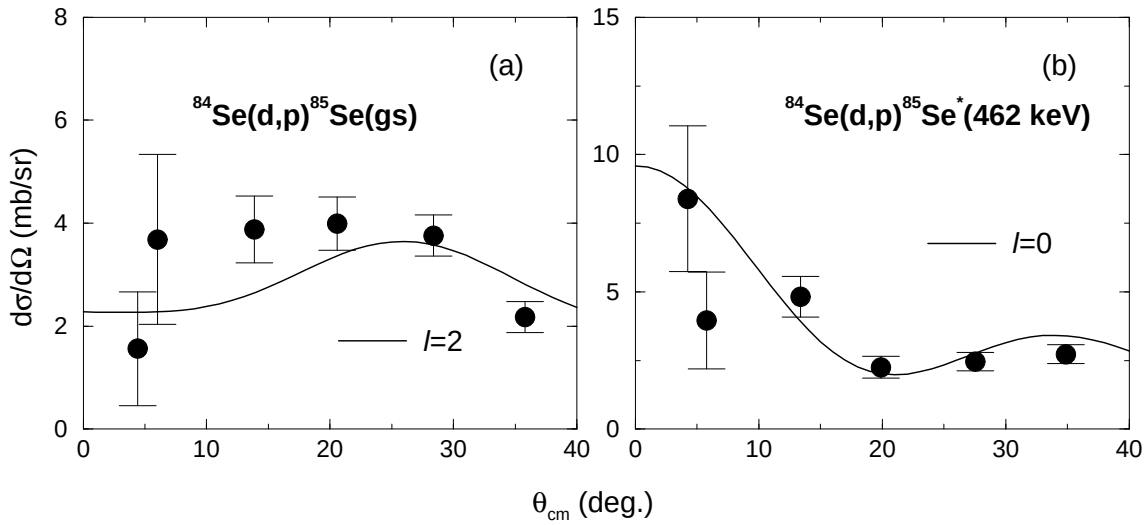

Figure 4.16: Proton angular distributions as functions of c.m. angle for ^{85}Se. (a) Ground-state data are fit by an $\ell = 2$ DW calculation; (b) $E_x = 462$ keV data are fit by an $\ell = 0$ DW calculation.

squared ANC is $C^2 = 25.2 \pm 4.1$ fm^{-1}.

4.3.2 ^{2}H(^{84}Se,p)^{85}Se angular distributions

Proton angular distributions from the ^{2}H(^{84}Se,p)^{85}Se reaction have been extracted from the data (Sect. 4.2) in a way similar to the ^{2}H(^{82}Ge,p)^{83}Ge reaction. The data from SIDAR (Sect. 3.2.2) were binned in four, four-strip bins, as with the Ge data, and the data from the CD detector (Sect. 4.2; Fig. 4.9) were binned into two bins of eight annular rings each.

The extracted angular distributions for transfer to the ground and first-excited states of ^{85}Se are presented in Fig. 4.16. The peaks in the Q-value spectrum for these two states are clearly resolved (Fig. 4.11), so the number of counts in each state, $N(\theta_i)$ of Eq. 4.5, is simply the sum of the peak counts in the bin. The error bars in Fig. 4.16 are purely statistical. Distorted waves calculations, shown as solid lines in

Table 4.3: Optical model potential parameters for the ^{2}H(^{84}Se,p)^{85}Se reaction. For the defintion of the parameters see Sect. 2.3. The value at * is adjusted to reproduce the binding energy of the neutron in ^{85}Se.

	V (MeV)	r_0 (fm)	a_0 (fm)	W (MeV)	W_D (MeV)	r_W (fm)	a_W (fm)	V_{so} (MeV)	r_{so} (fm)	a_{so} (fm)	r_c (fm)
d	108.21	1.05	0.86	0.0	11.37	1.43	0.749	7.0	0.75	0.5	1.3
p (g.s.)	55.31	1.195	0.69	0.92	9.14	1.227	0.72	5.9	1.065	0.65	1.27
n	*	1.25	0.65	0.0	0.0	-	-	6.0	1.25	0.65	1.25

Fig. 4.16, were made with the TWOFNR code using the globally parameterized potentials (Sect. 4.3) tuned for the ^{2}H(^{84}Se,p)^{85}Se reaction at $E_{beam} = 4.5$ MeV/nucleon, summarized in Table 4.3. Neutron configurations of $2d_{5/2}$ (ground state) and $3s_{1/2}$ (first-excited state) were assumed for the calculations.

The fits of the DW calculations to the data suggest transfers of $\ell = 2$ and $\ell = 0$ to the ground and first-excited states, respectively. Based on the same arguments as for the transfer to ^{83}Ge, the level assignments of $J^{\pi} = 5/2^{+}$ for the ground state of ^{85}Se and $J^{\pi} = 1/2^{+}$ for the first-excited state at $E_x = 462$ keV have been adopted. Spectroscopic factors have been extracted for these two states with the same estimated uncertainties as before: statistical best-fits, target thickness, and optical model parameters for the bound-state potential, leading to a 25% uncertainty. The extracted values are $S_{\ell j} = 0.33 \pm 0.08$ for the ground state and $S_{\ell j} = 0.30 \pm 0.08$ for the first-excited state. The bound-state potential parameters for these spectroscopic factors are summarized in Table 4.3.

As demonstrated in Fig. 4.17, the DW calculation is only slightly sensitive to the nuclear interior parts of the radial overlap functions, as was the case for the

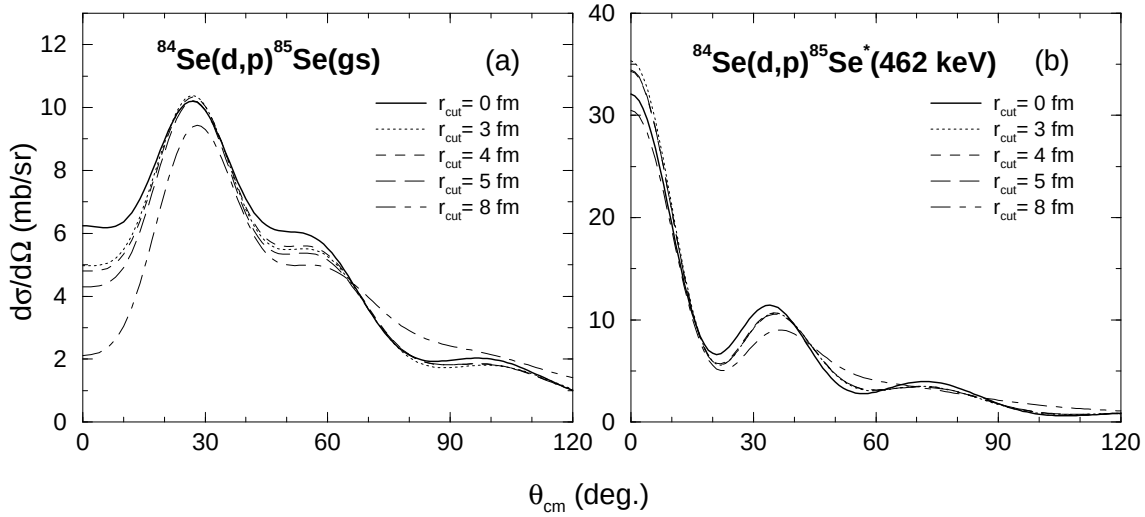

Figure 4.17: DW-calculated angular distributions with varying radial cutoffs in the overlap functions for ^{85}Se. (a) Ground-state; (b) $E_x = 462$ keV state.

^{2}H(^{82}Ge,p)^{83}Ge measurement, suggesting an ANC analysis is appropriate for this peripheral measurement of the ^{2}H(^{84}Se,p)^{85}Se reaction. The magnitude of the prominent forward peak varies by, at most, 10% out to a cutoff radius of 8 fm. The dependencies of the spectroscopic factors, S, and squared ANCs, C^2, on the single-particle ANCs, b, shown in Fig. 4.18, also suggest the reaction is peripheral; the extracted ANCs are nearly independent of the model-dependent nuclear interior part of the calculated overlap functions. The analysis and extraction of the ANCs for ^{85}Se proceeded in the same manner as for the ^{83}Ge case. The values $C^2 = 6.11 \pm 1.01$ fm^{-1} and $C^2 = 25.3 \pm 4.4$ fm^{-1} have been determined for the ground and first-excited states of ^{85}Se, respectively. Uncertainties come from the quadrature combination of the deviation from the average, the statistical best-fit of the DW calculations, and the uncertainty in the target thickness.

The data for the higher-lying excitations of ^{85}Se were also analyzed. However, the annular CD detector was not as useful for these states. The detection thresholds

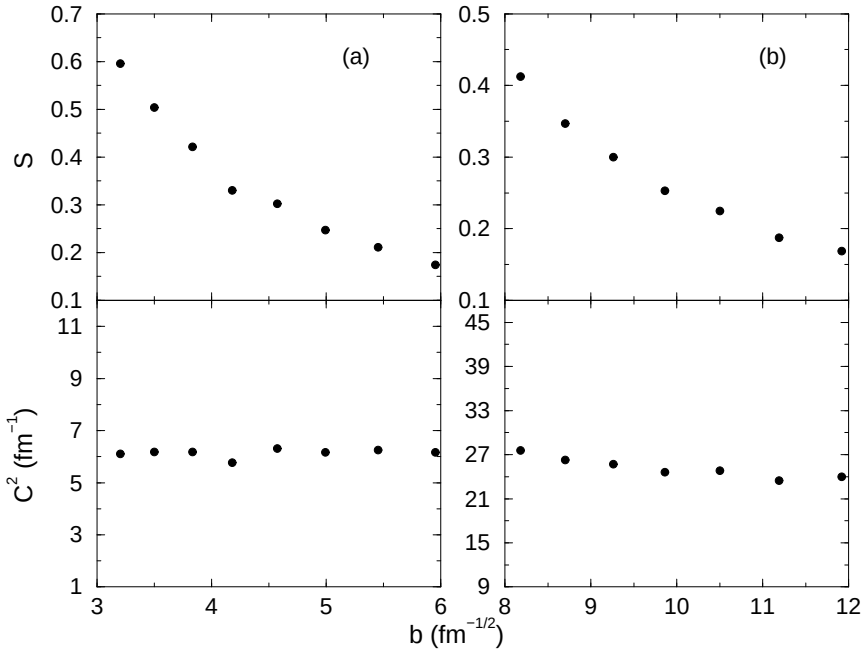

Figure 4.18: Dependencies of the extracted spectroscopic factors, S, and asymptotic normalization coefficients, C^2, on the single-particle ANCs, b, for ^{85}Se. The single-particle ANCs are themselves functions of the bound-state potential geometry. (a) Ground-state; (b) $E_x = 462$ keV state.

were probably set too high for this detector, eliminating lower-energy protons (higher-energy excitations) from the data stream. Still, SIDAR recorded counts for the state at $E_x = 1.115$ MeV and the doublet of states ($E_x = 1.438$ MeV and $E_x = 1.444$ MeV) centered at $E_x = 1.441$ MeV (see Fig. 4.11).

The previous work of Omtvedt, *et al.*, suggested the tentative assignment of $J^\pi = (3/2^+, 7/2^+)$ for the state at $E_x = 1.115$ MeV [Omt91]. The tentative assignment could indicate the population of either the neutron $2d_{3/2}$ ($\ell = 2$) or $1g_{7/2}$ ($\ell = 4$) configuration in ^{85}Se. The relative paucity of the data from the present work for this state ($Q = 1.208$ MeV in Fig. 4.11) suggests either very weak $2d_{3/2}$ strength for a $3/2^+$ state, or is a consequence of the poor angular momentum matching that

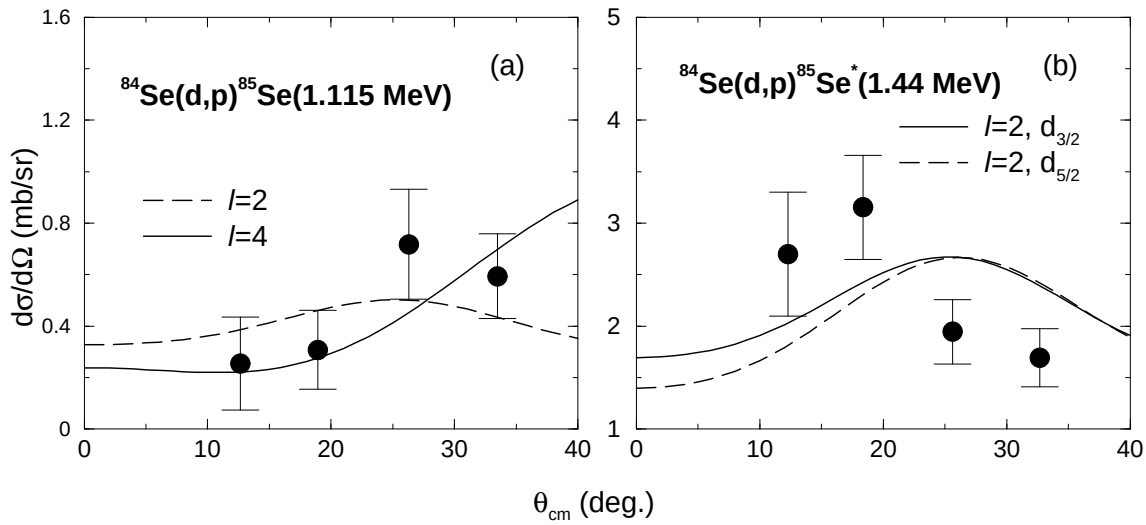

Figure 4.19: Proton angular distributions as functions of c.m. angle for ^{85}Se higher-lying excitations. (a) $E_x = 1.115$ MeV data are fit with $\ell = 2$ and $\ell = 4$ DW calculations; (b) doublet of $E_x = 1.438 + 1.444$ MeV data with $\ell = 2$ DW calculations as guides (see text).

inhibits $\ell = 4$ transfers (to the $1g_{7/2}$ configuration) in (d,p) reactions [Sat83]. The proton angular distribution from the population of this state is presented in Fig. 4.19(a). The DW calculations for $\ell = 2$ and $\ell = 4$ transfers are also shown. There appears to be a slight preference for the fit with the $\ell = 4$ calculation; however, the uncertainty of each fit is nearly 20%, and the reduced χ^2 values are abnormally low ($\chi^2/\nu = 0.89$ for $\ell = 2$, and $\chi^2/\nu = 0.51$ for $\ell = 4$). The spectroscopic factors determined from the fits are $S_{\ell j} = 0.06 \pm 0.02$ assuming a $2d_{3/2}$ configuration, and $S_{\ell j} = 0.77 \pm 0.27$ assuming a $1g_{7/2}$ configuration. The ANCs corresponding to the two possible assignments of this state are $C^2 = 0.42 \pm 0.11$ and $C^2 = 0.049 \pm 0.012$ for $\ell = 2$ and $\ell = 4$, respectively.

For completeness, the proton distribution from transfer to a doublet of states centered at $E_x = 1.441$ MeV ($E_x = 1.444$ MeV and $E_x = 1.438$ MeV) is shown in Fig. 4.19(b). The DW calculations in Fig. 4.19(b) are not fits to the data; rather,

Table 4.4: Summary of spectroscopic quantities determined from the measurements of the ^{82}Ge,^{84}Se(d,p) reactions in the present work. The ℓ are the transferred orbital angular momenta, J^π are the assigned (tentative) spins and parities, $S_{\ell j}$ are the extracted spectroscopic factors, C^2 are the squared ANCs, and $\Delta(^AX)$ is the mass excess of nucleus ^AX. Spectroscopic factors and ANCs for both ℓ-transfers are given for the 1.114 MeV excitation in ^{85}Se. The excitation energies of the states of ^{85}Se are taken from [Omt91].

^AX	E_x (MeV)	ℓ	J^π	$S_{\ell j}$	C^2 (fm^{-1})	$\Delta(^AX)$ (MeV)
^{83}Ge	0.0	2	$5/2^+$	0.48 ± 0.12	3.99 ± 0.67	-61.25 ± 0.26
	0.28 ± 0.07	0	$1/2^+$	0.50 ± 0.13	25.2 ± 4.1	-
^{85}Se	0.0	2	$5/2^+$	0.33 ± 0.08	6.11 ± 1.01	-
	0.462	0	$1/2^+$	0.30 ± 0.08	25.3 ± 4.4	-
	1.114	(2)	$(3/2^+)$	(0.06 ± 0.02)	(0.42 ± 0.11)	-
		(4)	$(7/2^+)$	(0.77 ± 0.27)	(0.049 ± 0.012)	-
	1.438 + 1.444	-	-	-	-	-

they are representative of $\ell = 2$ transfer. It was found that no simple, single ℓ transfer could explain the shape of this distribution. The shape of an $\ell = 0$ transfer would peak at $\theta_{cm} = 0°$ and again near $\theta_{cm} = 35°$; an $\ell = 1$ transfer would peak before the $\ell = 2$ transfer shown in Fig. 4.19(b), but would imply the population of a negative-parity state; and any transfer greater than $\ell = 2$ would not peak forward of $\theta_{cm} = 35°$.

To conclude this chapter, the spectroscopic information derived from the two measurements of this dissertation is summarized in Table 4.4. The excitation energies of states in ^{85}Se are taken from [Omt91].

Chapter 5

Interpretation

This chapter compares the results of Chapter 4 with previously measured properties of other $N = 51$ isotones and $Z = 51$ isotopes. Several mass models are described, and their predictions for the mass of ^{83}Ge are compared to the measured mass.

5.1 Energy level systematics

The spectroscopic properties of the first two states of the even $Z \leq 40$, $N = 51$ isotones, including the results of the measurements of the present work, are summarized in Fig. 5.1. The lengths of the thick lines at each energy level in the figure are proportional to the measured spectroscopic factors. The spectroscopic factors are all derived with the same bound-state potential parameters, $r_0 = 1.25$ fm and $a_0 = 0.65$ fm, for a Woods-Saxon shape.

The valence space above the presumed doubly-magic ^{78}Ni ($Z = 28$, $N = 50$) contains the $N = 51 - 82$ neutron orbitals $2d_{5/2}$, $2d_{3/2}$, $3s_{1/2}$, $1g_{7/2}$, and $1h_{11/2}$, and the $Z = 29 - 50$ proton orbitals $2p_{3/2}$, $2p_{1/2}$, $1f_{5/2}$, and $1g_{9/2}$. In an independent-particle shell model, the properties of the ground states and low-lying excitations of even Z, $N = 51$ isotones are expected to be determined solely by the valence neutron;

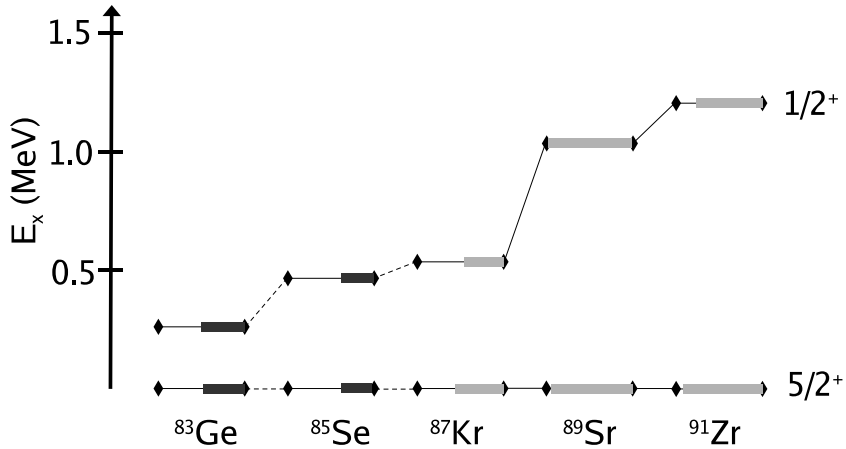

Figure 5.1: Spectroscopic properties of the first two states of the even $Z \leq 40$, $N = 51$ isotones. The lengths of the thick lines represent measured spectroscopic factors. Data for ^{83}Ge and ^{85}Se are from the present work. Data for the other $N = 51$ isotones: ^{91}Zr [Rat73], ^{89}Sr [Cle78], ^{87}Kr [Har70].

the protons are coupled to $J^\pi = 0^+$ and remain spectators in this picture.

The two states compared in Fig. 5.1 indicate the approximate validity of the independent-particle model. The ground states all have $J^\pi = 5/2^+$ and the first-excited states all have $J^\pi = 1/2^+$, in good agreement with the expectations of $\nu d_{5/2}$ and $\nu s_{1/2}$ configurations, respectively. However, the independent-particle model cannot explain the change in relative spacing between the two states, nor the reduced single-particle strengths seen in the more neutron-rich (lower Z) of these isotones.

The energies of single-particle states, the basis for the shell model, have long been known to depend on the configuration of the other nucleons. In particular, the location of a single-neutron level is strongly influenced by the orbitals occupied by the protons. The central potential of a $J^\pi = 0^+$ core nucleus is spherically symmetric, so the interaction with the valence orbit can have no directional (m-state) dependence [Cas00]. This directionally-independent interaction between filled shells and valence

nucleons is, therefore, due to the monopole part of the multipole expansion of the interaction, and is called the monopole shift [Cas00].

Each of the underlying filled shells of nucleons with angular momenta j can have a different effect on each valence orbital with angular momentum j' [Cas00]. As a result, the relative single-particle energies in a major shell can be dramatically different as nucleons of the opposite type fill specific j orbitals. The residual proton-neutron monopole interaction is written as [Ots01]:

$$V_{jj'} = \frac{\sum_J (2J+1) \langle jj' | V | jj' \rangle_J}{\sum_J (2J+1)} \tag{5.1}$$

where $\langle jj' | V | jj' \rangle_J$ is the matrix element of a two-body interaction. This residual interaction is found to be strongest between orbitals that are spin-orbit partners or pairs with opposite spins, and also those with good wavefunction overlaps [Gra03]. The directional independence of the interaction between a closed shell and a valence orbital means only the radial overlap is important in these cases. The radial overlap requirement implies that the strongest interactions are between orbitals with similar principal quantum numbers, n, and orbital angular momenta, ℓ [Fed77].

Figure 5.2 is an illustration of the relative proton single-particle energies for Sb ($Z = 51$) isotopes as a function of neutron number. The ground states of odd-A ^{105}Sb to ^{121}Sb all have $J^\pi = 5/2^+$ from a $\pi 2d_{5/2}$ configuration of the valence proton. Beginning near ^{113}Sb, the $J^\pi = 7/2^+$ state (likely the $\pi 1g_{7/2}$ configuration) drops in energy with increasing neutron number until finally becoming the ground state of ^{123}Sb and the heavier odd-A Sb isotopes. The relative separation between the $\pi g_{7/2}$

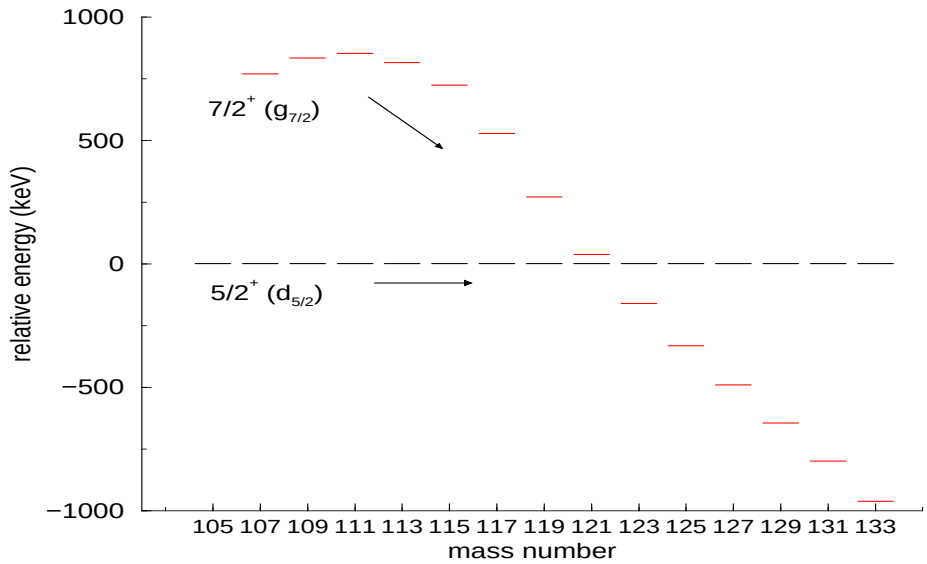

Figure 5.2: Relative energies of the first $5/2^+$ and $7/2^+$ states of odd-A Sb ($Z = 51$) isotopes, assumed to be the $\pi d_{5/2}$ and $\pi g_{7/2}$ single-particle states, respectively. Data taken from [Bha05].

and $\pi d_{5/2}$ orbitals also continues to grow with the addition of neutrons up to the closed shell at $N = 82$. The neutrons begin to fill the $\nu 1g_{7/2}$ orbital around $N = 62$ (^{113}Sb). The attractive proton-neutron interaction is stronger between protons in the $\pi 1g_{7/2}$ (rather than $\pi 2d_{5/2}$) orbital and $1g_{7/2}$ neutrons. Around $N = 72$ (^{123}Sb) the $\nu 1g_{7/2}$ orbital is full, but the neutrons begin filling the $\nu 1h_{11/2}$ orbital, a spin-flip partner to the $\pi 1g_{7/2}$ orbital with $\Delta\ell = 1$. The attraction between the $g_{7/2}$ protons and the increasing number of neutrons in the $1h_{11/2}$ orbital serve to further separate the $\pi g_{7/2}$ and $\pi d_{5/2}$ excitations in the low-lying spectra of the odd-A Sb isotopes.

This same mechanism is believed to cause the emergence of new magic numbers in neutron-rich nuclei. For example, the energies of the first 2^+ and 4^+ states in ^{56}Cr ($Z = 24$) suggest very little collectivity, usually a sign of a shell closure, in a nucleus in between both neutron and proton traditional closed shells [Pri01, App03]. The

explanation is that a new sub-shell closure occurs in this region for $N = 32$ because of the "release" of the $\nu f_{5/2}$ orbital [Pri01,App03]. In ^{49}Ca, with no protons in the $f_{7/2}$ orbital and one neutron beyond magic number $N = 28$ in the fp shell, the $\nu p_{3/2} - \nu p_{1/2}$ and $\nu p_{1/2} - \nu f_{5/2}$ energy gaps are significant, suggesting both $N = 32$ and $N = 34$ sub-shell closures in the region [App03]. With the addition of protons in the $f_{7/2}$ orbital, however, the strong $\pi f_{7/2} - \nu f_{5/2}$ interaction pulls the $\nu f_{5/2}$ orbital down, destroying first the $\nu p_{1/2} - \nu f_{5/2}$ gap, but preserving the separation between the $\nu p_{3/2} - \nu p_{1/2}$ orbitals, resulting in the $N = 32$ subshell closure in ^{56}Cr [Pri01, App03]. Further addition of protons soon destroys the remaining gap, as well, in the Ni isotopes.

The above discussion could suggest an explanation for the present case of the $N = 51$ isotones. In Fig. 5.1, the relative lowering of the $1/2^+$ state with decreasing proton number is equivalent to the lowering of the $5/2^+$ state with *increasing* proton number. If protons are removed from the $\pi f_{5/2}$ orbital beginning at Sr/Zr and continuing to Ge/Se, then a weakened $\pi f_{5/2} - \nu d_{5/2}$ interaction between this spin-flip $\Delta\ell = 1$ pair would "release" the $\nu d_{5/2}$ orbital, just as the removal of $f_{7/2}$ protons releases the $\nu f_{5/2}$ orbital in the $N = 32$ case. The $5/2^+$ ground state would then drift upward in going toward ^{83}Ge, relative to the barely affected $1/2^+$ state.

However, it is difficult to understand how the $\pi f_{5/2} - \nu d_{5/2}$ interaction is the explanation for the relative lowering of the $1/2^+$ state with decreasing Z in $N = 51$ isotones. The valence orbitals for $Z = 28 - 50$ protons (near $N = 50$) seem to be ordered differently than for $N = 28 - 50$ neutrons. In the the odd Z, $N = 50$ isotones, the ground states of ^{85}Br and ^{87}Rb both have $J^\pi = 3/2^-$ and ^{89}Y has $J^\pi = 1/2^-$.

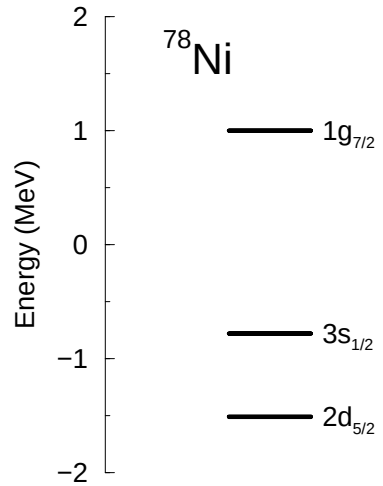

Figure 5.3: Neutron single-particle energies above the Fermi level in ^{78}Ni calculated from the Skyrme parameterization [Bro03].

Calculations of the odd-A Cu isotopes ($Z = 29$) suggest the ground state of ^{79}Cu has $J^\pi = 5/2^-$, an inversion of the $\pi 2p_{3/2}$ and $\pi 1f_{5/2}$ orbitals brought about by the strong $\pi f_{5/2} - \nu g_{9/2}$ interaction near $N = 50$ [Smi04]. The ground states suggest the ordering of proton levels above the closed shell of $Z = 28$ to be $f_{5/2}, p_{3/2}, p_{1/2}$. With this ordering, the $\pi f_{5/2} - \nu d_{5/2}$ interaction should not show increasing strength after the $\pi f_{5/2}$ orbital is already filled (near ^{84}Se).

Schematic arguments are not enough; detailed shell model calculations are necessary to describe the systematic features of Fig. 5.1. To this end, B. A. Brown has performed preliminary calculations for ^{83}Ge [Bro03]. The calculations use a combination of mean-field theory and configuration mixing. First, a Skyrme force parameterization is established for the mean field by fitting to known single-particle energies over a range of doubly- and singly-magic nuclei [Bro98]. Included in this fit are the single-particle energies for either ^{90}Zr or ^{88}Sr. The inclusion of both does not improve the fit. The single-particle energies for ^{78}Ni are extracted from the best-fit

Table 5.1: Comparison of the experimental and calculated [Bro03] properties of the first two states of ^{83}Ge.

J^π	E_x^{meas} (MeV)	E_x^{th} (MeV)	$S_{\ell j}^{meas}$	$S_{\ell j}^{th}$
$5/2^+$	0.0	0.0	0.48 ± 0.12	0.85
$1/2^+$	0.28 ± 0.07	0.47 ± 0.30	0.50 ± 0.13	0.51

Skyrme parameters, and a shell model calculation for ^{83}Ge is performed in the space of four protons and one neutron above the closed-shell ^{78}Ni. The proton input to the calculation is an effective interaction derived from $N = 50$ data [Ji88]. The neutron input are the ^{78}Ni single-particle energies from the Skyrme parameterization and a proton-neutron interaction from the M3Y potential [Kob84]. Figure 5.3 displays the neutron single-particle energies above the Fermi level in ^{78}Ni calculated from the Skyrme parameterization.

Table 5.1 compares the experimental and calculated spectroscopic properties of the first two states of ^{83}Ge. From the uncertainties assigned to the single-particle energies used in the Skyrme parameterization, the estimated uncertainty of the theory is 300 keV [Bro03]. Considering the calculations start from the single-particle energies of a predicted ^{78}Ni core, the agreement with the data for the first-excited state is fairly good. However, the theory predicts a significantly higher single-particle strength for the ground state than what is observed.

Not shown in the table are predictions for about 35 other states, up to an excitation energy of $E_x = 3$ MeV. The $s_{1/2}$ single-particle strength is fragmented across a number of these states, with the next state with significant $s_{1/2}$ strength at $E_x = 2.1$ MeV.

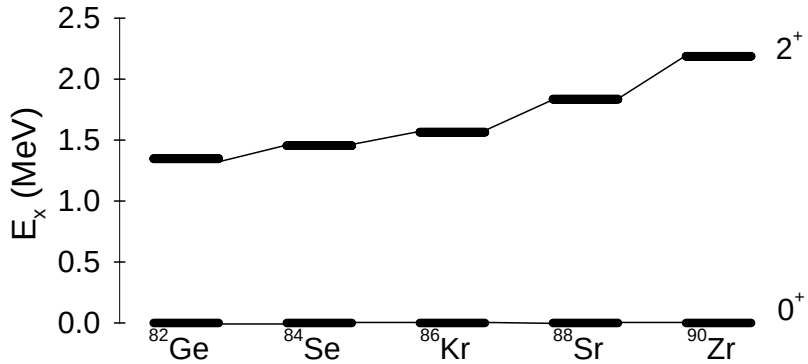

Figure 5.4: Excitation energies of the first 2^+ states in the even $Z \leq 40$, $N = 50$ isotones. Data taken from [Bha05, Pad05].

The fragmentation of the single-particle strength is not an entirely unexpected phenomenon as the states most single-particle-like in character are usually the low-lying excitations above *doubly*-magic nuclei. Since $Z = 40$ and, to some extent, $Z = 38$ are good subshell closures at $N = 50$, both ^{82}Ge and ^{84}Se are mid-shell in proton number. Figure 5.4 shows the energy of the first 2^+ states, $E(2_1^+)$, for the even Z, $N = 50$ isotones. In addition to single-particle excitations, a $1/2^+$ (and a $5/2^+$) state can be made in the $N = 51$ isotones by coupling a $d_{5/2}$ neutron to the 2^+ state of the even-even core. Such a $1/2^+$ excitation can mix with states with $s_{1/2}$ strength, reducing the $s_{1/2}$ strength of the first-excited state in the process. This coupling is expected more readily when the 2^+ state is lower in excitation, a situation usually found in the middle of a major shell. Although lower in excitation than in the $Z = 38$ and 40 isotones, the first 2^+ states in ^{82}Ge and ^{84}Se are relatively high in energy, at $E_x \sim 1.4$ MeV, considerably higher than the first $1/2^+$ states in the $N = 51$ nuclei. More calculations are needed, especially to compare with the other $N = 51$ isotones, to determine if such a mechanism can fragment the single-particle strength of both the $5/2^+$ and $1/2^+$ states of ^{83}Ge and ^{85}Se.

5.2 Masses far from stability

One of the most fundamental properties of an atomic nucleus is its mass. The binding energies of nuclei are part of the direct evidence for nuclear shell structure. A "kink" in (two-nucleon) separation energies across a specific number of nucleons indicates the presence of a significant shell gap. It is expected that changes in the shell structure of exotic nuclei will be reflected in the masses.

Masses are important in an astrophysical context, as well. As discussed in Chap. 1, the rapid neutron capture (r-) process is typically considered as a steady-state, near-equilibrium process. In the traditional description of the r-process, the cross sections for neutron capture are not important during the neutron irradiation time; the bath of neutrons and photons ensures an equilibrium between the (n,γ)-(γ,n) reactions [Fre99]. The build-up of isotopic abundances depends on the temperature, irradiation time, neutron concentration, and, notably, the neutron separation energies [Fre99]. The built-up abundance pattern in the very neutron-rich species determines, to an extent, the abundance pattern that is observed after these nuclei decay back towards stability. Most of the nuclei that participate in the neutron capture phase of the r-process have never been observed. The masses used in r-process calculations are predicted from various mass models that incorporate systematics, phenomenology, and basic nuclear structure physics. It will be many years before even a fraction of the masses involved are measured, but new mass measurements always update the present knowledge and may indicate new physics that must be included in the models for more reliable predictions far from stability. As documented in Fig. 1.3, solar

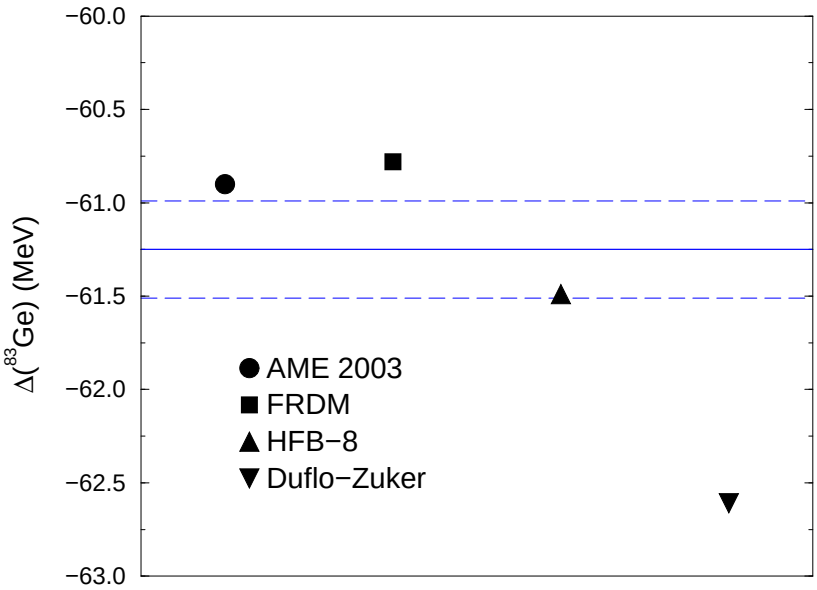

Figure 5.5: The mass excess, Δ, of ^{83}Ge as measured (horizontal line with dashed-line error bars), and predicted from the Atomic Mass Evaluation (AME) 2003 [Aud03], the Finite Range Droplet Model (FRDM) [Möl95], the Hartree-Fock-Bogoliubov-8 (HFB-8) model [Sam04], and the Duflo-Zuker model [Duf95].

abundances attributed to the r-process show patterns that are better explained by calculations that include a mass model with a quenched shell structure [Che95,Fre99].

The measurement of the Q-value of the ^{2}H(^{82}Ge,p)^{83}Ge reaction is also an indirect measurement of the previously unknown mass of ^{83}Ge (see Sect. 4.1). Figure 5.5 compares the measured mass excess, Δ(^{83}Ge), with the predictions of four models. The four models are briefly described below.

The Atomic Mass Evaluation (AME), a collection of the measured masses, makes short extrapolations to unstable nuclei [Aud03]. The extrapolations are based on keeping "smooth" the mass surface, a plot of the known masses as a function of Z and N [Aud03]. In this way, the masses just on the edges of the mass surface are typically predicted fairly well because small, local changes can be accounted for, but the reliability of the predictions farther from known values suffers. The AME is not

meant to be predictive.

The Finite-Range Droplet Model (FRDM) of Möller, *et. al*, is based on a macroscopic-microscopic approach to calculating atomic masses [Möl95]. The starting point is a liquid drop model, similar to the Bethe-Weizsäcker mass formula, that accounts for phenomenology, such as the observed saturation properties of nucleon interactions and the symmetry energy from the imbalance of protons and neutrons in the nucleus [Rin80]. Added to this macroscopic model are microscopic shell-plus-pairing corrections and corrections for deformation energy [Möl95]. The parameters in the model are derived from a fit to the known masses, and calculations with the best-fit parameters yield the masses of nuclei out to the model's predicted drip-lines of particle stability.

Goriely argues that for r-process applications, mass extrapolations should be based on more realistic microscopic models than the FRDM [Gor03]. The highly parameterized methods (such as the FRDM of Möller, *et. al*) do well, and even better than full microscopic models, in accurately reproducing experimental masses, but the better accuracy in the phenomenological methods is attributed to the computational complexity of the parameter determination from fits to data in the microscopic models [Gor03]. With advances in computation, however, it is now possible to generate mass tables that are based on supposedly more reliable nuclear structure physics. One such model, HFB-8, is based on Hartree-Fock-Bogoliubov mean-field theory with Skyrme forces, including pairing, fit to experimental mass data [Sam04].

The fourth mass model, of Duflo and Zuker [Duf95], is also a microscopic model

that incorporates microscopic phenomenology. A shell model Hamiltonian is separated into a monopole part and a part that contains all other multipoles of the shell model space [Duf95]. The multipole part is an effective interaction derived from a realistic nucleon-nucleon interaction. The monopole part of the effective Hamiltonian treats explicitly the description of single-particle behavior; the energies (masses) of closed-shell and subshell nuclei are controlled in the calculation by the monopole part of the Hamiltonian [Duf95].

As shown in Fig. 5.5, the AME and HFB-8 predictions reproduce the measured value of the mass excess of ^{83}Ge within uncertainties. The FRDM predicts a mass excess somewhat higher than the data. In contrast, the Duflo-Zuker model prediction of the mass excess is significantly lower than the measured value. In other regions of the nuclear landscape, the Duflo-Zuker model does very well in predicting masses near and across closed shells.

Figure 5.6 (adapted from [AMD05]) shows the differences, as functions of neutron number, between experimental masses and the Duflo-Zuker predictions of isotopic chains from $Z = 28 - 40$, offset by Z MeV (i.e., if the theory reproduces the measured mass, the plotted difference is Z of the isotope in MeV). The comparison with the mass of ^{83}Ge measured in the present work is indicated by the circled point. The $Z = 36$ chain is an example of what to expect if the Duflo-Zuker model is good. Aside from the expected even-odd differences, the predicted differences show relatively small deviations from Z, even across the $N = 50$ closure. However for $Z < 36$, the masses are systematically under predicted (corresponding to the over prediction of binding

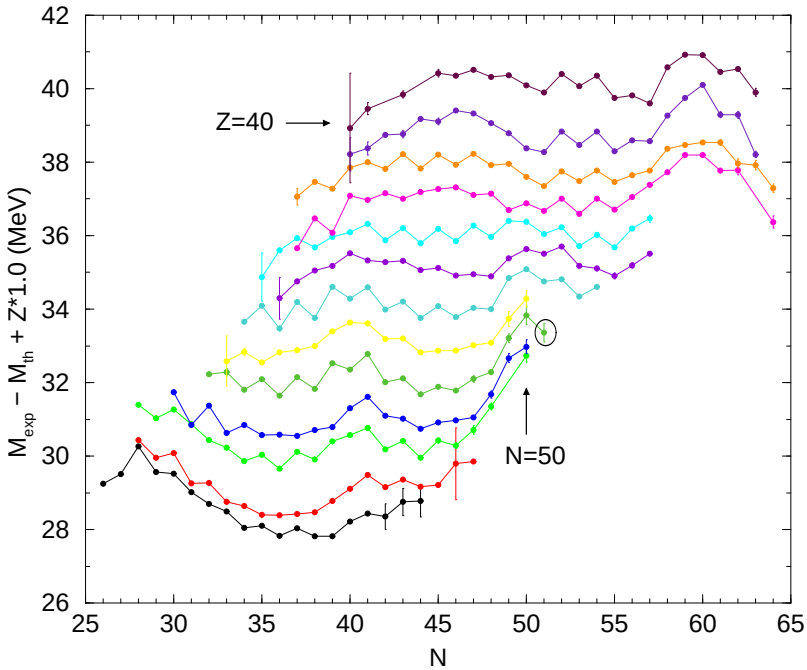

Figure 5.6: Differences between experimentally measured masses [Aud03] and predictions from the Duflo-Zuker mass model [Duf95,AMD05], offset by Z MeV, for isotopic chains with $Z = 28 - 40$. The circled point is the value for ^{83}Ge.

energies) for $N < 50$. The Duflo-Zuker model is designed to incorporate the effects of shell and subshell closures. The systematic over prediction of binding energies suggest that the actual shell gap at $N = 50$ near $Z = 28$ could be smaller than Duflo and Zuker predict. That the value for ^{83}Ge in Fig. 5.6 is less than for the $N = 50$ isotope ^{82}Ge supports this suggestion of a weaker $N = 50$ gap near ^{78}Ni [Aud05], a suggestion somewhat corroborated by the shorter than expected ^{78}Ni half-life of 110 ms [Hos05]. Alternatively, the model is poorly tuned to this region.

Figure 5.7 is a plot similar to Fig. 5.6 of mass differences for $Z = 48 - 64$ isotopes across the $N = 82$ shell gap. Here, the predictions of the Duflo-Zuker model are very accurate and, with the exception of a slight rise in the mass difference for $Z = 48$ and 49, there are no corresponding peaks around $N = 82$ [Aud05].

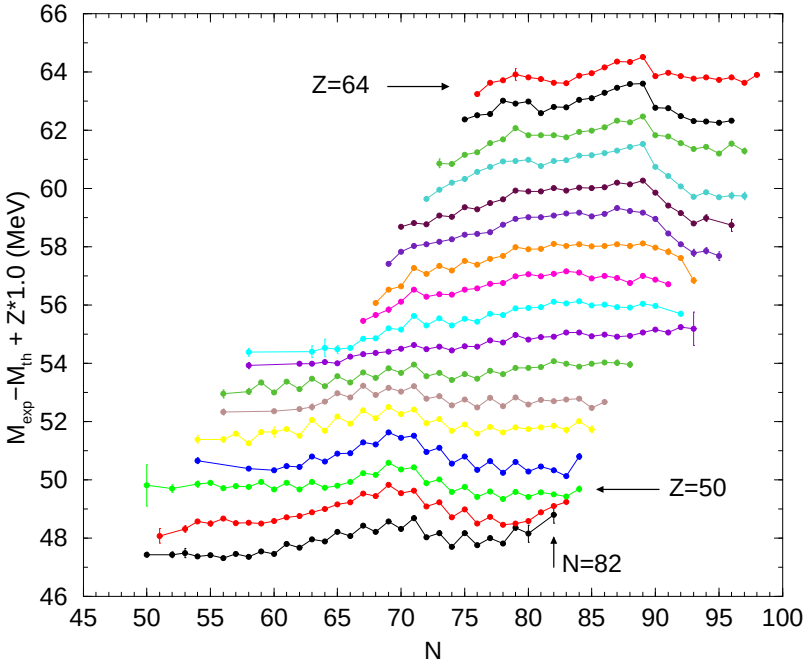

Figure 5.7: Differences between experimentally measured masses [Aud03] and predictions from the Duflo-Zuker mass model [Duf95,AMD05], offset by Z MeV, for isotopic chains of $Z = 48 - 64$.

Chapter 6

Summary and Conclusion

Radioactive ion beams of ^{82}Ge and ^{84}Se were used to measure the ^{2}H(^{82}Ge,p)^{83}Ge and ^{2}H(^{84}Se,p)^{85}Se reactions for the first time. The single-neutron excitations of the final $N = 51$ nuclei were populated and studied through the use of charged-particle spectroscopy in inverse kinematics. The (d,p) reaction proceeds in a direct manner allowing for the identification of excitation energies, transferred angular momenta, and single-particle strengths of final states by studying the energies and angular distributions of the emitted protons. Recoil coincidences in an ionization chamber enhanced the proton spectra and provided an absolute normalization for the differential cross sections extracted from the data.

The study of the low-lying states of ^{83}Ge revealed their excitation energies, spins, and parities. From proton differential cross sections and systematics of $N = 51$ isotones, the ground and first-excited ($E_x = 0.28 \pm 0.07$ MeV) states are found to have $J^\pi = 5/2^+$ and $J^\pi = 1/2^+$, respectively. The Q-value measured for the ^{2}H(^{82}Ge,p)^{83}Ge reaction ($Q = 1.47 \pm 0.07$ MeV) yielded the previously unknown mass of ^{83}Ge ($\Delta = -61.25 \pm 0.26$ MeV). This result, when compared to the particular mass model of Duflo and Zuker [Duf95], and taken with the lower-than-expected half-life of

^{78}Ni [Hos05], suggests shell effects for neutron-rich nuclei near $N = 50$ may be over-estimated. The spectroscopic factors of the first two states account for about half of the expected $2d_{5/2}$ and $3s_{1/2}$ neutron single-particle strengths, a result not entirely unexpected considering the semi-magic, mid-proton-shell nature of ^{82}Ge. However, with the relatively high excitation energy of the first 2^+ state of ^{82}Ge it is not clear that configuration mixing with $\nu \oplus 2^+$ excitations can lead to such fragmentation of the single-particle strength, and more theoretical investigation is warranted.

The measurement of ^{85}Se confirmed the energies of the first three states and the average excitation energy of a doublet consisting of the third and fourth excited states as determined in a previous study of γ-ray transitions following the β decay of ^{85}As [Omt91]. The spins and parities of the first two states, determined in a way similar to those of ^{83}Ge, confirm the tentative assignments of Omtvedt, *et al.* [Omt91], of $J^\pi = 5/2^+$ for the ground state and $J^\pi = 1/2^+$ for the first-excited state. Definitive level assignments cannot be made for the other states populated in the present measurement. The extracted spectroscopic factors for the first two states are both about one-third of the respective single-particle limits for pure $d_{5/2}$ and $s_{1/2}$ orbitals. It is not clear why the fragmentation of these single-particle strengths appears greater for ^{85}Se compared to ^{83}Ge. If the second-excited state has $J^\pi = 3/2^+$, the spectroscopic factor indicates a very weak ($\approx 7\%$) $d_{3/2}$ neutron configuration. Alternatively, the spectroscopic factor for a $J^\pi = 7/2^+$ assignment to this state is near the single-particle limit ($\approx 90\%$) for a $g_{7/2}$ neutron configuration.

The spectroscopic properties of the low-lying states in ^{83}Ge and ^{85}Se can inform

the rate of direct neutron capture on these nuclei. In the astrophysical scenario of the r-process, the ^{82}Ge(n,γ)^{83}Ge reaction rate may modify the final abundances observed in the $A \sim 80$ mass peak. The situation for capture to ^{83}Ge is similar to that of neutron capture on doubly-magic ^{208}Pb [Bla02, Rau98]. The Q-value of the ^{208}Pb(n,γ)^{209}Pb reaction is $Q = 3.938$ MeV, and there are very few resonances at this threshold energy [Bla02]. It is found that the direct component of the neutron capture cross section to ^{209}Pb is a significant fraction of the total capture cross section. The direct component of the Maxwellian-averaged cross section at 100 keV, a temperature ($\approx 1 \times 10^9$ K) expected in r-process events, is over 50% of the total [Bee97]. The Q-value for the ^{82}Ge(n,γ)^{83}Ge reaction, $Q_{\mathrm{n},\gamma} = 3.69$ MeV, equivalent to the neutron separation energy of ^{83}Ge (Sect. 4.1), is smaller than for the (n,γ) reaction on any stable nucleus heavier than ^{15}N. Because of the proximity of ^{83}Ge to a closed neutron shell, and particularly because of the low neutron separation energy of ^{83}Ge, the direct capture rate is expected to be a significant component to the total (n,γ) capture rate. The spins and positive parities of the first two states of ^{83}Ge and ^{85}Se mean that even at low energies the dominant direct capture terms will be p-wave ($\ell = 1$) capture accompanied by $E1$ γ-ray decay.

6.1 Outlook

6.1.1 Prospects for further $N = 51$ studies

There is an ongoing effort to determine the nuclear structure of the neutron-rich nuclei above the doubly magic ^{78}Ni. In regards to the present work on the $N = 51$

isotones, the ultimate goal would be to complete the measurements of single-neutron properties along the neutron-rich part of the $N = 51$ isotonic chain. This realization would require transfer reaction measurements to ^{81}Zn and ^{79}Ni, two very unfamiliar nuclei. The half life of ^{81}Zn ($t_{1/2} = 290 \pm 50$ ms [Kra91a]) is the only measured property of that $N = 51$ nucleus, and ^{79}Ni has never been observed in the laboratory. The major difficulty in these measurements will be the production of beams of very short-lived nuclei. The half life of ^{80}Zn is $t_{1/2} = 537 \pm 29$ ms [Kra91a]. It was only recently that the half life of ^{78}Ni ($t_{1/2} = 110^{+100}_{-60}$ ms [Hos05])—the necessary beam for (d,p) reactions to ^{79}Ni—was determined.

To perform these measurements will require advanced facilities capable of producing these exotic nuclei in more sufficient quantities than what are available today. In the United States, the Rare Isotope Accelerator (RIA) [RIA05] is being planned, and in Europe the Facility for Antiproton and Ion Research (FAIR) [FAI05] is being developed. However, there are still open experimental questions that can be explored while the next generation radioactive ion beam facilities are being built.

Because of ambiguities in the bound-state potentials used in the analyses described in Sect. 2.4, and the fact that the present measurements are peripheral reactions, there are uncertainties regarding the appropriateness of the present extraction of spectroscopic factors. Therefore, the related, nearly-model-independent quantities of the asymptotic normalization coefficients (ANCs) for the bound-state wavefunctions have been determined. The fact that the ANCs can be used reliably across different measurements suggests a two-stage process to determine more accurate spectroscopic

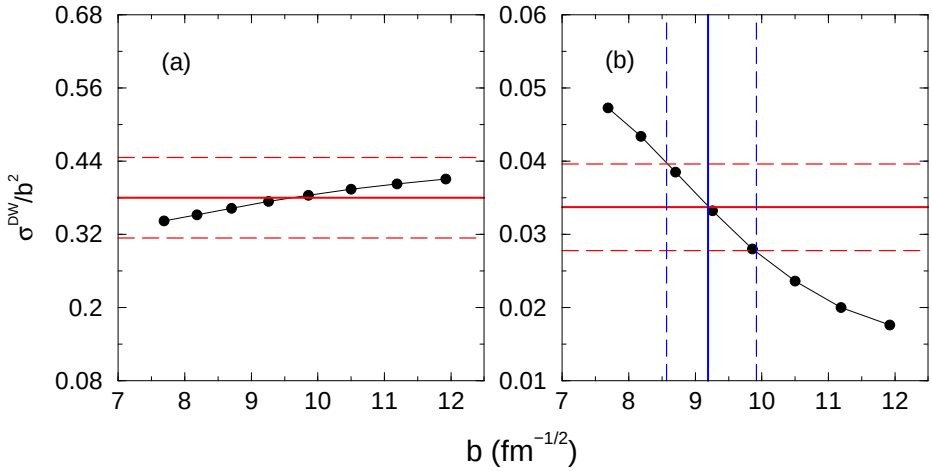

Figure 6.1: Calculated dependency of the ratio $\sigma^{DW}/\left(b^B_{A\ell j}\right)^2$ as a function of the single-particle ANC, $b^B_{A\ell j}$ (points). (a) peripheral reaction; horizontal line is a "measured" ratio $(d\sigma/d\Omega)/(C^B_{A\ell j})^2$. (b) non-peripheral reaction; the measured ratio (horizontal lines) constrains the single-particle ANC (vertical lines) leading to a more accurate spectroscopic factor.

factors [Muk05].

At higher incident beam energies, where the transfer reaction cannot be considered peripheral, the removal of model dependencies by "factoring out" the single-particle ANCs, b, from the calculated differential cross sections, as demonstrated in Eq. 2.32, is no longer complete. Figure 6.1 shows the factored quantity $\sigma^{DW}/\left(b^B_{A\ell j}\right)^2$ as a function of the single-particle ANC, $b^B_{A\ell j}$, for both (a) a peripheral measurement and (b) a non-peripheral measurement. Examining Eq. 2.32 again, the division of both sides by $(C^B_{A\ell j})^2$ yields an equivalence between the factored quantity plotted in Fig. 6.1 and an experimentally determined quantity, $(d\sigma/d\Omega)/(C^B_{A\ell j})^2$. This second quantity (in this case an illustration, not actual data) is plotted in Fig. 6.1 as the horizontal line with associated error bars. The two-stage process for the spectroscopic factor determination is as follows: a peripheral measurement is performed to determine the ANC, $(C^B_{A\ell j})^2$; a second, non-peripheral measurement determines $d\sigma/d\Omega$ at the

higher beam energy; finally, the ratio $(d\sigma/d\Omega)/(C^B_{A\ell j})^2$, determined from *independent* measurements, is used to constrain the ratio $\sigma^{DW}/\left(b^B_{A\ell j}\right)^2$, thereby fixing the single-particle ANC, $b^B_{A\ell j}$, and the spectroscopic factor through the relationship of Eq. 2.31 [Muk05].

6.1.2 Prospects for further (d,p) studies at HRIBF

The work presented here is part of a broad, ongoing research program at the HRIBF to study transfer reactions on unstable nuclei. Future radioactive beam (d,p) reaction measurements are planned on both light and heavy neutron-rich fission fragments. The lighter fission fragments can be measured using the same techniques of this dissertation. However, an alternate approach must be used for the heavier fragments because, at the currently available beam energies, the reaction products have different angular distributions in the laboratory.

The HRIBF is able to deliver beams of heavy fission fragments such as ^{132}Sn at energies just above the Coulomb barrier. Measurements near the $N = 82$ closed shell for the Sn ($Z = 50$) isotones are important to probe shell structure in nuclei far from stability, as well as to probe the properties of nuclei along the r-process path of nucleosynthesis. Figure 6.2 shows a DW calculated differential cross section for the ^{132}Sn(d,p)^{133}Sn reaction at a beam energy of 4 MeV/nucleon, in both c.m. and laboratory coordinates. When compared with Fig. 2.1, the comparatively lower energy relative to the barrier in Sn destroys the diffraction-like shape of the proton angular distributions of the (d,p) reaction as observed at higher energies [Sat83]. The

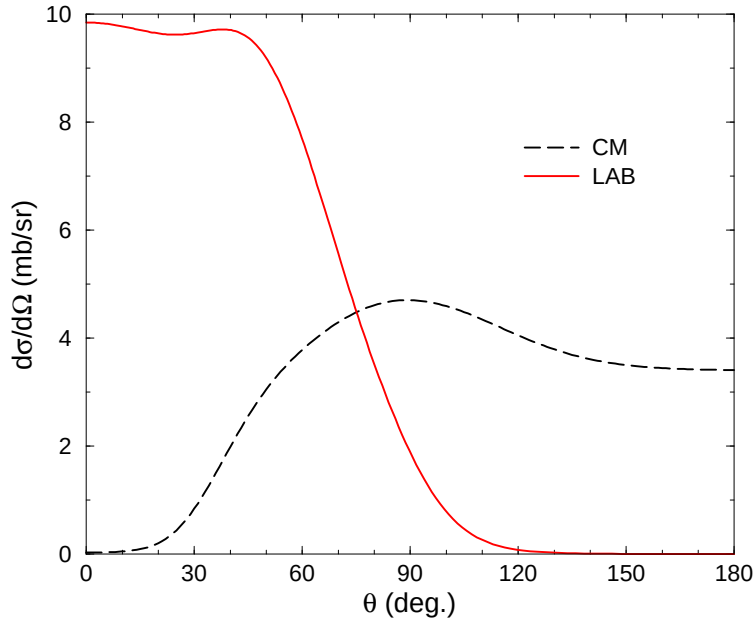

Figure 6.2: Calculated angular distributions for the ^{132}Sn(d,p)^{133}Sn reaction with $\ell = 3$ transfer at $E_{beam} = 4$ MeV/nucleon, referred to c.m. (dashed) and laboratory (solid) coordinates.

laboratory distribution in Fig. 6.2 demonstrates that measurements of the protons in this reaction must be forward of $\theta_{lab} \approx 100°$ in order to be sensitive to the shape of the distribution and to perform the measurement in a finite time with reasonable cross sections.

Proton detection near $\theta_{lab} = 90°$ presents a number of experimental complications. From the inverse reaction kinematics, the proton energies increase with decreasing laboratory angle, and the rate of change of the energy with respect to angle is largest for angles near $\theta_{lab} \approx 90°$. The higher energy protons require thicker detectors to stop and record the deposited energy. The large rate of change, or kinematic shift, means that protons with very similar trajectories differ considerably in energy; thus the resolution in energy of these protons is worsened. The c.m. resolution of excitation energies can be improved with very good position resolution of the detected protons:

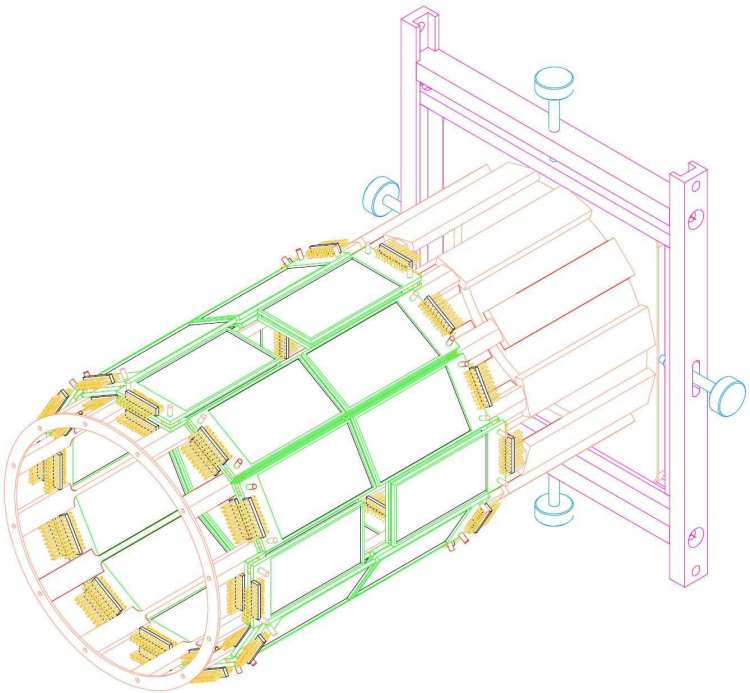

Figure 6.3: The Oak Ridge Rutgers University Barrel Array showing the two rings of charged-particle telescopes. The gap between rings allows for a target to be mounted.

the detected angles and energies of the protons are both needed to reconstruct the Q-value of the reaction. Detection of protons forward of $\theta = 90°$ requires particle identification techniques because for elastic scattering, $\theta_{lab} = 90°$ corresponds to $\theta_{cm} = 0°$, where Rutherford scattering is concentrated. Therefore, the protons from transfer must be detected in a large background of elastically scattered deuterons and carbons from a CD_2 target (as well as elastically scattered protons from any CH_2 in the target).

To meet these detection demands, the Oak Ridge Rutgers University Barrel Array (ORRUBA) is being constructed. The design for this large array of silicon detectors, shown in Fig. 6.3, consists of two rings of 12 particle telescopes that function analogously to the anodes of the ionization chamber described in Sect. 3.2.1: particle

identification is determined by $\Delta E - E$ measurement in the two silicon detectors of each telescope. The silicon detectors consist of wafers that have longitudinally aligned strips with resistive front layers. The ΔE detectors will have two thicknesses, 65 and 140 μm; the E detectors will be 1 mm thick. The resistive layer on each strip creates a division of the charge from incident radiation that is read out from both ends of the strip. The differences in the signals from the two strip ends provide measurements of the longitudinal position. The position resolution in this direction—the direction most sensitive to the polar angle of the reaction—is typically better than 1 mm, and depending on the distance of the ring from the beam axis, can lead to an angle resolution on the order of $\Delta\theta = 0.5°$. The ORRUBA design is complete. The prototype detectors are currently being tested. Commisioning of ORRUBA is anticipated for early 2006. Initial measurements of the ^{130,132}Sn(d,p) reactions are scheduled for Fall 2005 using 6-9 $\Delta E - E$ silicon detector telescopes.

Another option being developed for the measurement of (d,p) transfer reactions is to measure reaction protons in coincidence with gamma rays. The resolution of a high-purity germanium detector is typically on the order of a fraction of a percent ($\sim$ 2 keV at 1.33 MeV) [Kno00]. In present (d,p) measurements with beams travelling at $\sim$ 0.1 c, there are considerable Doppler effects. The Doppler broadening at $\theta_{lab} = 90°$ is anticipated to degrade the γ-ray energy resolution to $20 - 30$ keV, still significantly better than for reaction proton energies. Therefore, by measuring γ rays in coincidence with reaction protons the excitation energies of the states can be determined more accurately, and closely-spaced doublets can be resolved. When

high energy levels are populated, the subsequent cascade of transitions would also allow indentification of additional excitations with little low-ℓ single-particle strengths. One of the drawbacks to measuring γ rays in coincidence with reaction protons, especially with low-intensity radioactive beams, is the limited efficiency of the germanium detectors. Even with close-packed geometries, the efficiency for γ-ray detection will be about 4%. The effect of this limitation is hopefully minimized by the efficiency of the charged-particle detectors. In Summer 2005 the (d,pγ) capabilities will be developed by measuring the transfer onto the stable, $N = 50$ ^{88}Sr. Once developed, the ^{82}Ge(d,pγ) reaction could be remeasured to obtain a more accurate measurement of the energy of the $1/2^+$ state, resolving this excitation from the ground state. In the longer term, the (d,pγ) measurements could incorporate ORRUBA at the center of an array of Ge detectors.

References

[AMD05] http://www.nndc.bnl.gov/amdc/index.html

[App03] D. E. Appelbe, C. J. Barton, M. H. Muikku, J. Simpson, D. D. Warner, C. W. Beausang, M. A. Caprio, J. R. Cooper, J. R. Novak, N. V. Zamfir, R. A. E. Austin, J. A. Cameron, C. Malcolmson, J. C. Waddington, and F. R. Xu, Phys. Rev. C **67**, 034309 (2003).

[Aud03] G. Audi, A. H. Wapstra and C. Thibault, Nucl. Phys. **A729**, 337 (2003).

[Aud05] G. Audi, private communication (2005).

[Bar00] D. W. Bardayan, Ph. D. thesis, Yale University (2000).

[Bar01] D. W. Bardayan, J. C. Blackmon, W. Bradfield-Smith, C. R. Brune, A. E. Champagne, T. Davinson, B. A. Johnson, R. L. Kozub, C. S. Lee, R. Lewis, P. D. Parker, A. C. Shotter, M. S. Smith, D. W. Visser, and P. J. Woods, Phys. Rev. C **63**, 065802 (2001).

[Bar39] W. H. Barkas, Phys. Rev. **55**, 691 (1939).

[Bar73] C. M. Bartle and H. O. Meyer, Nucl. Instrum. Meth. **112**, 615 (1973).

[Bec69] F. D. Bechetti, Jr. and G. W. Greenlees, Phys. Rev. **182**, 1190 (1969).

[Bee96] H. Beer, C. Coceva, P. V. Sedyshev, Yu. P. Popov, H. Herndl, R. Hofinger, P. Mohr, and H. Oberhummer, Phys. Rev. C **54**, 2014 (1996).

[Bee97] H. Beer, F. Corvi, and P. Mutti, Astrophys. J. **474**, 843 (1997).

[Ber00] M. J. Berger, J. S. Coursey, and M. A. Zucker, *ESTAR, PSTAR, and ASTAR: Computer Programs for Calculating Stopping-Power and Range Tables for Electrons, Protons, and Helium Ions (version 1.2.2)*, (2000) Available: http://physics.nist.gov/Star [2005, January 11], National Institute of Standards and Technology, Gaithersburg, MD.

[Bha05] M. Bhat, *Evaluated Nuclear Structure Data File* (Springer-Verlag, Berlin, 1992), data extracted using the NNDC ON-Line Data Service from the ENSDF database, file revised as of February 13, 2005.

[Bia99] S. F. Biagi, Nucl. Instrum. Meth. **A421**, 234 (1999).

[Bla02] J. C. Blackmon, S. Raman, J. K. Dickens, R. M. Lindstrom, R. L. Paul, J. E. Lynn, Phys. Rev. C **65**, 045801 (2002).

[Bro98] B. A. Brown, Phys. Rev. C **58**, 220 (1998).

[Bro03] B. A. Brown, private communication.

[Byr70] F. W. Byron, Jr. and R. W. Fuller *Mathematics of Classical and Quantum Physics* (Dover Publications, New York, 1970).

[Car97] H. K. Carter, J. Kormicki, D. W. Stracener, J. B. Breitenbach, J. C. Blackmon, M. S. Smith, and D. W. Bardayan, Nucl. Instrum. Meth. **B126**, 166 (1997).

[Cas00] R. F. Casten, *Nuclear Structure from a Simple Perspective*, (Oxford University Press, New York, 2000).

[Che95] B. Chen, J. Dobaczewski, K. L. Kratz, K. Langanke, B. Pfeiffer, F. K. Thielemann, and P. Vogel, Phys. Lett. B **355**, 37 (1995).

[Chr66] L. G. Christophorou, G. S. Hurst, and A. Hadjiantoniou, J. Chem. Phys. **44**, 3506 (1966).

[Chr79] L. G. Christophorou, D. L. McCorkle, D. V. Maxey, and J. G. Carter, Nucl. Instrum. Meth. **163**, 141 (1979).

[Cla83] D. D. Clayton, *Principles of Stellar Evolution and Nucleosynthesis*, (University of Chicago Press, Chicago, 1983).

[Cle78] T. P. Cleary, Nucl. Phys. **A301**, 317 (1978).

[Dav00] T. Davinson, W. Bradfield-Smith, S. Cherubini, A. DiPietro, W. Galster, A. M. Laird, P. Leleux, A. Ninane, A. N. Ostrowski, A. C. Shotter, J. Vervier, and P. J. Woods, Nucl. Instrum. Meth. **A454**, 350 (2000).

[Dob96] J. Dobaczewski, W. Nazarewicz, T. R. Werner, J. F. Berger, C. R. Chinn, J. Decharge, Phys. Rev. C **53**, 2809 (1996).

[Duf95] J. Duflo and J. P. Zuker, Phys. Rev. C **52**, 23 (1995).

[FAI05] http://www.gsi.de/zukunftsprojekt/index_e.html

[Fed77] P. Federman and S. Pittel, Phys. Lett. B **69**, 385 (1977).

[Fee49] E. Feenberg, and K. C. Hammack, Phys. Rev. **74**, 1877 (1949).

[For74] J. L. C. Ford Jr., K. S. Toth, G. R. Satchler, D. C. Hensley, L. W. Owen, R. M. DeVries, R. M. Gaedke, P. J. Riley, and S. T. Thornton, Phys. Rev. C **10**, 1429 (1974).

[Fre99] C. Freiburghaus, J.-F. Rembges, T. Rauscher, E. Kolbe, F.-K. Thielemann, K.-L. Kratz, B. Pfeiffer, and J. J. Cowan, Astrophys. J. **516**, 381 (1999).

[Gor03] S. Goriely, Nucl. Phys. **A718**, 287c (2003).

[Gra03] H. Grawe, Acta Phys. Pol. B **34**, 2267 (2003).

[Har70] K. Haravu, C. L. Hollas, P. J. Riley, and W. R. Coker, Phys. Rev. C **1**, 938 (1970).

[Hau52] W. Hauser and H. Feshbach, Phys. Rev. **87**, 366 (1952).

[Hax49] O. Haxel, T. H. D. Jensen, and H. E. Suess, Phys. Rev. **75**, 1766 (1949).

[HRI05] http://www.phy.ornl.gov/hribf/ribinjector

[Hos05] P. T. Hosmer, H. Schatz, A. Aprahamian, O. Arndt, R. R. C. Clement, A. Estrade, K.-L. Kratz, S. N. Liddick, P. F. Mantica, W. F. Mueller, F. Montes, A. C. Morton, M. Ouellette, E. Pellegrini, B. Pfeiffer, P. Reeder, P. Santi, M. Steiner, A. Stolz, B. E. Tomlin, W. B. Walters, and A. Wöhr, Phys. Rev. Lett. **94**, 112501 (2005).

[Hun88] S. R. Hunter, J. G. Carter, and L. G. Christophorou, Phys. Rev. A **38**, 58 (1988).

[Iga] University of Surrey modified version of the code TWOFNR of M. Igarashi, M. Toyama, and N. Kishida, private communication.

[Jam88] A. N. James, T. P. Morrison, K. L. Ying, K. A. Connell, H. G. Price, and J. Simpson, Nucl. Instrum. Meth. **A267**, 144 (1988).

[Ji88] X. Ji, B. H. Wildenthal, Phys. Rev. C **37**, 1256 (1998).

[Kno00] G. F. Knoll, *Radiation Detection and Measurement*, 3rd ed., (Wiley, New York, 2000).

[Kob84] A. M. Kobos, B. A. Brown, R. Lindsay, and G. R. Satchler, Nucl. Phys. **A425**, 205 (1984).

[Kör71] H. J. Körner and J. P. Schiffer, Phys. Rev. Lett. **27**, 1457 (1971).

[Kra87] K. S. Krane, *Introductory Nuclear Physics* (Wiley, New York, 1987).

[Kra91a] K.-L. Kratz, H. Gabelmann, P. Möller, B. Pfeiffer, H. L. Ravn, A. Wöhr, and the ISOLDE Collaboration, Z. Phys. A **340**, 419 (1991).

[Kra91b] G. Kraus, P. Egelhof, H. Emling, E. Grosse, W. Henning, R. Holzmann, H. J. Körner, J. V. Kratz, R. Kulessa, Ch. Schieβl, J. P. Schiffer, W. Wagner, W. Walus, and H. J. Wollersheim, Z. Phys. A **340**, 339 (1991).

[Kra96] E. Krausmann, W. Balogh, H. Oberhummer, T. Rauscher, K.-L. Kratz, and W. Ziegert, Phys. Rev. C **53**, 469 (1996).

[Kun] P. D. Kunz, computer codes DWUCK4 and DWUCK5, unpublished.

[Loh74] J. M. Lohr and W. Haeberli, Nucl. Phys. A **232**, 381 (1974).

[May48] M. G. Mayer, Phys. Rev. **74**, 235 (1948).

[May49] M. G. Mayer, Phys. Rev. **75**, 1969 (1949).

[Mic05] http://www.micronsemiconductor.co.uk

[Möl95] P. Möller, J. .R. Nix, W. D. Myers, and W. J. Swiatecki, At. Data Nucl. Data Tables **59**, 185 (1995).

[Mon78] L. A. Montestruque, M. C. Cobian-Rozak, G. Szaloky, J. D. Zumbro, and S. E. Darden, Nucl. Phys. **A305**, 29 (1978).

[Mue05] P. E. Mueller, private communication.

[Muk01] A. M. Mukhamedzhanov, C. A. Gagliardi, and R. E. Tribble, Phys. Rev. C **63**, 024612 (2001).

[Muk05] A. M. Mukhamedzhanov, private communication.

[Omt91] J. P. Omtvedt, B. Fogelberg, and P. Hoff, Z. Phys. A **339**, 349 (1991).

[Ots01] T. Otsuka, R. Fujimoto, Y. Utsuno, B. A. Brown, M. Honma, and T. Mizusaki, Phys. Rev. Lett. **87**, 082502 (2001).

[Pad05] E. Padilla-Rodal1, A. Galindo-Uribarri, C. Baktash, J. C. Batchelder, J. R. Beene, R. Bijker, B. A. Brown, O. Castaños, B. Fuentes, J. Gomez del Campo, P. A. Hausladen, Y. Larochelle, A. F. Lisetskiy, P. E. Mueller, D. C. Radford, D. W. Stracener, J. P. Urrego, R. L. Varner, and C.-H. Yu, Phys. Rev. Lett. **94**, 122501 (2005).

[Pal75] V. Palladino and B. Sadoulet, Nucl. Instrum. Meth. **128**, 323 (1975).

[Per63] C. M. Perey and F. G. Perey, Phys. Rev. **132**, 755 (1963).

[Per76] C. M. Perey and F. G. Perey, At. Data Nucl. Data Tables **17**, 1 (1976).

[Per03] O. Perru, F. Ibrahim, O. Bajeat, C. Bourgeois, F. Clapier, E. Cottereau, C. Donzaud, M. Ducourtieux, S. Galès, D. Guillemaud-Mueller, C. Lau, H. Lefort, F. Le Blanc, A. C. Mueller, J. Obert, N. Pauwels, J. C. Potier, F. Pougheon, J. Proust, B. Roussière, J. Sauvage, O. Sorlin, and D. Verney, Phys. At. Nucl. **66**, 1421 (2003).

[Pre75] M. A. Preston, and R. K. Bhaduri, *Structure of the Nucleus* (Addison-Wesley, Massachusetts, 1975).

[Pri01] J. I. Prisciandaro, P. F. Mantica, B. A. Brown, D. W. Anthony, M. W. Cooper, A. Garcia, D. E. Groh, A. Komives, W. Kumarasiri, P. A. Lofy, A. M. Oros-Peusquens, S. L. Tabor, and M. Wiedeking, Phys. Lett. B **510**, 17 (2001).

[Qia03] Y.-Z. Qian, Prog. Part. Nucl. Phys. **50**, 153 (2003).

[Rap68] J. Rapaport and A. K. Kerman, Nucl. Phys. **A119**, 641 (1968).

[Rap72] J. Rapaport, A. Sperduto, and M. Salomaa, Nucl. Phys. **A197**, 337 (1972).

[Rat73] R. D. Rathmell, P. J. Bjorkholm, and W. Haeberli, Nucl. Phys. **A206**, 459 (1973).

[Rau97] T. Rauscher, F.-K. Thielemann, and K.-L. Kratz, Phys. Rev. C **56**, 1613 (1997).

[Rau98] T. Rauscher, R. Bieber, H. Oberhummer, K.-L. Kratz, J. Dobaczewski, P. Möller, and M. M. Sharma, Phys. Rev. C **57**, 2031 (1998).

[Reh98] K. E. Rehm, F. Borasi, C. L. Jiang, D. Ackermann, I. Ahmad, B. A. Brown, F. Brumwell, C. N. Davids, P. Decrock, S. M. Fischer, J. Görres, J. Greene, G. Hackmann, B. Harss, D. Henderson, W. Henning, R. V. F. Janssens, G. McMichael, V. Nanal, D. Nisius, J. Nolen, R. C. Pardo, M. Paul, P. Reiter, J. P. Schiffer, D. Seweryniak, R. E. Segel, M. Wiescher, and A. H. Wousmaa, Phys. Rev. Lett. **80**, 676 (1998).

[RIA05] http://www.orau.org/ria

[Rin80] P. Ring and P. Schuck, *The Nuclear Many-Body Problem* (Springer-Verlag, New York, 1980).

[Sak94] J. J. Sakurai, *Modern Quantum Mechanics* (Addison-Wesley, Reading, MA, 1994).

[Sam04] M. Samyn, S. Goriely, M. Bender, and J. M. Pearson, Phys. Rev. C **70**, 044309 (2004).

[Sas65] R. E. Sass, B. Rosner, and E. J. Schneid, Phys. Rev. **138**, 2B 399 (1965).

[Sat83] G. R. Satchler, *Direct Nuclear Reactions* (Oxford University Press, New York, 1983).

[Smi04] N. A. Smirnova, A. De Maesschalck, A. Van Dyck, and K. Heyde, Phys. Rev. C **69**, 044306 (2004).

[Str03] D. W. Stracener, Nucl. Instrum. Meth. **B204**, 42 (2003).

[Str04] D. W. Stracener, G. D. Alton, R. L. Auble, J. R. Beene, P. E. Mueller, and J. C. Bilheux, Nucl. Instrum. Meth. **A521**, 126 (2004).

[Str05] D. W. Stracener, private communication.

[Sur01] R. Surman and J. Engel, Phys. Rev. C **64**, 035801 (2001).

[Var91] R. L. Varner, W. J. Thompson, T. L. McAbee, E. J. Ludwig, and T. B. Clegg, Phys. Rep. **201**, 57 (1991).

[Win88] J. A. Winger, J. C. Hill, F. K. Wohn, R. L. Gill, X. Ji, and B. H. Wildenthal, Phys. Rev. C **38**, 285 (1988).

Vita

Jeffry S. Thomas

Education and Appointments

2000 B.S. in Physics, The College of New Jersey, Ewing, NJ

2000-01 Graduate Assistance in Areas of National Need Fellow,
Department of Education and Rutgers University

2001-05 Graduate Research Assistant,
Rutgers, The State University of New Jersey, New Brunswick, NJ

Publications - Journal Articles

2004 *"Is the Nuclear Spin-Orbit Interaction Changing with Neutron Excess?"*
J.P. Schiffer, S.J. Freeman, J.A. Caggiano, C. Deibel, A. Heinz, C.-L. Jiang, R. Lewis, A. Parikh, P.D. Parker, K.E. Rehm, S. Sinha, J.S. Thomas
Phys. Rev. Lett. **92**, 162501 (2004)

2004 *"Study of the* ^{124}Sn*(d,p) reaction in inverse kinematics close to the Coulomb barrier"*
K.L. Jones, R.L. Kozub, C. Baktash, D.W. Bardayan, J.C. Blackmon, W.C. Catford, J.A. Cizewski, R.P. Fitzgerald, M.S. Johnson, K.L. Jones, R.J. Livesay, Z. Ma, C.D. Nesaraja, D. Shapira, M.S. Smith, J.S. Thomas, D.W. Visser
Phys. Rev. C **70**, 067602 (2004)

2005 *"First Study of the Level Structure of the r-Process Nucleus* ^{83}Ge*"*
J.S. Thomas, D.W. Bardayan, J.C. Blackmon, J.A. Cizewski, U. Greife, C.J. Gross, M.S. Johnson, K.L. Jones, R.L. Kozub, J.F. Liang, R.J. Livesay, Z. Ma, B.H. Moazen, C.D. Nesaraja, D. Shapira, M.S. Smith
Phys. Rev. C **71**, 021302(R) (2005)

2005 *"Population of superdeformed excitations in* ^{198}Po*"*
M.S. Johnson, J.A. Cizewski, M.B. Smith, J.S. Thomas, J.A. Becker, L.A. Bernstein, A. Schiller, D.P. McNabb, P. Fallon, A.O. Macchiavelli
Phys. Rev. C **71**, 024317 (2005)

2005 *"New constraints on the* ^{18}F*(p,α)*^{15}O *rate in novae from the (d,p) reaction"*
R.L. Kozub, D.W. Bardayan, J.C. Batchelder, J.C. Blackmon, C.R. Brune, A.E. Champagne, J.A. Cizewski, T. Davinson, U. Greife, C.J. Gross, C.C. Jewett, R.J. Livesay, Z. Ma, B.H. Moazen, C.D. Nesaraja, L. Sahin, J.P. Scott, D. Shapira, M.S. Smith, J.S. Thomas, P.J. Woods
Phys. Rev. C **71**, 032801(R) (2005)

2005 *Quasicontinuous Decay and Properties of Superdeformed Excitations in* ^{195}Pb
M.S. Johnson, J.A. Cizewski, K.Y. Ding, N. Fotiades, M.B. Smith, J.S. Thomas, K. Hauschild, J.A. Becker, D.P. McNabb, L.A. Bernstein, R.M. Clark, M.A. Deleplanque, R.M. Diamond, P. Fallon, I.Y. Lee, A.O. Macchiavelli, F.S. Stephens
Phys. Rev. C **71**, 044310 (2005)

Publications - Conference Proceedings

2003 *"Single-particle structure of neutron-rich nuclei"*
J.A.Cizewski, K.L. Jones, J.S. Thomas, D.W. Bardayan, J.C. Blackmon, C.J. Gross, J.F. Liang, D. Shapira, M.S. Smith, D.W. Stracener, R.L. Kozub, C.D. Nesaraja, U. Greife, R.J. Livesay, Z. Ma
Proceedings of the Highly Specialized Seminar on Symmetries in Nuclear Structure, edited by A. Vitturi and R.F. Casten (World Scientific, New Jersey, 2003)

2004 *"Studies of the neutron single-particle structure of exotic nuclei at the HRIBF"*
J.S. Thomas, D.W. Bardayan, J.C. Blackmon, J.A. Cizewski, U. Greife, C.J. Gross, M.S. Johnson, K.L. Jones, R.L. Kozub, J.F. Liang, R.J. Livesay, Z. Ma, B.H. Moazen, C.D. Nesaraja, D. Shapira, M.S. Smith
Proceedings of The Sixth International Conference on Radioactive Nuclear Beams, Nucl. Phys. A **746**, 178c (2004)

2004 *"The* ^{17}F*(p,γ)*^{18}Ne *direct capture cross section"*
J.C. Blackmon, D.W. Bardayan, C.R. Brune, F. Carstoiu, A.E. Champagne, R. Crespo, T. Davinson, J.C. Fernandes, C.A. Gagliardi, U. Greife, C.J. Gross, P.A. Hausladen, C. Iliadis, C.C. Jewett, R.L. Kozub, T.A. Lewis, F. Liang, B.H. Moazen, A.M. Mukhamedzhanov, C.D. Nesaraja, F.M. Nunes, P.D. Parker, D.C. Radford, L. Sahin, J.P. Scott, D. Shapira, M.S. Smith, J.S. Thomas, L. Trache, R.E. Tribble, P.J. Woods and C.-H. Yu
Proceedings of The Sixth International Conference on Radioactive Nuclear Beams, Nucl. Phys. A **746**, 365c (2004)

2005 *"Studies of (p,γ) reactions with the Daresbury Recoil Separator at ORNL'S HRIBF"*
R. Fitzgerald, E. Abbotoy, D.W. Bardayan, J.C. Blackmon, A.E. Champagne, A.A. Chen, U. Greife, D.W. Hill, A.N. James, R.L. Kozub, T.A. Lewis, R. Livesay, Z. Ma, S.L. Mahan, J.W. McConnell, W.T. Milner, B.H. Moazen, P.D. Parker, D.E. Pierce, M.E. Roettger, L.

Sahin, D. Shapira, M.S. Smith, F. Strieder, K.B. Swartz, J.S. Thomas, and D.W. Visser
Nucl. Phys. A **748**, 351 (2005)

2005 *"Single-neutron excitations in neutron-rich $N = 51$ nuclei"*
J.S. Thomas, D.W. Bardayan, J.C. Blackmon, J.A. Cizewski, R.P. Fitzgerald, U. Greife, C.J. Gross, M.S. Johnson, K.L. Jones, R.L. Kozub, J.F. Liang, R.J. Livesay, Z. Ma, B.H. Moazen, C.D. Nesaraja, D. Shapira, M.S. Smith, and D.W. Visser
Proceedings of The Fourth International Conference on Exotic Nuclei and Atomic Masses, submitted to Euro. Phys. J. Direct (2005)

2005 *"Developing techniques to study $A \sim 132$ nuclei with (d,p) reactions in inverse kinematics*
K.L. Jones, D.W. Bardayan, J.C. Blackmon, W.N. Catford, J.A. Cizewski, T. Davinson, U. Greife, M.S. Johnson, R.L. Kozub, J.F. Liang, R.J. Livesay, Z. Ma, C.D. Nesaraja, S. Pain, D. Shapira, M.S. Smith, J.S. Thomas, D. Visser, and P.J. Woods
Proceedings of The Fourth International Conference on Exotic Nuclei and Atomic Masses, submitted to Euro. Phys. J. Direct (2005)

2005 *"Neutron single-particle states in r-process nuclei near closed shells"*
J.S. Thomas, D.W. Bardayan, J.C. Blackmon, J.A. Cizewski, R.P. Fitzgerald, U. Greife, C.J. Gross, M.S. Johnson, K.L. Jones, R.L. Kozub, J.F. Liang, R.J. Livesay, Z. Ma, B.H. Moazen, C.D. Nesaraja, D. Shapira, M.S. Smith, and D.W. Visser
Proceedings of The Eighth International Symposium on Nuclei in the Cosmos, accepted Nucl. Phys. A (2005)